Electronic Thesis and Dissertation Repository

8-3-2023 10:45 AM

Wind Loading Analysis of Standing Seam Metal Roofs on Low-Rise Buildings

Ellen J. Marejka, *Western University*

Follow this and additional works at: https://ir.lib.uwo.ca/etd

Part of the Civil Engineering Commons

Abstract

Standing seam metal roofs (SSMR) are a roofing system made up of prefabricated panels secured to the underlying structural purlins using concealed clips. The present study sought to develop a simplified code-approach for evaluating SSMRs. A model of the wind field and wind loads was validated using wind tunnel data from Arif (2017), influence functions and clip layout from Xia (2022), and compared the results to ASCE 7-22. Worst case enveloped GCp were compared by area for three different models: (i) ASCE Method, which gives wind loads based on bare deck roof, (ii) Clip Tributary Area (CTA) Method, which assumed the SSMR configuration and the clip geometric tributary area to predict clip loads, and (iii) Influence Function (IF) Method, which assumed the SSMR configuration and influence functions to determine clip loads. A load adjustment factor was calculated to compare the pressure coefficients between the ASCE Method and IF Method, this quantified the difference between the code model and a model that considered load sharing. The ASCE Method produced results that followed normal building aerodynamics, showing as effective wind area size increases the peak pressure decreases. The CTA Method significantly overestimated the ridge clip and eave clip loads compared to the IF Method. Typically, a roof on a low-rise building experiences the highest suction at the corners and edges. These areas coincide with the clips that have the greatest load sharing, and thus, the peak suction was reduced in these regions. Predicted clip loads from the CTA Method and IF Method did not show correlation with area. The ASCE Method was compared to the IF Method and the proposed load adjustment factor was presented for each ASCE zone and for inner clips and ridge and eave clips separately. The load adjustment factor indicates the ASCE Method is generally 8–59% conservative in its predictions.

Keywords

i

Summary for Lay Audience

Standing seam metal roofs (SSMR) are a metal roofing system used on low-rise buildings in North America. They are prefabricated, manufactured systems that haven proven to be water-tight and unaffected by extreme temperatures. The SSMR panels are secured to the roof structure using fasteners called clips. Generic prescribed building codes, such as ASCE 7, do not consider the details of load sharing among the panels, clips, and roof structure in these manufactured SSMR systems. However, it is worthwhile to study the load sharing in order to optimize the design. This idea forms the basis of the current research.

In this thesis, an analysis of wind tunnel data was used to predict wind loads on a building with standing seam metal roof. The wind loads of three prediction models were compared. The first model used the simple, standardized approach found in the ASCE building code. The second model used a hybrid of the building code and a verified analytical model. The third model, thought to be most realistic, used just the verified analytical model. A comparison of the three models showed that while the building code is a good estimator of wind loads, it is very conservative and overestimated the loads when compared to the analytical model. Some recommendations to improve the building code were presented.

Acknowledgements

Table of Contents

List of Figures

List of Tables

List of Nomenclature and Abbreviations

Acronyms and Abbreviations

2L: Open country terrain with 0.38 m (15 in) barrier

2S: Open country terrain, no barrier

FIU: Florida International University

ABL: Atmospheric Boundary Layer

ASCE: American Society of Civil Engineers

ASTM: American Society for Testing and Materials

B1 – B4: Denotes the four different building plan configurations

B: Smaller length of the building plan dimension

BLWT: The Boundary Layer Wind Tunnel II

C&C: Components and Cladding

CTA Method: Clip Tributary Area Method

DAD: Database-Assisted Design

ESDU: Engineering Sciences Data Unit

FEM: Finite Element Modelling/Model

H1:   Height of the shorter models (0.078 m)

H2:   Height of the taller models (0.234 m)

IF Method: Influence Function Method

IRLBH: Insurance Research Lab for Better Homes

L: Greater length of the building plan dimension

Lieblein BLUE: Best Linear Unbiased Estimator (Lieblein, 1974)

LRC   Load-Response Correlation

MSU: Mississippi State University

MWFRS: Main Wind-Force Resisting System (ASCE, 2010)

NBCC: National Building Code of Canada

NIST: National Institute of Standards and Technology

PLA: Pressure Loading Actuator

PLA: Pressure Loading Actuator

RHVR: Roof Height Velocity Ratio

SSMR: Standing Seam Metal Roof

USD: United States Dollars

UWO: University of Western Ontario

WERFL: Wind Engineering Research Field Laboratory

Notation and Symbols

α_T Scale parameter of Gumbel distribution for time period T

α_t Scale parameter of Gumbel distribution for time period t

$\bar{C}p_{AA}$ Mean area-averaged pressure coefficient

$\bar{P}$ Mean pressure at roof height

$\bar{q}_H$ Mean dynamic pressure at roof height

$\bar{U}$ Mean wind speed

$\check{C}p_{AA}$ Peak pressure coefficient

$\chi^2(f)$ Aerodynamic admittance function

μ_T Location parameter of Gumbel distribution for time period T

μ_t Location parameter of Gumbel distribution for time period t

ρ Air density, $1.225\ kg/m^3$

σ_{U_H} Standard deviation of wind speed

τ Time lag

A_e Effective area (the area where $I(x,y) \neq 0$)

A_g Geometric tributary area

A_{IF} Influence surface associated with the influence function

A_i Area of pressure tap i that falls within tributary area, A

A_{total} Total area considered in area-average

C Conversion factor

Cp Pressure coefficient

$Cp_{AA}(t)$ Area-averaged pressure coefficient at time, t

$Cp_i(t)$ Pressure coefficient for tap i at time, t

Cp_{ref} Pressure coefficient referenced to the reference height, *i.e.*, pitot tube height

F_U Uplift force on a component

g Peak factor

GCp Equivalent peak pressure coefficient as in ASCE 7

H Roof height of the model

I Importance factor

i Pressure tap indicator

$I(x,y)$ Influence function

I_U Turbulence intensity

K_d Directionality factor

K_h Exposure factor

K_{zt} Topography factor

L_u Integral length scale

m Number of samples

P Probability of non-exceedance

$P(x, y, t)$ Pressure at *(x,y)* at time, *t*

P_ASCE Pressure as defined in ASCE 7

$R(\tau)$ Auto-correlation function

$RHVR$ Roof height velocity ratio

$S_\mathrm{P}(f)$ Power spectral density function of fluctuating pressure

$S_\mathrm{U}(f)$ Power spectral density function of fluctuating velocity

T Extrapolated time period, full-scale

t Time period, full-scale

T_u Integral time scale

$U'(t)$ Fluctuating wind speed component at time *t*

$U_\mathrm{10m,\,open,\,3s}$ 3 second wind speed at 10 m above ground in open country terrain

U_H Wind speed at roof height

U_ref Wind speed at reference height

1 Introduction

There is a growing need to improve and strengthen infrastructure in the current world. This need stems from the strain that has been put on natural resources, whether it be demand for renewable resources like solar energy, or the need for more resilient structures in the event of natural disasters. The current research focuses on the latter with respect to severe wind storms like tornadoes, hurricanes, and typhoons, and their effects on low-rise buildings. Some of their impacts can be seen in Figure 1. Severe storms are a significant source of economic loss in the global economy resulting in roughly $32 billion USD in damage every year since 1990 (Xia, 2022). In fact, about 70% of insured losses can be attributed to wind storms (Holmes, 2015). The damage is due to both direct destruction from high winds, and indirect destruction such as accompanying flying debris and water damage.

Figure 1: Photograph of compromised houses from damage survey from the Barrie Tornado in 1985.

1.1 Wind Loading on Low-Rise Buildings

Low-rise structures account for the majority of buildings in North America, with a range of construction techniques including steel-framed (*e.g.*, warehouses, hangars), wood-framed

(*e.g.*, houses), concrete, or a combination thereof. The durability of these structures is of the utmost importance to social and economic welfare.

During periods of high winds, the air flows over and around a building creating high suction forces on the exterior and large positive pressures internally, resulting in high net pressures (Crandell et al., 1993). The roof is particularly vulnerable to these high net pressures because it experiences extreme fluctuating wind loads from flow separation and the formation of conical vortices (Holmes, 2015). A building's structural system, or Main Wind-Force Resisting System (MWFRS), endures the pressure acting on larger areas while higher net pressures act on the smaller areas associated with components and cladding (ASCE, 2010).

Components and cladding (C&C) are parts of the building envelope that are not considered to be in the MWFRS. Components receive wind loads either directly or from cladding. From there, the load is transferred to the MWFRS (ASCE, 2016). Examples of components include fasteners and purlins. Cladding receives wind pressures directly. Examples of cladding include curtain walls, roof decking, and sheathing. Due to the nature of building aerodynamics, the roof C&C experience much greater wind pressures than the MWFRS. Therefore, if there are damages to be incurred during a wind storm, it is most likely that they are incurred by the roof C&C as they are highly susceptible to damage. An example of this is shown in Figure 2, where the houses have intact structural systems, but the shingles, siding, and fenestration have been damaged.

(a)	**(b)**

Figure 2: Photographs (a) and (b) showing cladding failures with intact structural systems (Joplin, Mo., 2011, courtesy of Dr. David Prevatt).

1.2 Standing Seam Metal Roof Systems

Metal roofing systems have been used for decades because of their weatherproofing ability, ease of construction, and low economic cost. Metal roofing originated with through-fastened roof design in which sheet metal panelling would be secured to the structural members (*e.g.*, purlins) by screws that penetrated through the panel (Baskaran and Dutt, 1997). Inevitably, this design was susceptible to water ingress around the screw head. Furthermore, these single-ply roof systems were unable to handle the effects of flutter and fatigue caused by high winds. Metal roofing construction has since become more resilient; Standing Seam Metal Roofs (SSMR) are no exception. SSMRs are a modern type of roofing system made up of an array of prefabricated metal panels that span from the roof ridge to the eave edge. Figure 3 displays the various applications of SSMRs for agricultural, residential, and industrial land uses.

<center>(a)</center>   <center>(b)</center>

<center>(c)</center>

Figure 3: Examples of common standing seam metal roof systems (a) barn, (b) house, and (c) warehouse.

The panels of an SSMR system are secured to the structural members of the roof using clips, as seen in Figure 4. The clips are concealed in the seam itself. A diagram of SSMR construction is shown in Figure 5. A panel has two distinct parts: a horizontal section and two standing seams, one at each end along the shorter length. The repetition of panels and seams on the roof surface creates a ribbing pattern perpendicular to the roof ridge (Dixon et al., 2011). It is typical for SSMRs to be constructed of steel or corrosion-resistant aluminum panels, ranging from 0.3 mm and 0.7 mm in thickness. They are between 0.30 m (12 in) and 0.76 m (30 in) in width (Prevatt et al., 1995; Song et al., 2017). The length of the panel varies greatly being as short as 1.2 m (4ft) and up to 13.7 m (45 ft) and is customized to the roof size.
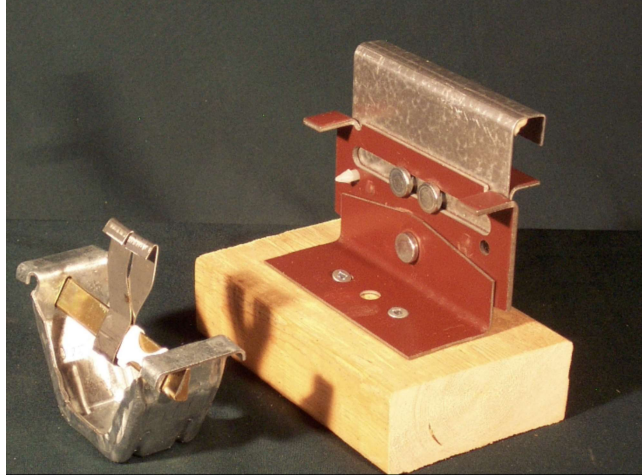
Figure 4: Photograph of a clip used in SSMR systems (Prevatt et al., 1995).

The standing seams commonly take on a vertical-leg or trapezoidal profile, as can be seen in Figure 6. The seams provide support to the structural system and allow for closed connection between adjacent panels. Compared to a conventional shingled structure, the SSMR has no need for roof sheathing or shingles since a panel can be fastened directly to the purlins through the clips hidden within the folded seam. There are a variety of clips available for use in these systems, including fixed clips without stand-off, fixed clips with stand-off, and floating clips, to name a few. Although it is not required, roof sheathing can still be used with this system. The seams are above the waterline of the roof (Prevatt et al., 1995). The ribbing of the seams direct any flowing water away from the seams. This feature provides a valuable design that does not allow for water ingress like a through-fastened roof.
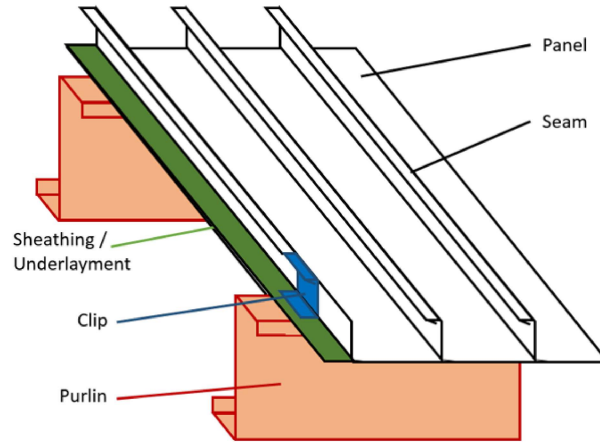
Figure 5: Diagram of a standing seam metal roof.

In addition to being water-tight, the metal panels and clips are capable of withstanding extreme temperature fluctuations. To account for the thermal properties of the metal, a panel is able to shift relative to the clip and a panel is able to act as a diaphragm to the structural frame (Dixon et al., 2011). Furthermore, panels are produced and assembled in manufacturing facilities. This prefabrication reduces the likelihood of processing and installation errors (Song et al., 2017). SSMR design has proven to be valuable through its ability to supply a water-tight, corrosion and thermal resistant environment. However, there are well-studied shortfalls of the system from a wind engineering perspective, in terms of design, installation, and testing.
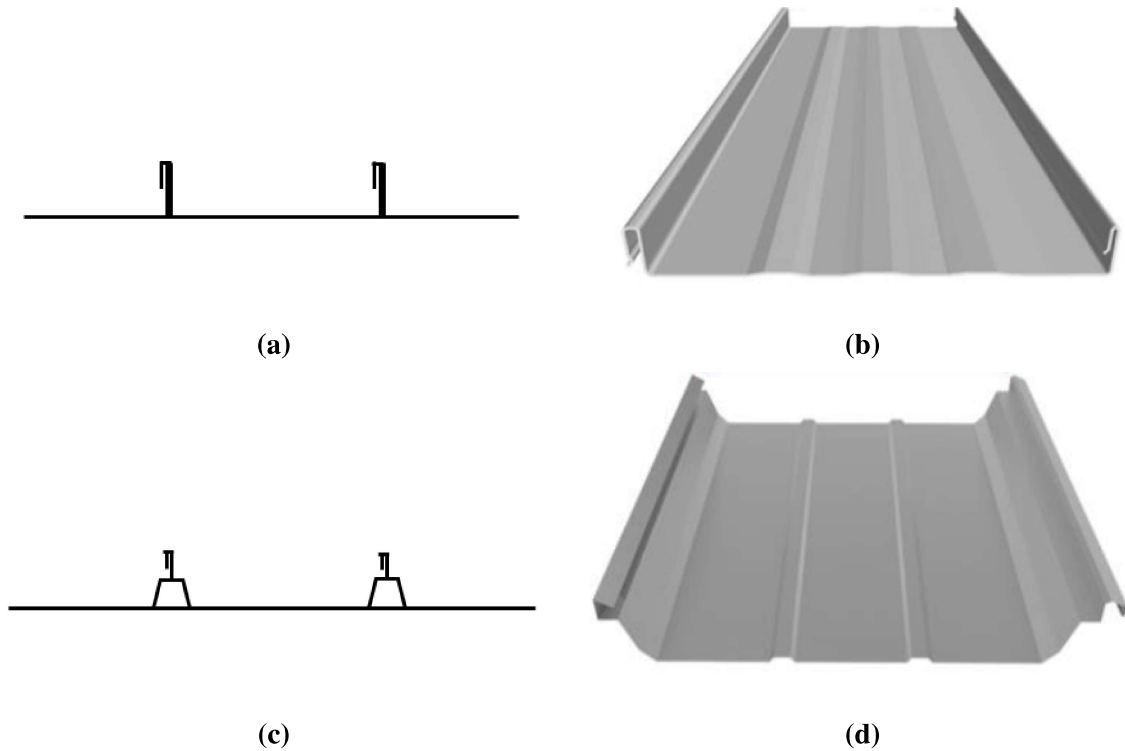
Figure 6: Diagram of standing seam with (a), (b) vertical-leg seam and (c), (d) trapezoidal seam (Habte, 2015).

The metal panels used in standing seam roofs are light-weight and, depending on their thickness, can be flexible. Typically, these panels range from 0.3 mm and 0.7 mm in thickness. A flexible panel can provide some structural stability since it will constantly adjust to the building frame, allowing panels to deflect between structural supports. However, the flexible panel will also experience deflection and distortion (Dixon et al., 2011; Prevatt et al., 1995). When under pressure, these panels can deform enough to change their properties and performance, potentially leading to premature, catastrophic failure. The deformation of panels can occur under positive pressure (*i.e.*, download, gravity) or negative pressure (*i.e.*, uplift, suction). This effect is shown in Figures 7 and 8. The extent of deformation is a function of the panel width, panel thickness, and properties of the panel material (Schroter, 1985). In efforts to prevent premature failure, there have been studies on the load path between roof components and structural members.
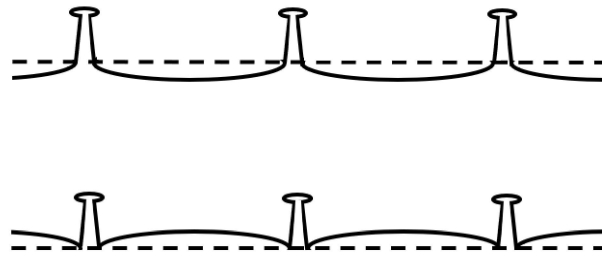
(b)

Figure 7: Panel deformation under (a) positive pressure and (b) negative pressure.

(a)   **(b)**

Figure 8: Section testing on a standing seam metal roof in a laboratory (a) before uniform pressure was applied and (b) after loading (Prevatt and Schiff, 1996).

SSMRs experience failure when there is such excessive and irreversible distortion to the panel resulting in a clip failure at the seam joint (Sinno, 2008). Clip failure is difficult to evaluate in these systems because no single component controls the failure of the seam joints, but it is rather a combination of several mechanisms. The failure modes of these roofing systems are quite different than the failures observed in the through fastened roofs discussed in Baskaran et al. (1997). The most common failure modes of SSMRs subjected to standardized testing are seam opening and horizontal movement of the seam, as shown in Figure 9. Seam opening occurs when the uplift force on the panel is great enough to

8

cause the clip to become dislodged from the panel. Horizontal movement of the seam is similar, however the clip is bent and shifted horizontally, causing the panel to become disconnected from the clip. In either case, once the clip is separated from the seam and no longer connected to the panel, the panel can freely peel back or fly off the building and the roof is breached.
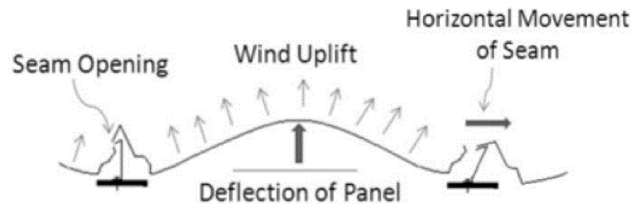
Figure 9: Profile of failure modes on SSMR system Dixon et al., 2011.

Another failure mode observed in Habte et al. (2015) is the clip rupture or breakage. This failure occurred under dynamic testing conditions where the vibration of the non-uniform wind loading caused fatigue failure of the clip. This is shown in Figure 26 of Chapter 2.

1.3 Current Approach to Determine Design Loads on Components and Cladding

The natural movement of the air within the atmospheric boundary layer (ABL) is unsteady in time and non-uniform in space. Studying these wind effects on structures, thus, becomes a challenging task. There are several analysis methods, including full-scale tests, model-scale wind tunnel simulations, structural analysis software (*e.g.*, finite element modelling), and application of forces via point loads or through pressure loading actuators systems (PLA). These methods have created a network of information that fostered the development of building codes and construction practices.

1.3.1 Experimental Test Methods

When wind acts on a low-rise building it creates a distribution of pressure on the surfaces, affecting the superficial elements known as components and cladding. As previously

mentioned, the components and cladding of the roof will experience much greater wind pressures than the MWFRS (Holmes, 2015). To prevent premature failure, it is important that wind pressure incurred by C&C can be accurately modelled and studied. The wind field acting on the C&C are related through building aerodynamics. The relationship between aerodynamics and structural response forms the foundation of wind engineering and building codes. The most common approaches to determine wind loads include full-scale testing and wind tunnel testing.

Full-scale testing facilities, like the 12-fan Wall of Wind (WOW) open jet facility at Florida International University (FIU), are novel systems used to determine wind loading and responses of structures. Engineered buildings (*e.g.*, made of steel or concrete) tend to have less variability than non-engineered structures (*e.g.*, wood-framed construction). This variability of materials and connections leads to systems that have unknown load paths (Kopp et al., 2012). Although full-scale experiments cannot predict these load paths like computer modelling, they are able to simulate the severe winds experienced in a storm in ways that wind tunnel tests cannot. After completion of the experiment, exhaustive damage surveys can help determine the failure mechanisms of the building and materials. This insight can help identify the deficiencies in building codes, such as toe-nailed roof-to-wall connections (Kopp et al., 2012). In place of massive fan arrays, PLAs can be installed on full-scale models such as the Three Little Pigs house in Kopp et al. (2010), or on cladding such as in Henderson and Ginger (2011). In full-scale PLA testing, the test specimen is subjected to simulated cyclonic wind loads by the PLA with an air bag system. The test results can be integrated with computational models to enhance building codes (Kopp et al., 2010; Henderson and Ginger, 2011).

The current approach of modelling wind loads requires generating pressure distributions using wind tunnel test data. Wind tunnel testing in a boundary layer wind tunnel is a widely-used and accepted instrument for assessing wind loads. It is also more cost-effective and requires fewer skilled technicians than full-scale testing. The test section of the Boundary Layer Wind Tunnel (BLWT) at University of Western Ontario (UWO) is shown in Fig-

ure 10. It is used to simulate realistic flows within the ABL by setting the parameters of the test (*e.g.*, wind speed, turbulence characteristics, building model size and shape) to the equivalent values observed in ABL. Wind tunnels may introduce uncertainties due to blockage ratios or scaling from mismatching Reynolds numbers (Azzi et al., 2020). The wind tunnel tests used in the current research are described in Chapter 3. There are other techniques used to quantify wind loads, including component capacity and failure testing. These standardized test methods are discussed in the following section.

BLWT II	Length (m.)	Width (m.)	Height (m.)	Max.Speed (km/hr.)
Overall Size	64	15	6	-
High Speed Test Section	39	3.4	2.5	100
Low Speed Test Section	52	5	4	36
Water Channel	52	5	2	-

Drive: 215kw: Variable Speed D.C.
Fan: 2.5m Diameter
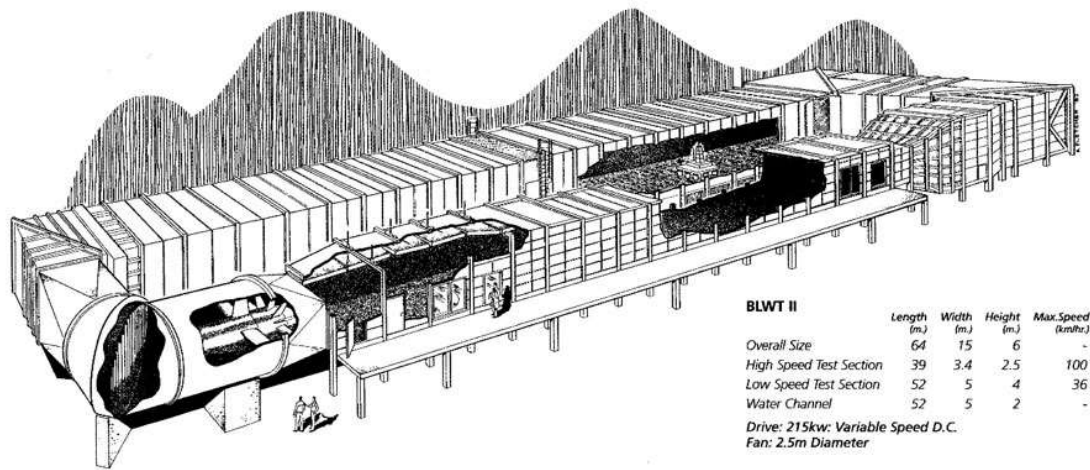
Figure 10: Sketch of the Boundary Layer Wind Tunnel test section as it was set up at Western University circa 1980 (Western University, 1980).

1.3.2   Standardized Test Procedures

A standardized test is used to determine the structural capacity of a product. The test can solely determine the capacity of that specific product and then express if a product meets or exceeds a particular design specification. For metal roofing systems there are several capacity tests including, but not limited to: ASTM E1592, UL 580 (2006), UL 1897 (2015), FM 4474, and CSA A123.21 (2014). All tests are similar in that they only consider a sample size of a full-scale roof. This roof sample is replicated in a laboratory to the size listed in the test standard. It then encounters a load exerted by a pressure chamber. The load is commonly a static uniform pressure applied as either a step-and-hold load or as a ramp load. The actual magnitude of the load is set forth in the specified test standard. The

majority of these tests are failure-driven and can provide an ultimate capacity of product (Prevatt et al., 1995).

For instance, the American Society for Testing and Materials (ASTM) outlines a procedure known as ASTM E1592 for the testing of sheet metal roof systems. This test, *Standard Test Method for Structural Performance of Sheet Metal Roof and Siding Systems by Uniform Static Air Pressure Difference*, only considers a segment of a roof system of approximately 3 m by 7 m. A pressure chamber is installed on the roof section and a reference pressure is applied for one minute. The reference pressure is at least four times, but not more than ten times the dead weight of the roof section. This is followed by one minute of an applied load of one third of the anticipated failure pressure, and then the pressure is returned to the reference value. This process continues in more detail until the roof fails, which is discerned by seams opening or clip-seam or purlin-clip rupture (ASTM International, 2001). This can be seen in Figure 11. The displacement of the panel is recorded throughout and a load-displacement curve can be plotted to find the uplift capacity. However, because this test only assesses a portion of the roof, the displacement is only measured in the vertical direction and will not account for lateral shifts that could be observed in wind tunnel testing. This leads to results that are approximately 50% to 80% conservative in the corner regions, depending on the roof system (Surry et al., 2007).
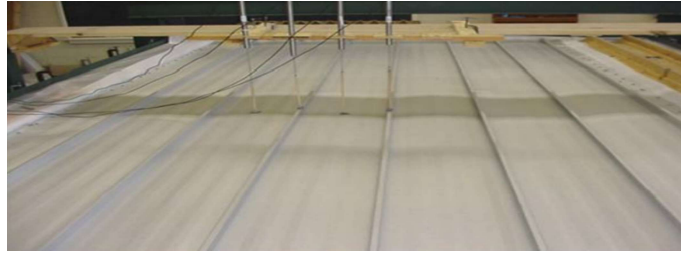
(a)

(b)

(c)

Figure 11: Standing seam roof built for uniform pressure testing (a) before loading, (b) during loading, and (c) after seam failure (Sinno, 2008).

There are minor distinctions between some of the standards. Underwriter Laboratories (UL) test procedure UL 580, *Safety Testing for Uplift Resistance of Roof Assemblies* examines the uplift resistance of a roof section and applies a rating to the roof. It can implement static and dynamic loads. Conversely, UL 1897 involves a similar apparatus, but it is a failure test similar to both ASTM E1952 and FM 4471. The test procedure described in CSA A123.21 strives to provide more reliable uplift capacities by using dynamic loading with vacuum chambers, however it still only considers a portion of the roof.

It is understood that standardized tests are limited by their loading techniques. The type of

load they apply, typically a uniform static pressure, is not illustrative of real wind loads that show extreme variation temporally and spatially. Moreover, standardized test methods are restricted by artificial boundary conditions. The small test section of roof cannot account for the dynamic-spatially varying properties of the wind-induced pressures and the resulting effects on the eave edge or roof ridge. The drawbacks are especially apparent in SSMR standardized testing experiments, which will be discussed in Chapter 2. In addition to full-scale experiments, wind tunnel simulations and standardized testing, there are also building codes which dictate results of such tests and whether or not they are within an acceptable risk level.

1.3.3   American Society of Civil Engineers (ASCE 7)

The pressure coefficients recorded during wind tunnel testing are simplified and compared to a design wind load. The design load may be expressed as a minimum value or a range of values, and is defined by the relevant building code for the geographical location of study. In the United States the provisions are largely based on the American Society of Civil Engineers (ASCE), Standard 7, *Minimum Design Loads and Associated Criteria for Buildings and Other Structures (ASCE 7)*. Chapter 30 of ASCE 7 describes wind loads specific to components and cladding. Note that the wind load provisions set forth in the National Building Code of Canada are largely based on the ASCE standards.

Buildings in the real world are constructed in many different ways and not all can undergo extensive wind tunnel testing. This creates the need to simplify wind loads in order to codify them. This codification can be observed in prescriptive building codes. For instance, in ASCE 7 the design load is a simple equivalent static load expressed as one value based on the zone in which the component falls (either interior, edge, or corner) and the effective wind area upon which the pressure acts. The loads are based on an agglomeration of studies completed on bare deck roofs and there are different values given for many different roof types (*e.g.*, gable, hip, saw-tooth etc.) and roof slopes (Habte et al., 2015). This is more clearly shown in Figures 12 and 13.
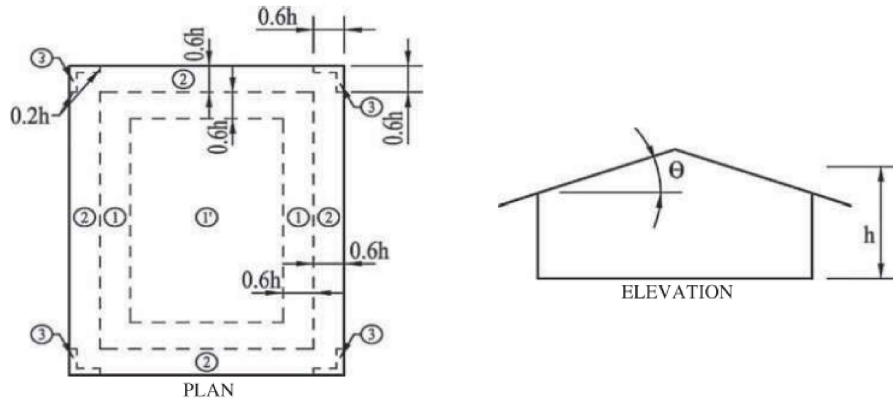
Figure 12: Diagram of roof zone designations and their respective locations for a gable roof low-rise building of particular slope (ASCE, 2022)
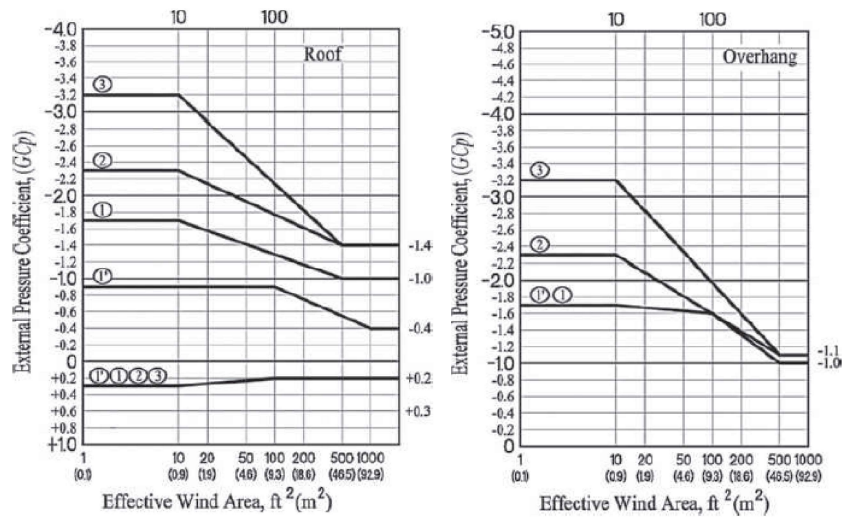
Figure 13: Corresponding peak equivalent pressure coefficients versus area for each zone (ASCE, 2022)

As can be seen in Figure 12, the size of the roof zones tend to depend on the mean roof height, h. This relationship was established in Kopp and Morrison (2018) which found that the cornering vortices tend to become proportionally larger as the building becomes taller (Kopp and Morrison, 2018). Furthermore, in Figure 13, it can be observed that as the effective wind area logarithmically increases the peak pressure decreases. Surry et al. (2007) demonstrated that increasing spatial-averaging area reduces the peak load over larger ar-

15

eas, which results in a trend of pressure decreases with area. This is typical aerodynamic behaviour for low-rise buildings.

The values in Figure 13 are calculated with Eq.(3), where GCp is the area-averaged peak pressure coefficient for the uplift force F_U, ρ is the air density, $U_{10m,\,open,\,3s}$ is the longitudinal 3 second gust speed measured in open terrain at 10 m above ground. There are four factors: K_{zt} which accounts for topography, K_d for wind directionality, K_h for velocity pressure exposure at the mean roof height, and I, the importance factor. The last term, A_e, is the effective tributary area of the component. This is written as,

$$F_U = P_{ASCE} A_e \qquad (1)$$

$$F_U = \frac{1}{2} \rho U^2_{10m,\,open,\,3s} GCp K_{zt} K_d K_h I A_e \qquad (2)$$

or

$$GCp = \frac{F_u}{\frac{1}{2}\rho U^2_{10m,\,open,\,3s} K_{zt} K_d K_h I A_e} \qquad (3)$$

In this research, the components under consideration are the clips which fasten the SSMR panels to the underlying structural purlin.

Although the ASCE approach is simple and straightforward, it may result in grossly conservative or unconservative design loads. This is because building codes are required to be applicable to a multitude of building types, and therefore cannot consider specific roof systems like SSMRs (Farquhar et al., 2005). This research assesses three approaches: ASCE Method, Clip Tributary Area Method, and an Influence Function Method. The comparison of these methods provides insight on improvements SSMR design standards.

1.3.4 Effective Tributary Area and Influence Functions

In general, the overall uplift, F_U, on a building component can be calculated using Eq.(5),

$$F_U = \int_A P(x, y, t) I(x, y) dA \qquad (4)$$

16

$$F_U = \frac{1}{2}\rho C \bar{U}_H{}^2 Cp \int_A I(x,y)dA \qquad (5)$$

where $P(x,y,t)$ is the pressure, C is a conversion factor to get the peak pressures at peak velocity, $\bar{U}_H$ is the mean hourly wind speed at roof height H, Cp is the pressure coefficient, and $I(x,y)$ is the influence function for a given component. The F_U can be converted to a GCp value by normalizing by the dynamic pressure. This is discussed thoroughly in Chapter 4. The GCp values from three different methods will be compared in the current study. The comparison will help in defining a load adjustment factor, F, which directly compares the ASCE Method and the Influence Function Method, clearly demonstrating the quantitative difference between the code approach and a model that considers realistic load transfer pathways.

In a low-rise building, there are multiple load paths and redundancies within these paths. This makes it difficult to ascertain which are the most critical (Xia, 2022). In layman's terms, an influence function is a tool that shows the effect of a force on a system and how that force is distributed. An influence function is a quantitative measurement of a reaction from an applied load. An influence function provides a direct connection between the load pattern and structural response, in this case allowing for more precise estimation of clip reactions. Influence functions result in a better understanding of spatial variation (Davenport, 1995). These functions can be thought of as a matrix of influence coefficients corresponding to spatial coordinates. These influence coefficients have a magnitude less than or equal to one.

The effective tributary area, A_e, is the integral of the influence function over the area, A, where $I(x,y) \neq 0$. This can be expressed as,

$$A_e = \int_A I(x,y)dA \qquad (6)$$

Thus, Eq.(5) can be simplified to

$$F_U = \frac{1}{2}\rho C \bar{U}_H{}^2 Cp A_e \qquad (7)$$

17

In this research there are two different approaches involving influence functions to obtain the effective tributary area: the Clip Tributary Area Method (CTA Method) and the Influence Function Method (IF Method). The first follows the ASCE provision of assigning tributary area to C&C, and the second is based on influence functions presented by Xia (2022).

The Clip Tributary Area Method is not actually prescribed in the code, but it the simplest approach taken by most designers (Morrison and Kopp, 2010). It assumes a unit influence function equal to one ($I(x,y) = 1$) in the geometric tributary area and zero ($I(x,y) = 0$) everywhere else. The geometric tributary area of a given clip is defined as half the distance to the adjacent clip.

A, is the area where $I(x,y) \neq 0$ for the given component, in this method the area would be equal to the component's geometric tributary area, A_{g}. Then Eq.(6) for a component becomes,

$$A_{\mathrm{e}} = \int_{A_{\mathrm{g}}} I(x,y)dA \qquad (8)$$

In this case, because it is a unit influence function, the effective tributary area is equal to the geometric tributary area. The Clip Tributary Area Method is the standard approach for both statically-determinate and statically-indeterminate systems. However, the assumption that the effective tributary area is equal to the geometric tributary area is not valid for statically-indeterminate systems, such as SSMRs.

Statically-indeterminate structures experience load paths that change with uplift force. These load paths are complex, redundant, and do not account for the load redistribution from deformed panels (Morrison and Reinhold, 2015). In the case of standing seam metal roofs, the panels are flexible and the deflection and deformation changes with uplift force.

An influence function for a statically indeterminate system can only be found through numerical modelling. The Influence Function Method can evaluate statically-indeterminate systems in a manner that is more representative of actual wind loading. The effective tributary area is found by integrating the influence function of a clip over the area where the

influence function is not equal to zero ($I(x,y) \neq 0$). In the current study, this area is the influence surface, A_{IF}. The influence surface is the length of the panel by the distance to the adjacent seams. This can be expressed mathematically as,

$$A_{\text{e}} = \int_{A_{\text{IF}}} I(x,y) dA \tag{9}$$

The geometric tributary area, A_{g}, of the Clip Tributary Area Method is not equal to the effective tributary area, A_{e}, for a statically-indeterminate system. This implies that the clip loads estimated with the Clip Tributary Area Method will be different than the clip loads estimated with the Influence Function Method. The Clip Tributary Area Method is easily applied in modelling, but it may not be as accurate as the Influence Function Method for SSMR systems because it ignores the actual load path, load sharing, and boundary conditions of the roof. For these reasons, SSMR systems should be evaluated and codified differently to bare deck roofs. A flowchart of the methodology is shown in Figure 14.
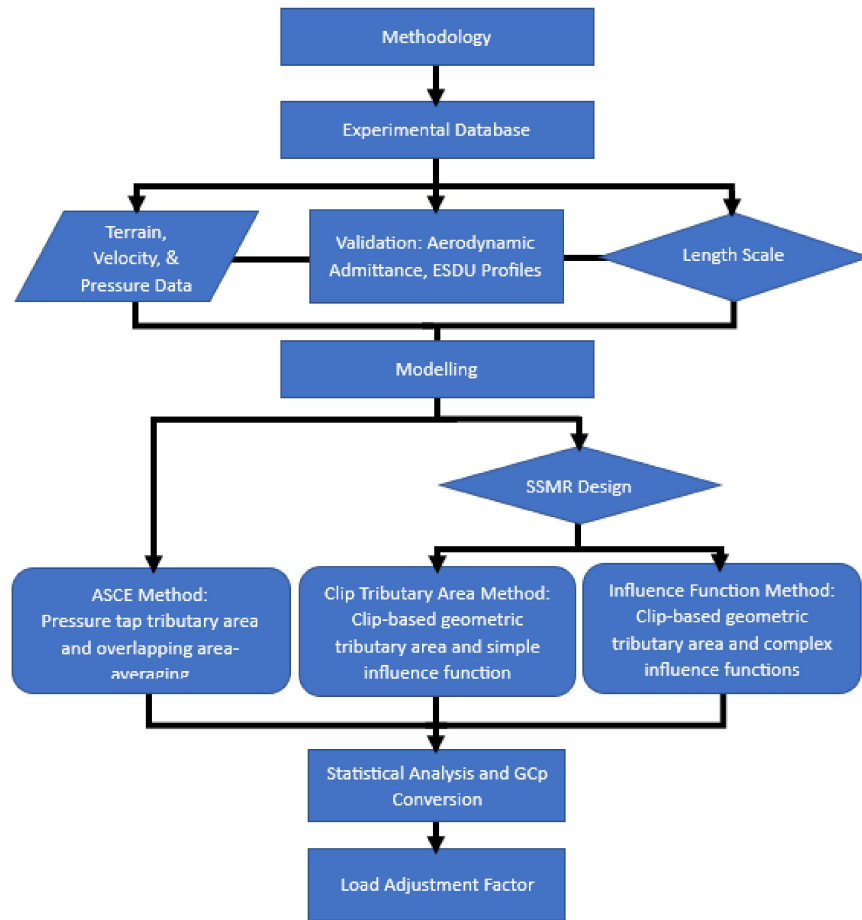
Figure 14: Flow chart of methodology, including experimental database and modelling approach

As discussed, both full-scale testing and wind tunnel experiments are ideal for basic shapes of building sizes, but are not practical for assessing all low-rise buildings outfitted with SSMRs. Standardized testing is best for C&C-specific inquiries, but has restrictions that make the data unreliable for a complete system. Furthermore, while the design load prescribed by ASCE is well-established and accepted for traditional roofing systems, it is not representative of the wind effects experienced by SSMR systems for several reasons. These SSMR roof systems are sensitive to wind loading. There is further work required to understand the uplift behaviour in order to accurately develop building codes. The need for more realistic design wind loads for metal roofing has formed the basis of the present study.

20

1.4 Objective of Thesis

The motivation for the present study is to develop an optimized code-approach for evaluating standing seam metal roof systems. The proposed approach will build upon previous works completed by Nasiri (2019) and Xia (2022). It will consist of three main parts:

- Determine wind loading on low-rise buildings using the general ASCE approach of area-averaging, referred to as the ASCE Method.

- Implement the Clip Tributary Area Method, which determines clip loads of several low-rise building configurations that have been outfitted with SSMRs by using a uniform influence function of one within the clip geometric tributary area.

- Implement the Influence Function Method, which determines the clip loads of several low-rise building configurations that have been outfitted with SSMRs by using influence functions and influence surfaces defined in Xia (2022).

The equivalent peak pressure coefficients from each of these methods will be compared and a load adjustment factor relevant to SSMRs will be calculated. Throughout the study, the models will be investigated and panel configurations will be assessed with respect to the building dimensions and aerodynamics.

1.5 Overview of Thesis

The thesis is described through the following sections:

- Chapter 1: A general introduction to the topic of research providing background on wind loading and the SSMR systems and the current approach for determining design wind loads for components and cladding.

- Chapter 2: A literature review elaborates the previous studies upon which the current research is founded. Discourses include notes on methods and results experimental or simulations completed for low-rise buildings. It discusses relevant wind tunnel

tests and finite element models from Xia (2022) necessary to complete the current study.

- Chapter 3: This section outlines the experimental setup and data processing from Arif (2017), which supplied the data used in the present research. It details the physical parameters for the wind tunnel tests, inclusive of the building models, terrain configurations, and sampling rates. It goes on to compare the testing conditions of Arif (2017) to Akon and Kopp (2016) in terms of velocity profile, spectra, and scale determination.

- Chapter 4: The modelling approach is described in Chapter 4. There is focus on the application of influence functions, effective tributary area, and layout of the roof panels. A comparison and validation to Kopp and Morrison (2018) is outlined in this section.

- Chapter 5: This chapter is dedicated to sharing results of the modelling and delves into a discussion on the layout of the roof panels. It debates the implementation of a load adjustment factor specific to SSMR panels for buildings of various plan dimensions.

- Chapter 6: Conclusions are presented for the current research, as well as the limitations of its application. Recommendations are provided for future work.

2 Literature Review

This chapter is a literature review that describes past research on low-rise buildings from a wind engineering perspective. It broadly examines early works on low-rise building and C&C test findings and their progression through time. It will elaborate on modelling SSMR systems and goes on to contemplate the design of these systems in regards to clips, seam construction, and panel deformation.

The MWFRS is defined by ASCE 7 as a collective of structural elements that provide stability and support to the building. Components and cladding, on the other hand, are an assemblage of elements within the building envelope that are not considered to be in the MWFRS. C&C provide limited structural support, but they are pertinent to the roof and wall coverings. C&C serve the functional purpose of protecting against natural elements like rain, snow, and wind. They are also recognized as aesthetically important architectural features of a building.

Investigating the wind effects on structures is an onerous process. There are several methods for studying wind loads on C&C which were mentioned in Chapter 1. They include full-scale testing (*e.g.*, Azzi et al., 2020), wind tunnel simulations (*e.g.*, Ho et al., 2005), component-specific testing (*e.g.*, Sinno, 2008), and computational models (*e.g.*, El Damatty et al., 2003). These various methods allowed for the experimentation and research that forms the basis of building provisions. Wind loads on SSMRs, however, are not well understood because of the complexity of the load paths.

2.1 Aerodynamic Studies on Low-Rise Buildings

There have been many works written on wind loading of low-rise buildings. Engineers and scientists alike have evaluated different experimental procedures and configurations in terms of predicting wind-loads. Some of these procedures were explored in Chapter 1, but here they will be discussed in greater depth with explanations of their contributions to wind

engineering as a whole.

2.1.1   Flow Separation, Turbulence, and Pressure Coefficients

Upstream flow conditions are essential to characterizing bluff body aerodynamics in different terrains. Studying the flow around these bluff bodies is also fundamental to understanding the loading and design of components and cladding. In this current research, flow separation, turbulence intensity, and peak pressures were used to validate wind tunnel data.

The upstream flow conditions create a wind field comprised of streamlines and boundary layers acting on a low-rise building. When these boundary layers meet the bluff edge of a low-rise building, they first separate at a location known as the separation point, shown in Figure 15. Then they curve towards the roof surface and reattach at a point known as the reattachment point. Upstream of the reattachment point, the flow is recirculating and creating a highly turbulent region known as the separation bubble (Akon, 2017). The size and shape of the separation bubble are affected by the building parameters as well as the turbulence intensity and the integral length scale (Akon and Kopp, 2016).
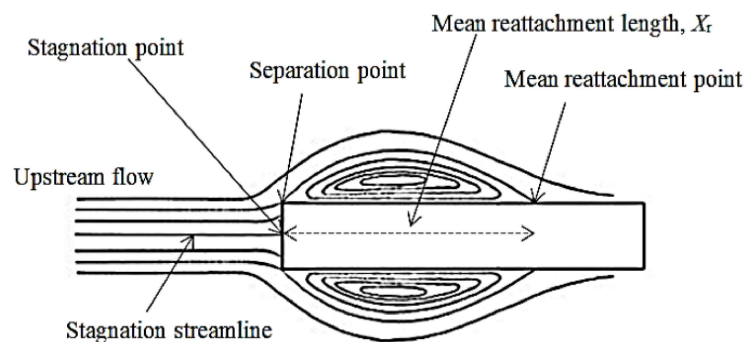
Figure 15: Diagram of separating and reattaching flow around the sharp edges of a 2D bluff body (Akon, 2017).

Flow separation and turbulence intensity is a topic that has attention of many, where studies tend to build on each other rather extensively. For instance, Wu et al. (2017) built on Akon and Kopp (2016) by improving the understanding of their physical observations with an

24

analytical model. It has been widely accepted that as turbulence intensity increases, the separation bubble shrinks and thus reattachment length become smaller. But, reattachment length is largely unaffected by the integral length scale (Akon and Kopp, 2016). Although high turbulence intensity causes faster reattachment, the pressure does not recover at the same rate. Wu et al. (2017) discovered that as upstream turbulence increases, the pressure actually recovers faster on the leeward side of the roof.

For the majority of low-rise building studied, there is considerable variation observed in the instantaneous pressure distributions of the peak loads, as shown through the peak and mean area-averaged pressures (Holmes, 1988; Surry et al., 2007). Arif (2017), Akon and Kopp (2016), and Wu et al. (2017) used the same models in their studies and established that the magnitude of the peak pressure coefficients are more dependent upon the integral length scale than on the turbulence intensity (Arif, 2017). The increasing magnitude of minimum mean pressure coefficients with turbulence intensity is ultimately related to the growing convection- and turbulence-pressure gradients (Wu et al., 2017).

2.1.2 NIST Aerodynamic Database and Related Studies

Perhaps the most comprehensive study of low-rise buildings is the National Institute of Standards and Technology (NIST) aerodynamic database. The NIST database is an archived collection of data sets that were contributed by the BLWT at University of Western Ontario (UWO). The data sets contain wind tunnel test parameters and results of low-rise, gabled-roof models of various dimensions, roof slopes, and scales. The data show trends consistent with typical aerodynamic behaviour (Ho et al., 2005). In the sister paper, St. Pierre et al. (2005) compared the structural responses to ASCE 7-02 wind load provisions for the United States (St.Pierre et al., 2005).

The NIST database provides aerodynamic information for database-assisted design for estimating structural reactions to spatially and temporally varying wind fields (Xia, 2022). The NIST data sets have since been used in several studies for wind loading on C&C and are still used today as a validation tool for new wind tunnel tests (Wang and Kopp, 2021b).

The current research also used comparable tests from the NIST database to verify findings and trends in the subject wind tunnel data, this is explored in Chapter 3. Another validation tool is the Levitan and Mehta (1992a) field measurements of real wind loads. This gave researchers comparative data for their own physical and analytical modelling.

Figure 16: Site of full-scale test building and surrounding terrain (Levitan and Mehta, 1992b).

The creation of the NIST aerodynamic database permitted the study by Kopp and Morrison (2018), which laid the foundation for the amended ASCE 7-10 provision, known as ASCE 7-16. ASCE 7-16 outlines design standards for roof C&C in greater detail than it's predecessor. The ASCE 7 provisions have the influence to create a more resilient built environment within North America. The authors identified the inconsistencies with the corner and edge zones through contour plots, seen in Figure 17. They redefined the zones using dimensions related to building height, as height was found to drive the spatial patterns of the area-averaged pressure coefficients. Much of the present thesis is based on methods employed in Kopp and Morrison (2018).
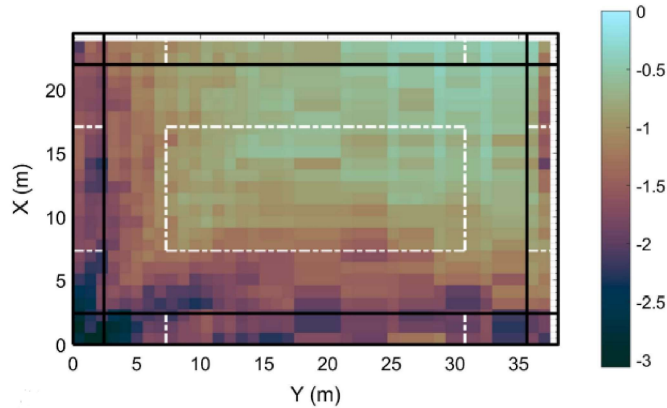
Figure 17: Example of worst-case pressure contour plot produced for the roof of a NIST building model with new proposed ASCE zones shown in dashed white line (Kopp and Morrison, 2018).

While only some were mentioned, there is no shortage of data on low-rise buildings from probabilistic, analytical, and experimental standpoints; However, there is relatively little research on low-rise buildings outfitted with SSMR systems. This review goes onto explain the valuable papers already published on metal roofing and SSMRs and their influence on how standing seam metal roofs are perceived.

2.2 Wind Studies on Metal Roofing Systems

Hurricane Andrew provided new opportunities to study wind loads on metal roofs. Smith (1995) found that theses roofs have potential to be excellent performers in storms, yet they are limited by the lack of design standards from manufacturing and installing perspectives (Smith, 1995). Standing seam metal roofs are remarkable roof systems, however, they are susceptible to uplift through the seam-clip connections. These connections are driven by interior clips that act as flexible supports for the roof and are even typically modelled as springs (*e.g.*, El Damatty et al., 2003; Nasiri, 2019). This should not discredit SSMRs as an effective and economically-viable roof system; instead a solution should be proposed to acknowledge them in regulation and reinforce them from a design perspective. This will be proposed in this research, taking the form of a load adjustment factor. Studies on

27

metal roofs and SSMRs are discussed and significant findings and solutions are listed in the following sections.

2.2.1 Finite Element Modelling and Numerical Simulations

Finite Element Modelling (FEM) is a numerical tool used to compute the response of structural or C&C systems to various loads. FEM is useful for SSMR systems as it allows the user to determine the influence functions of clips, and it can accurately model boundary conditions and elemental interactions. Ali and Senseny (2003) first considered the load-response of SSMR to create a risk model that estimates total losses from severe wind storms by looking at failure modes of components, fatigue demand, and repair schemes. They stated that a non-linear analysis is necessary to improve forecasts of panel deflection and seam deformation (Ali and Senseny, 2003). This was substantiated in El Damatty (2003) who incorporated the results of a full-scale SSMR test at Mississippi State University (MSU) and performed component testing to simulate the results with a three-dimensional FEM. An example of the model mesh and validation are shown in Figure 18. Conclusions were drawn including: (i) the clips take on approximately 69% of the total load applied to the roof, and (ii) the load at which a seam opens (and thus behaves in a non-linear fashion) is lower than the ultimate capacity of the clip, meaning that the seam opening will dictate the clip behaviour (El Damatty et al., 2003).
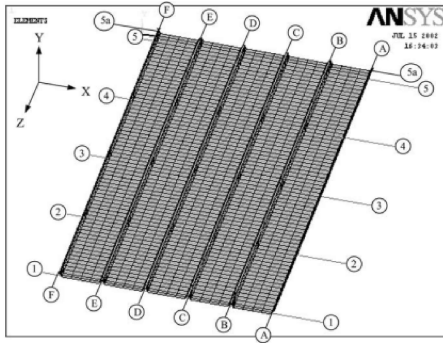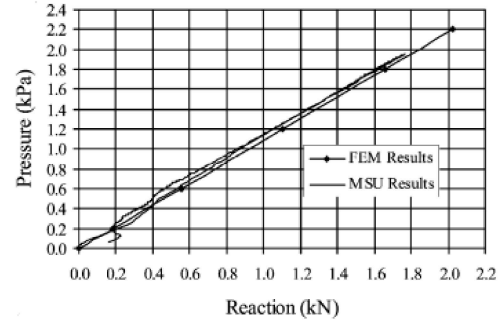
(a)   (b)

Figure 18: Modelling details including the (a) finite element mesh and (b) resulting validation between MSU experiment and FEM curve for clip C-2 (El Damatty et al., 2003).

To build on the previous two studies, Surry et al. (2007) compared the results of full-scale component test to model-scale wind tunnel tests on SSMR systems. Surry et al. (2007) illustrated the effect of spatial averaging, which is shown in Figure 19. They demonstrated that increasing spatial-averaging area reduces the peak load over larger areas. Therefore, designing an entire panel for the largest localized uplift on the panel is conservative so long as the panel is able to share the load.
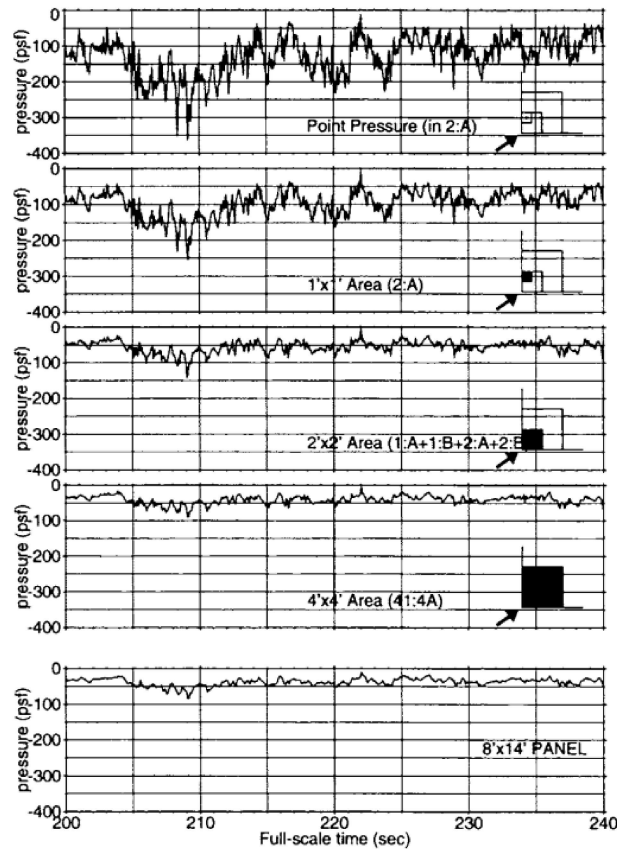
Figure 19: The pressure variation with time for different tributary areas near the corner of the roof (Surry et al., 2007).

The results showed significant consistency between the full-scale component test to the model-scale wind tunnel test, which overall suggested that for the windward corner, the ASTM E1592 test was about 50% conservative. Both experiments have limitations since neither can accurately capture the load response of the roof structure. It is hypothesized that full-scale experiments can provide calibration standard for FEM as done by El Damatty et al. (2003).

2.2.2 Development and Application of Influence Functions

Influence functions are well established tools, but are typically only used for specific practical applications. Engineers agree that influence functions are more widely applicable than they may seem, as they provide a direct connection of the load pattern to the response and

30

thus a better idea of spatial variation (Davenport, 1995; Prevatt et al., 1995; Surry et al., 2007).

In their research, Nasiri (2019) and Xia (2022) applied full-scale testing and finite element modelling to determine the influence functions and influence surfaces of all clips on a standing seam metal roof. This was done in efforts to better understand the load sharing and failure mechanisms of SSMR systems under realistic boundary conditions. Xia (2022) specifically upholded findings from Farquhar et al. (2005); both concluded that clip loads produced using effective tributary areas from influence surfaces are lower magnitude than the loads produced using the code-prescribed geometric tributary area.

The geometric tributary area method (referred to as Clip Tributary Area Method or CTA Method in this work) may produce unrepresentative clip reactions because it ignores boundary conditions. Influence functions have limitations though, since in a whole system, like a house, there are many nonstructural features that contribute to the strength of the building. They are also limited because the influence coefficient depends on the level of load being applied (Kopp et al., 2010).

Farquhar et al. (2005) applied uniform and wind tunnel pressures on a simple scaled SSMR model until failure. This was done in efforts to find a relationship between standardized testing and dynamic pressures of actual winds that cause failure. The pressure tap tributary area was assigned by equally dividing the area between the taps. An assumed influence function was used in the analysis of the clip reactions and peak pressure coefficients. This influence function is visually depicted in Figure 20.
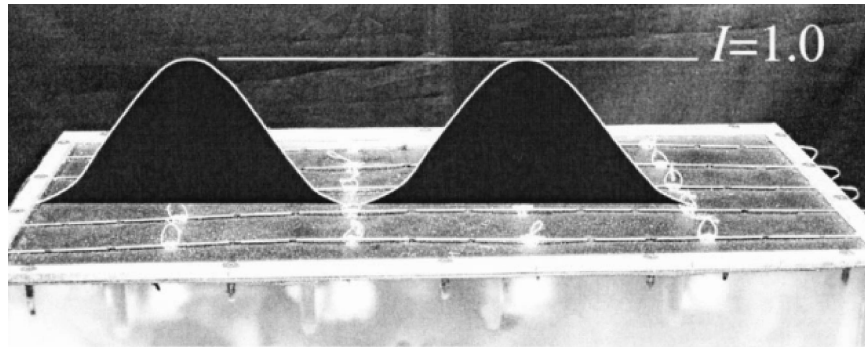
Figure 20: The along-seam influence function at two clip locations overlain on a photograph of the failure model (Farquhar et al., 2005; Morrison and Kopp, 2010).

The study found that none of the clips are significantly affected by the highly localized suctions that occur in the corner. The corner, which is typically the worst aerodynamic region, showed that the ASCE 7-02 design clip load overestimated the pressure by 30% compared to the actual peak clip load. This conservatism was attributed to the oversimplified design loads in ASCE 7-02, which are meant to be applicable to all buildings and roof systems and not one specific structure (Farquhar et al., 2005). In reality, the clip loads were governed by the smaller pressures found closest to the clips. This is a result of the larger effective areas from the influence function model. In addition to the design load discrepancies, the uniform static testing results were predicted with good accuracy by integrating the clip influence functions with the non-uniform pressures. It should be noted that testing on scaled SSMR models, like in Farquhar et al. (2005) may introduce scaling issues due to Reynolds number mismatch and not being able to capture the effects of the seam profile (Habte et al., 2015).

The continuation of Farquhar et al. (2005) used UWO's BLWT to test a high resolution panel fastened to a building model. Morrison and Kopp (2010) installed a panel containing over 700 pressure taps that was able to capture the effects of the cornering wind loads. The area-averaged pressure coefficients were calculated first using a uniform along-seam influence function of one in the clip geometric tributary area. Then it was calculated with an along-seam influence function defined in Farquhar et al. (2005) and an across-seam

32

influence function was defined as the decreasing linearly to 0 between adjacent seams. Results from Morrison and Kopp (2010) are consistent with Farquhar et al. (2005) and find ASCE 7-05 conservative in the corner with the exception that clips adjacent to the edge are not critical ones.

Nasiri (2019) employed load-response correlation (LRC) method to define the pressure distribution which causes the peak clip reaction. The LRC method was validated by full-scale testing, by applying a concentrated load at 576 different locations as 50 load cells measured the response at clip locations. A very simplified schematic of this is shown in Figure 21.
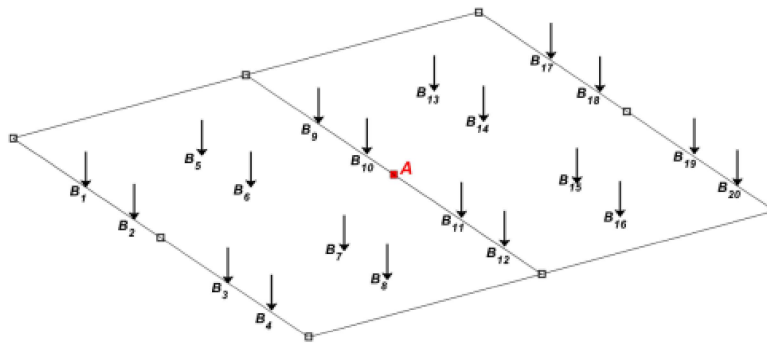
Figure 21: Schematic plot of clips (red square) and point load applications (black) (Nasiri, 2019).

Nasiri (2019) then went on to generalize the results for linear behaviour by using finite element analysis. The panel seam was modelled as a multi-span beam, which is by nature, is statically indeterminate. These multi-span beams consisted of simple supports at the eave and ridge with vertical spring supports internally. Their research found that using vertical springs provided a more realistic approximation than previous works (*e.g.*, Ho et al., 1995, El Damatty et al., 2003); however, modelling the eave and ridge clips as simple supports still showed oversimplification. This was determined by assessing the influence functions, which had a value of less than one at the clip locations, suggesting that considering clips as simple supports is not an accurate assumption (Nasiri, 2019).

Nasiri (2019) observed that the area of the adjacent panels along the seam, for the length of

the seam could be considered the influence surface, or effective tributary area. An example of the measured influence function from a clip is shown in Figure 22. The simplified approach taken by designers, however, assumes the effective tributary area is equal to the geometric tributary area. It also ignores the influence of boundary conditions and the roof profile on load sharing. The simplifications in the code lead to overestimated clip loads experienced by the boundary fastener. It was found that the load not transfer across the roof ridge (Nasiri, 2019).
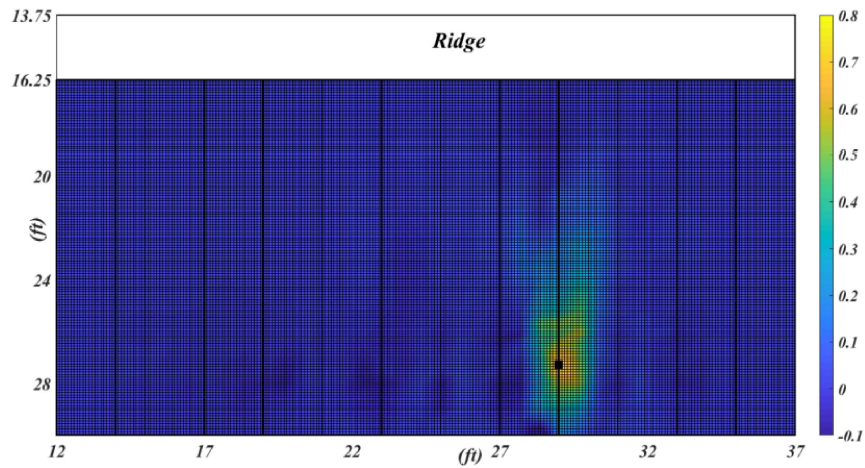
Figure 22: A clip (black square) and its influence function shown over the entire roof (Nasiri, 2019).

Nasiri (2019) found that clip loading remained linear between pressure distribution and structural response for low wind pressures of 0.5 kPa or less. When loading surpasses this pressure, the load distribution is no longer linear and panels deform more load transfers to the clips and fasteners at the roof edge. This was also confirmed by Sinno (2008) and Xia (2022).

Xia (2022) took the recommendations of Nasiri (2019) and created a FEM that modelled the panel seam as a beam with all clips as vertical springs. The FEM reproduced the failure modes observed in full-scale testing at Insurance Research Lab for Better Homes (IRLBH) completed by Xia (2022). The results show that boundary conditions have significant impact on the load distribution, and that ridge and eave constraints effect the load

34

redistribution the most (Xia, 2022). For the eave clip, the approximate maximum value of the influence function is 0.5, indicating that a sizeable portion of the load transfers to the fastener at the eave. For the ridge clip, there is a back-up plate at the ridge cap which supports the ridge fastener and restricts deflection.

Xia (2022) confirmed that of Nasiri (2019), stating that current standards do not consider boundary conditions, and consequentially they underestimate clip loads at the ridge and overestimate them everywhere else. Xia (2022) concluded that the ridge clip is more accurately modelled as a rigid support since it has the greatest stiffness (attributed to the back-up plate), but the same cannot be said for the fastener connection at the eave edge (Xia, 2022).

Furthermore, Xia (2022) found that the magnitude of the wind pressure has limited effect on the influence function along the seam. With this knowledge, a revised analytical model was presented using updated influence functions. The many versions of influence functions are shown in Figure 23 for a single clip type. There are 5 different clip types presented in this work which describes the clips location along the seam. The clips are physically identical and installed in the same manner on the roof. The updated analytical model presented by Xia (2022) is based on a load of 0 kPa.
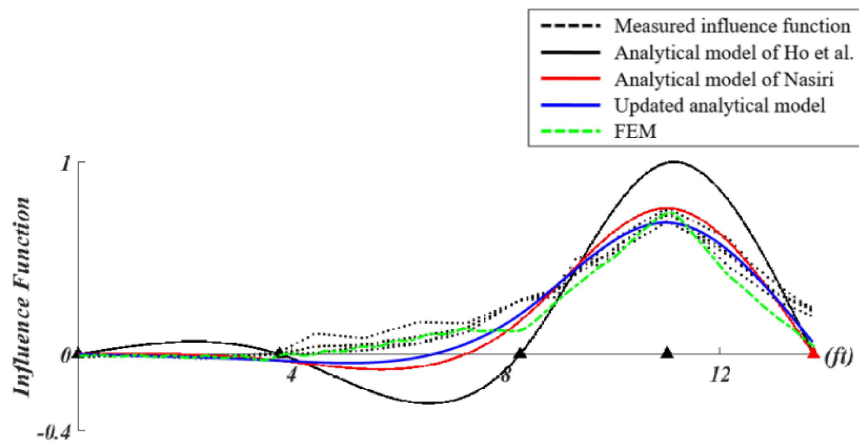
Figure 23: Comparison between influence functions of a clip at a specific location along the seam (Xia, 2022).

Xia (2022) then use database-assisted design (DAD) method and the updated analytical

model to better estimate the clip reactions of a roof system and compare the calculated values to those produced by ASCE 7-16. DAD method involves aerodynamic information, like that from wind tunnel testing, and structural information, like influence functions. ASCE 7-16 was found to give conservative estimations of clip reactions similar to Morrison and Kopp (2010) (Xia, 2022).

Influence functions allow for realistic understanding of load sharing of SSMRs. The influence functions and surfaces from Xia (2022) will be used in this current analysis in combination with wind tunnel data. In this study, the updated analytical model influence function was used for the along seam influence function. The across seam influence was equal to the calculated influence coefficient at the seam, and then decreases linearly to zero at the adjacent seam. This model is often used for roof panel analyses (*e.g.*, Ho et al., 1995, Farquhar et al., 2005, and Xia, 2022). These authors appreciated the importance of creating analytical models based on full-scale test results, and in many cases the most accurate studies are those that make use of experimental testing and validate them with computational models or vice versa.

2.2.3   Experimental Tests

The study of structural or component failure through experimental testing is done in efforts to improve designs and revise codes. For this reason, it is vital that wind loads incurred by these systems and elements be aerodynamically modelled in physical simulations. The most common approaches to modelling wind loads include full-scale testing (with or without PLAs) and wind tunnel testing. However, one of the first studies on metal roofing was an analysis of fastener pull-out loads on steel decks. It indicated that the fastener failure loads differ greatly under static and dynamic tests conditions, with resistance decreasing by 30-50% under the latter conditions. Thus, dynamic testing should be used to develop the allowable design load (Baskaran and Dutt, 1997). Habte et al. (2015) confirmed this as well. Schroter amended this and said that static air pressure tests are more reliable than mechanical pull-out tests (Schroter, 1985). Overall, this confirmed that mechanical pull-out

tests are less reliable than static pressure testing, but generally, dynamic testing provides the most realistic wind loading.

The deformation of a metal panel is a function of the panel width and thickness, material properties, and rib design; And the deformation is highly non-linear and shows that small pressures can lead to failure, in addition to geometric non-linearities altering the load transfer. In a study that utilized the BRERWULF (Building Research Establishment Real-Time Wind Uniform Load Follower) system developed by Cook et al. (1988), it was found that the end fastener of the SSMR can have remarkable effects on the remaining clips; *i.e.*, removing the end fastener on an SSMR panel can reduce the failure load by 42% (Schroter, 1985; Prevatt et al., 1995). At the time, BRERWULF was an innovative system that used pressure loading actuators (PLA) and rigid pressure chambers to apply spatially uniform pressures to a test specimen.

Failure testing is a sufficient tool to determine the ultimate strength of a subject, especially SSMRs. Sinno (2008) developed a failure test involving dynamic wind-induced pressures on a SSMR using electromagnetic actuators. The test setup can be seen in Figure 24. They also performed the standardized ASTM E1592 until failure on an identical SSMR specimen. Sinno (2008) sought to find a correlation between the current uniform static testing and dynamic electromagnetic testing. The correlation was in the form of an index factor as defined by the approximate equation shown in Eq.(10),

$$Index\ Factor = \frac{Clip\ Reaction\ from\ ASCE\ 7\ and\ Tributary\ Area_{\text{ASTM E1592}}}{Maximum\ Dynamic\ Clip\ Reaction} \quad (10)$$

It was found that this factor was almost proportional to

$$Index\ Factor = \frac{Failure\ Wind\ Speed^2_{\text{Dynamic}}}{Failure\ Wind\ Speed^2_{\text{ASTM E-1592}}} \quad (11)$$

or

$$Index\ Factor = \frac{Failure\ Pressure_{\text{Dynamic}}}{Failure\ Pressure_{\text{ASCE 7, Uniform}}} \quad (12)$$

The electromagnetic data were validated against wind tunnel data from UWO. The electromagnetic data were found to match the wind tunnel data temporally and spatially, and were also able to reproduce the correlation coefficients. This was the first experiment where wind tunnel loads were applied successfully to a full-scale SSMR laboratory specimen. The dynamic test failure mechanisms were found to be invariably different from their static test counterpart, and the panel deflection and deformation at the ends were much greater under dynamic loading than static uniform loading.

Figure 24: Electromagnetic uplift testing configuration on standing seam metal roof (Sinno, 2008).

Habte et al. (2015) completed an experiment at the Wall of Wind (WOW) at Florida International University (FIU). The WOW was used to generate a full-scale wind field on vertical-leg and trapezoidal SSMR systems, with and without eave trims. The results ascertained that SSMR panel deflections and failure modes under dynamic loading are different from those under uniform pressures. These results, like several aforementioned studies, suggest that dynamic loads govern the performance of the roof as compared to static uniform conditions. The most common failure mechanism was seam-clip separation due to panel deflection at the connection, as seen in Figure 25. Clip rupture and breakage was much more common than typical clip slippage, which is observed in uniform static testing. This was determined to be due to the vibration from the wind loading.

Figure 25: Clip rupture and breakage at the clip-seam connection due to panel deflection and deformation (Habte et al., 2015).

Habte et al. (2015) concluded that the code, which is based on bare deck roofing, is not representative and the roof geometry and seam profiles are critical to determining wind loads. The seam profiles and eave trims were found to affect the load distributions on the roof, with trapezoidal seam experiencing much greater suction and larger non-uniformity. This proves that architectural features can have sizeable impacts on the uplift force. In this case, ASCE 7-10 was unconservative for the trapezoidal seam in the edge zones, but more reasonable for the vertical-leg seam (Habte et al., 2015).

(a)   **(b)**
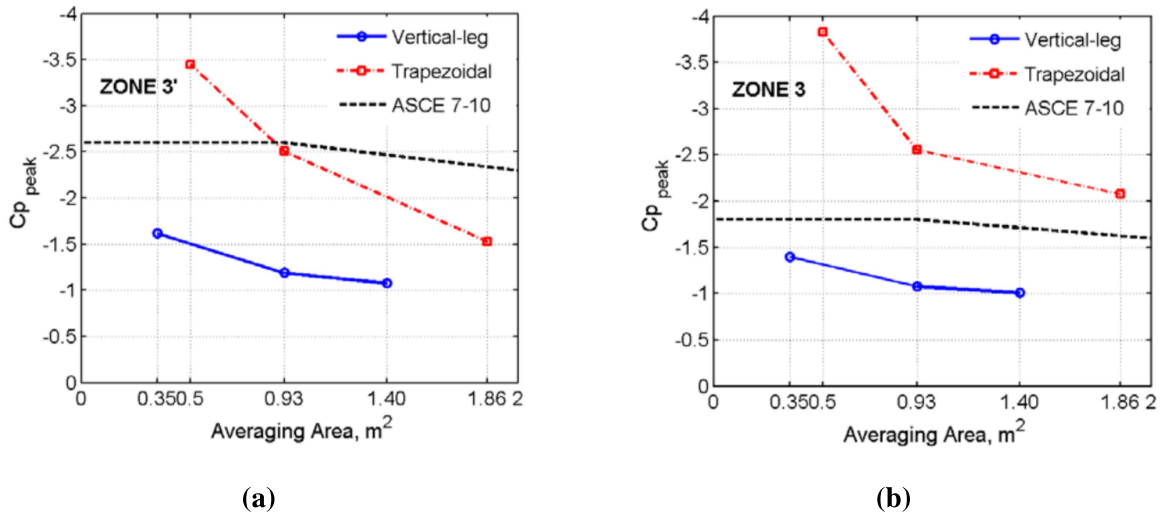
Figure 26: Experimental peak pressure coefficients plotted against area-average for (a) corner (zone 3') and (b) edge (zone 3) regions compared to ASCE 7-10 provisions (Habte et al., 2015).

From there, Azzi et al. (2020) used the WOW facility again to conduct large-scale testing on a 1:10 building model. One model had a bare deck roof (like those used to create ASCE 7 provisions) and one was outfitted with a trapezoidal seam SSMR. The bare deck pressures were verified against a full-scale model. The SSMR model also had eave and gable attachments. The models are shown in Figure 27.
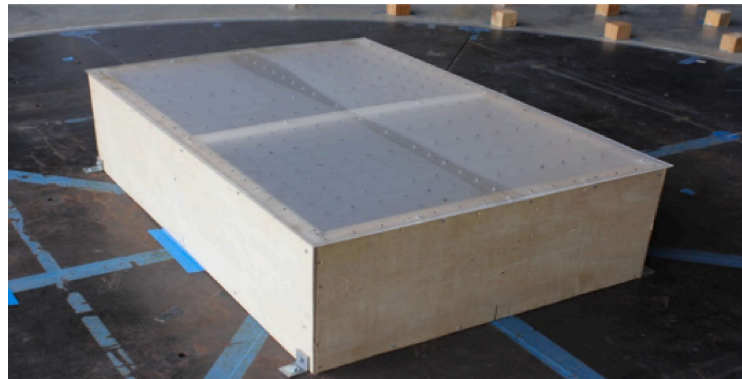
(a)
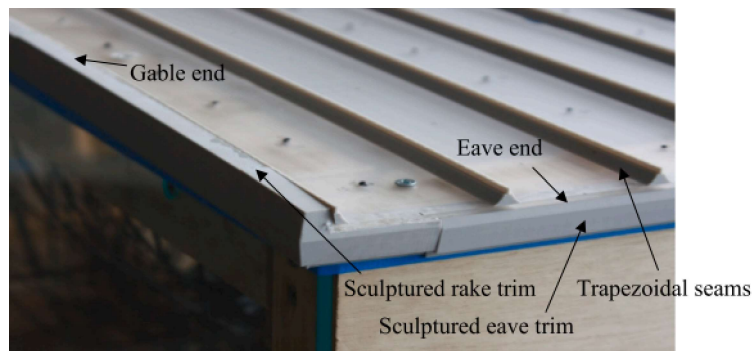
(b)

Figure 27: Photographs of the 1:10 (a) bare deck and (b) a SSMR model configurations (Azzi et al., 2020).

A wind tunnel approach was applied to correct scaling issues of the turbulence spectrum caused by the test section size. The results of this study support the previous study's findings that architectural features, namely the seams, can significantly alter the pressure distribution on the roof; peak pressure for individual taps and area-averages were reduced by as much as 70% and 45%, respectively. The attachment of eave and gable trims modified the aerodynamics along the edges and at the corners, reducing peak pressures in these zones.

40

This is likely because the standing seams hinder the formation and transport of corner vortices. Figure 28 shows the stark differences in pressure distribution comparison between the bare deck and SSMR models.

(a)   (b)
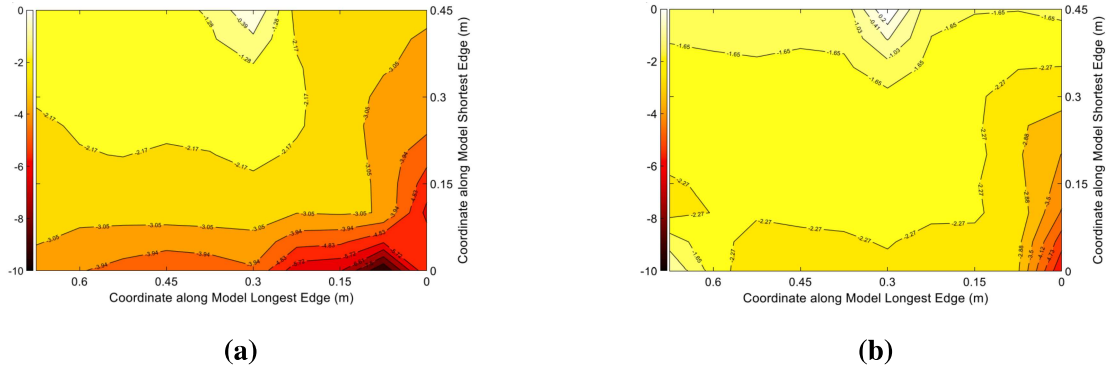
Figure 28: Contour lines of the peak pressure coefficient for (a) a bare deck configuration and (b) a SSMR configuration (Azzi et al., 2020).

2.3   Summary

High winds can cause extreme pressure fluctuations on low-rise buildings and the C&C take the bulk of these wind loads (Kopp and Morrison, 2018). The building aerodynamics along with wind-induced pressures lead to flow separation and reattachment, a major cause of damage to the roof and the cladding (Saathoff and Melbourne, 1989). Improved wind loading predictions can facilitate code amendments, and thus promote the reinforced design of components and cladding. In turn, this would reduce economic losses associated with severe wind storms while also strengthening disaster recovery efforts.

Standing seam metal roofs are an economical alternative to conventional roof systems. They are water-tight, corrosion-resistant, thermal-resistant, in addition to being expertly prefabricated. Their geometric features are able to break up vortices and therefore reduce clip loads. These attributes support the argument for more research on SSMR system behaviour. Thus, the thesis objectives will be addressed as follows: First, a model of the wind climate and corresponding wind loads on several buildings will be established and validated using wind tunnel data from Arif (2017). Then C&C responses will be calculated

and evaluated as to whether or not they are at an acceptable risk level, this will be done in three parts: (i) creating enveloped GCp vs. area curves as done in Kopp and Morrison (2018), referred to as the ASCE Method, (ii) creating the same curve as (i), but implementing the Clip Tributary Area Method, whereby using a clip influence function of 1 in the clips geometric tributary area, and (iii) creating the same curve as (i) but implementing the Influence Function Method as defined by the influence functions in Xia (2022). From this, a load adjustment factor specific to SSMR design will be calculated.

3   Experimental Database

Wind tunnel models have proven tremendously valuable in simulating flows in the atmospheric boundary layer. In the field of wind engineering most structures of interest can be classified as bluff bodies in regards to the air flow around them. Studying the flow around these bluff bodies is of fundamental importance to the design of such components and cladding.

In the current study, data from a wind tunnel test are used. The design of the building models, tap layout, and terrain simulation are described in the following sections. The velocity and turbulence intensity profiles and integral length scale are discussed. There are also discourses on wind spectrum, aerodynamic admittance, and length scale.

It should be noted that the experimental portion of this research was previously described in Arif (2017). Arif (2017) assessed the effects of upstream turbulence on local pressures on low-rise buildings of various sizes. The previous research analysis did not require scaling of the wind tunnel model into full-scale dimensions, therefore no scale was determined for length, velocity, or frequency (Arif, 2017). However, the current research considers wind loads on components and cladding, namely the clips that secure SSMR panels to the underlying purlins. This current analysis requires full-scale dimensions to be applicable in the real world. For this reason, detailed analysis of the wind tunnel scaling is conducted herein.

3.1   Model Design

Wind tunnel testing was previously carried out in Arif (2017) on two different building models that were designed and constructed to mimic the dimensions of the Texas Tech University Wind Engineering Research Field Laboratory (WERFL) Buildings as described in Levitan and Mehta (1992a, 1992b). These building models had flat roofs and the same plan dimensions (184 mm by 275 mm), but had heights of 78 mm and 234 mm in model-

scale height denoted as H1 and H2, respectively. The dimensions are shown in Figure 29.

(a)   **(b)**
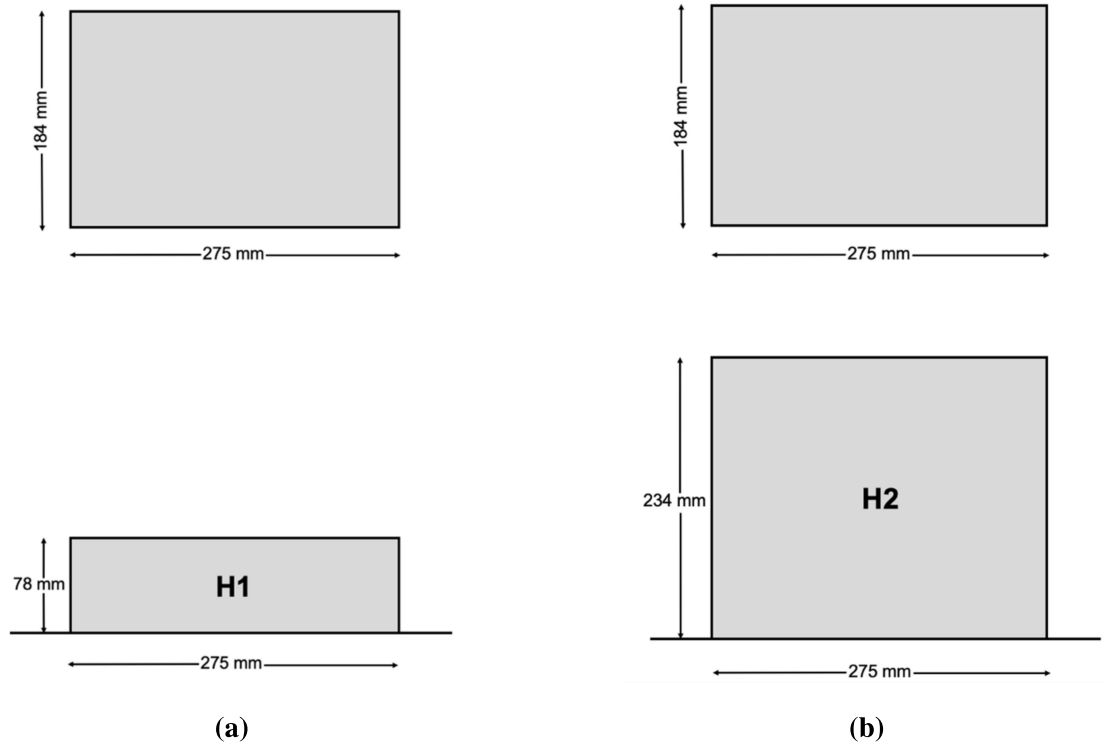
Figure 29: Dimensions of building model (a) H1 = 0.078 mm and (b) H2 = 0.275 mm.

Each model was used in combination with one or more "dummy" blocks of same height to achieve different building plan configurations. There were four different plan configurations (denoted as B1 through B4) considered for the two building heights, for a total of eight building models. The various plan configurations can be seen in Figure 30. The detailed dimensions and wall aspect ratios are outlined in Table 1.
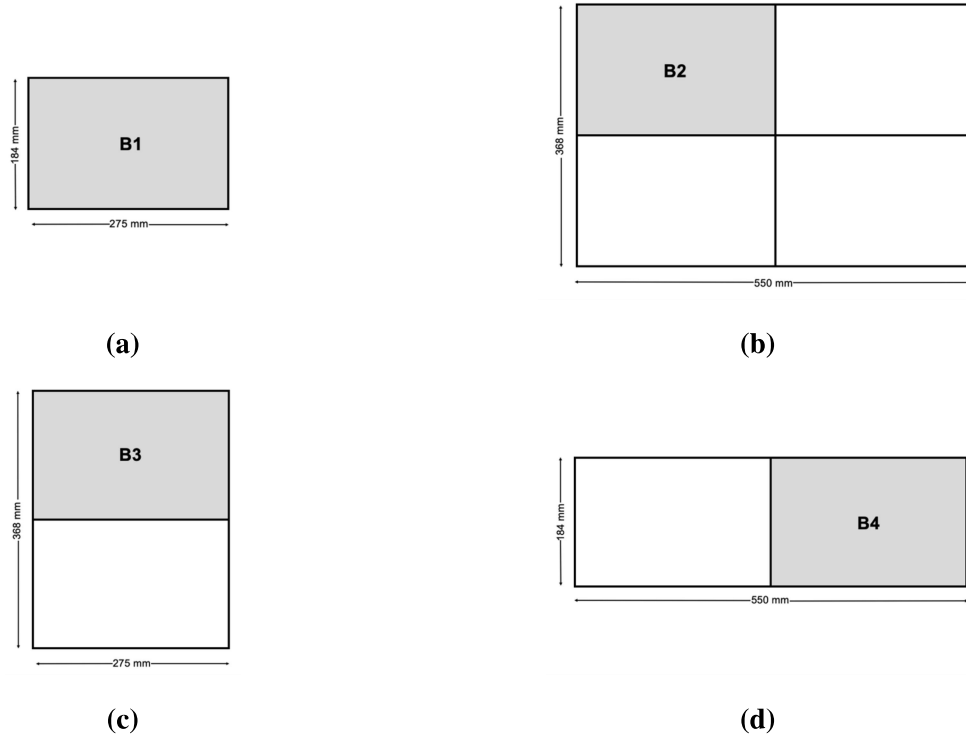
Figure 30: Plan configurations for models (a) B1, (b) B2, (c) B3, and (d) B4. The "dummy" blocks are filled in white.

Table 1: Model Dimensions and Aspect Ratios

Model	Plan Dimensions		Height (mm)	Aspect Ratio	
	Smaller, B	Larger, L		H/B	H/L
B1-H1	184	275	78	0.42	0.28
B1-H2	184	275	234	1.27	0.85
B2-H1	368	550	78	0.21	0.14
B2-H2	368	550	234	0.64	0.43
B3-H1	275	368	78	0.28	0.21
B3-H2	275	368	234	0.85	0.64
B4-H1	184	550	78	0.42	0.14
B4-H2	184	550	234	1.27	0.43

3.2 Tap Layout

Pressure taps on the building models measure the instantaneous surface pressure, this allows for an analysis of the wind loading. The pressure taps were situated in an evenly spaced grid on the roof surface of the building block models so that pressure contours could convey the effects of wind on the roof. There were no pressure taps on the walls of the building models and no pressure taps on the "dummy" blocks. There was a total of 950 pressure taps on a removable panel with 25 taps along the shorter length, B, and 38 taps along the longer plan dimension, L. The taps were placed in a uniformly distributed grid of 7.35 mm in the longer plan dimension and 7.54 mm in width dimensions, with a distance of 1.50 mm from the edge in both plan dimensions. The tap grid spacing can be seen in Figure 31. Since there was no predetermined length scale, it was acknowledged that the quality of the full-scale tap resolution was dependent on the scale chosen in this analysis.

(a)   (b)
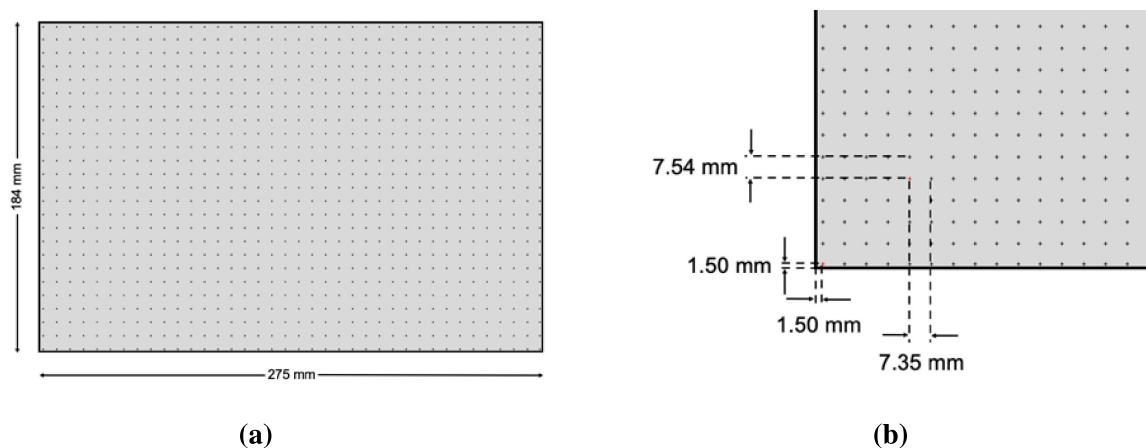
Figure 31: Tap layout and grid spacing of the (a) entire building block, and a (b) magnified image with measurements.

The pressure data were collected at 625 Hz for 120 seconds at every wind angle listed in Table 2. The wind directions with respect to the model are shown in Figure 32. Details of the pressure tap, scanners, and tubing systems at the Boundary Layer Wind Tunnel are described in Ho et al. (2005).

Table 2: Experimental Wind Directions

Model	Wind Angle	Interval
B1–H1	0–90°	10°
B1–H2	0–90°	10°
B2–H1	0–360°	10°
B2–H2	0–360°	10°
B3–H1	0–90°	10°
B3–H2	0–90°	10°
B4–H1	0–180°	10°
B4–H2	0–180°	10°

(a)

(b)

(c)

(d)
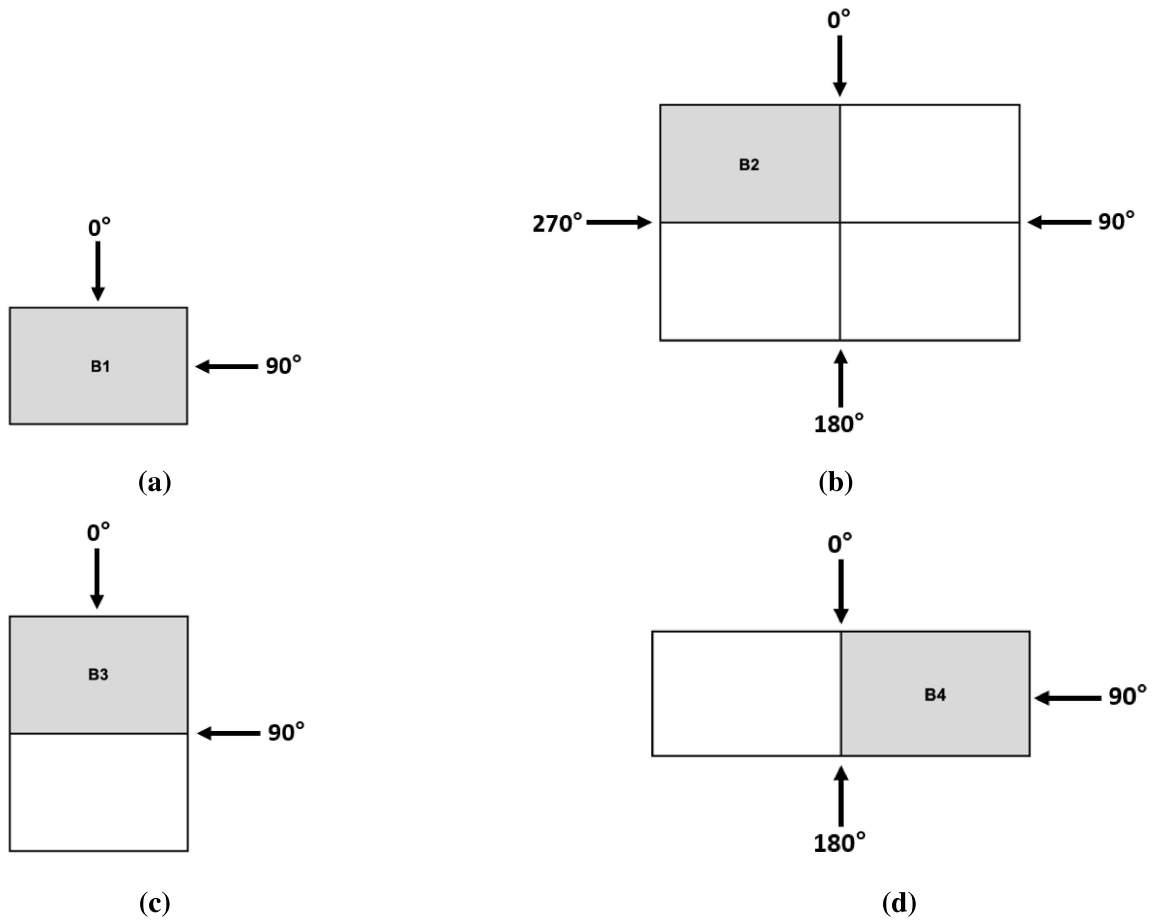
Figure 32: Wind angles used for models (a) B1, (b) B2, (c) B3, and (d) B4. The "dummy" blocks are filled in white.

47

3.3   Terrain Simulation

Upstream flow conditions are essential to characterizing bluff body aerodynamics in different terrains. The BLWT at the University of Western Ontario (UWO) employs a test section that measures 2.4 m by 3.4 m in cross-sectional breadth and 39 m in upstream fetch. Various terrain conditions can be simulated in the BLWT using roughness blocks, spires, and barriers. The Arif (2017) experiment considered three different terrain exposures: open water ('1'), open country ('2'), and suburban ('3'). These closely replicated the terrain used in Akon and Kopp (2016).

For each terrain, the ground roughness configuration was the same, but the terrain was tested with and without a 0.38 m tall barrier at the upstream entrance. These terrains are denoted as follows: no barrier ('S') and barrier ('L'). As shown in Akon and Kopp (2016), the presence or lack of large turbulence-producing elements governs the size of the integral length scale, a parameter indicative of the flow characteristics in a given terrain; The "no barrier" case ('S') should typically have a smaller integral length scale, since there are only roughness blocks present, which can only produce small vortices or eddies. Conversely, the barrier case ('L') produces larger integral scales as it captures the turbulence from barrier (Akon, 2017). The effects of the barrier on the velocity profile, turbulence intensity, and integral length scale are discussed in the following section. For the current research, only the open country cases with the barrier (denoted as '2L') were used.

Within the BLWT, the building model is placed on the turntable so that it can be easily rotated to different angles of attack. The range of wind directions tested for each building model are included in Table 2. These wind directions were chosen based on the symmetry and configuration of the plan and they allow for the pressure coefficients over the entire roof to be measured for 0°–90°. The wind angles were measured in intervals of 10°.

3.4 Velocity and Turbulence Intensity Profiles

The velocity profile displays the distribution of wind speed along the height of the ABL. There are characteristic velocity profiles for given terrains, which are used for comparison in this study. The turbulence-generating elements (*e.g.*, roughness blocks, barriers) had been configured in a way so that the desired velocity profiles could be achieved (Akon, 2017). The velocity measurements were recorded without the model in the tunnel. During testing, the Cobra probe was positioned behind the turntable, on the leeward side of the model. This positioning minimizes the impact of the probe wake on the pressure readings.

There are insufficient data from Arif (2017) to create a full velocity profile. The measurements were collected at three locations: the static pitot tube to measure upper-level dynamic pressure at the standard reference height of 1.47 m and a Cobra probe at both building heights, H1 and H2. However, the experimental testing implemented both a model and a set of terrain conditions that were reasonably similar to those described in Akon and Kopp (2016). With both data sets available, a comparison of the velocity and turbulence intensity profiles was completed. The turbulence intensity, I_U, is defined as

$$I_U = \frac{\sigma_{U_H}}{\bar{U}_H} \tag{13}$$

Turbulence intensity is a measure of wind speed fluctuations in the wind tunnel, and as such the definition of σ_{U_H} in Eq.(13) is the standard deviation of the wind speed, U_H, at the building height. The mean value of the wind speed time history is denoted as $\bar{U}_H$. This comparison is presented in Figure 33, and it ensures the current analysis could be completed with the velocity data from Akon and Kopp (2016).
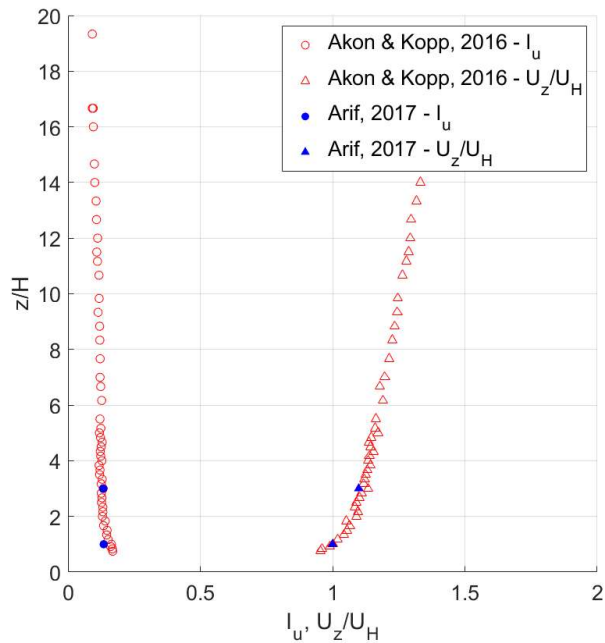
Figure 33: Turbulence intensity and velocity profiles for an open country terrain ('2L').

The turbulence intensity, seen in Figure 33, is not significantly affected by the presence or lack of barrier for open country terrain. This conclusion is also drawn in Guo (2021). The numerical values are shown in Table 3. It can be seen in Figure 33, that although the normalized velocity profile of the current data agree well with those of Akon and Kopp (2016), the turbulence intensity is notably lower in the current data set at H1 (Table 3 for reference). The mismatch in turbulence intensity was deemed likely a result of different physical characteristics (*e.g.*, cleanliness of the screens, upstream of the wind tunnel contraction) in the wind tunnel, since the experiments were conducted several years apart.

The mean model height wind speed are outlined in Table 4. These wind speeds were recorded at model height without the model in the tunnel. It is observed that wind speeds in the current experiment are approximately 40% higher than that of Akon (2017) (also used in Akon and Kopp (2016)), which may have resulted in larger error of the latter data set. It has been proven through wind tunnel testing completed by Kwan (2020), that when the wind

50

speed at model height decreases, the uncertainty of the measuring instrument increases. Because of this phenomena, low-rise wind tunnel simulations should be run at higher wind speeds with careful consideration to not incur vibration on the Cobra probe or mast (Kwan, 2020). However, this was determined after the previous works by Akon and Kopp (2016). To prove that the data remained valid and the pressure coefficients were unaffected, the turbulence characteristics were investigated further. This was done by assessing the integral length scales between experiments and then by comparing spectra.

Table 3: Turbulence Intensity Comparison

Height	Terrain	Barrier (m)	I_u (%) (Arif, 2017)	I_u (%) (Akon and Kopp, 2016)
H1	2L	0.38	14	17
H2	2L	0.38	13	13

Table 4: Mean Roof Height Velocity Comparison

Height	Terrain	Barrier (m)	$\bar{U}_H$ (m/s) (Arif, 2017)	$\bar{U}_H$ (m/s) (Akon and Kopp, 2016)
H1	2L	0.38	12.62	7.46
H2	2L	0.38	13.86	8.45

3.5 Integral Length Scale

Integral length scale, L_u, is a measure of the average size of the largest turbulent vortices in the upstream flow. The turbulent vortices are referred to as eddies and they are rotating flow structures that are assumed to move at a speed approximately equal to the mean velocity. In the wind tunnel, small eddies can be simulated by features like roughness blocks and nuts, whereas large eddies are recreated by larger turbulence-producing elements, like a barrier. The integral length scale is the product of the integral time scale, T_u and the mean wind velocity, $\bar{U}$, such that

$$L_u = T_u \bar{U} \tag{14}$$

51

The integral time scale is the integral of the the auto-correlation function, $R(\tau)$, for the along-wind direction with respect to a time lag, τ, as can be seen below

$$T_{\mathrm{u}} = \int_0^{\tau_0} R(\tau)\,d\tau \tag{15}$$

The value of τ_0 is the time at which the auto-correlation function first equals zero. The fluctuating wind speed at time t is denoted as $U'(t)$. The auto-correlation function is defined by

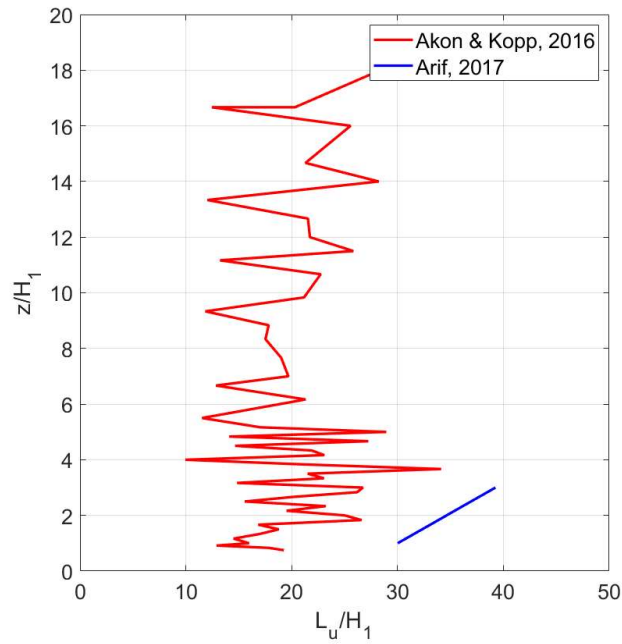$$R(\tau) = \frac{\overline{U'(t)U'(t+\tau)}}{\sigma_{\mathrm{U}}{}^2} \tag{16}$$

Figure 34: Integral length scales against normalized height for an open country terrain ('2L').

The integral lengths for Akon and Kopp (2016) and Arif (2017) are shown in Figure 34, with values provided in Table 5. Subscript 'x' in Table 5 denotes the height used as outlined in the first column, either H1 or H2.

Table 5: Integral Length Scale Comparison

Height	Terrain	Barrier (m)	L_u/H_x (Arif, 2017)	L_u/H_x (Akon and Kopp, 2016)
H1	2L	0.38	30	11
H2	2L	0.38	7	5

The results of Akon and Kopp (2016) indicate that when the barrier is present, the integral length increased. Overall, the integral length scales are, on average, 219% larger in the current data set than in Akon and Kopp (2016). The mean roof height velocity is larger in the current data set as well, while the turbulence intensities are lower for the H1 building model. The magnitude of the peak pressure coefficients increase with integral length scale and turbulence intensity (Saathoff and Melbourne, 1989). However, the data convey both an increased integral length scale and decreased turbulence intensity, so the effects are studied by plotting the power spectral density. Matching spectra between experiments is of greater importance for low-rise building wind load analyses.

3.6 Velocity Spectra

The power spectral density of the fluctuating longitudinal velocity, or spectra, is an expression of the energy content of wind in the atmospheric boundary layer. In other words, the spectra describes the turbulence, and turbulence is significant to wind loading on low-rise buildings. The velocity must be measured at the appropriate height during the wind tunnel tests, without the model in the tunnel. In Akon and Kopp (2016), the mean stagnation point on the windward wall for low-rise buildings, regardless of turbulence properties, is approximately 0.65H, where H is the height of the building. In this case, the appropriate height is a proxy to the height of the actual stagnation point and can be assumed to be the eave height of the building. In Arif (2017) the sampling frequency was set as 625 Hz, whereas Akon and Kopp (2016) sampled at 1250 Hz. The spectra for both model heights are compared between experiments in Figure 35.
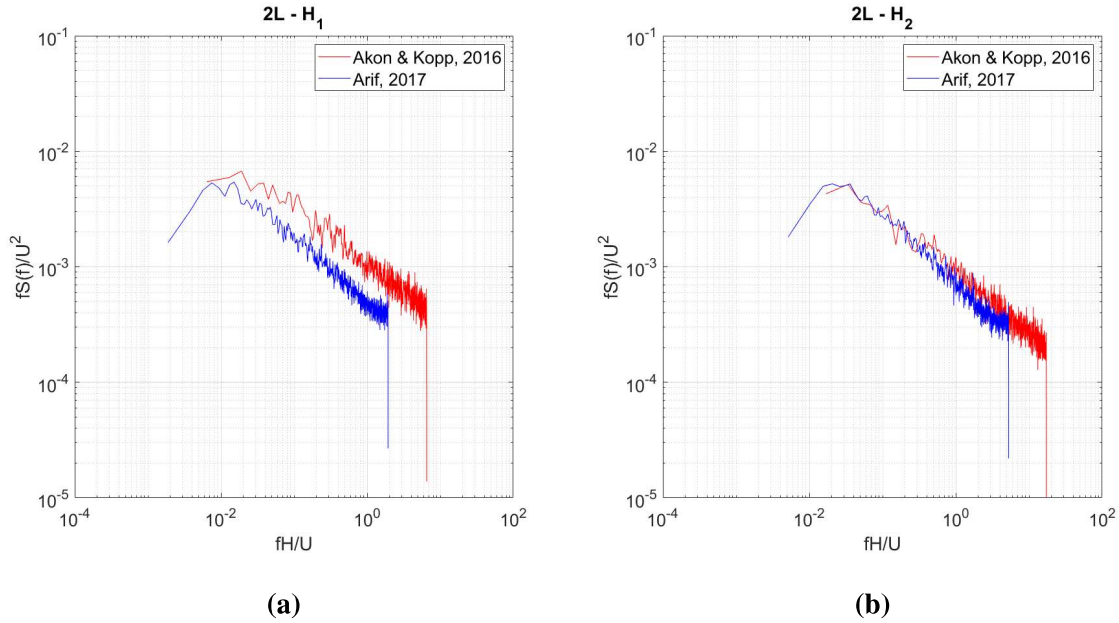
Figure 35: Power spectral density for an open country terrain ('2L') at heights (a) H1 and (b) H2.

It is most important that the peak values align at similar frequencies. The shape matches well between experiments, but the low turbulence intensity of 14% at H1 in Arif (2017) results in decreased spectral density function when compared to Akon and Kopp (2016) of 17% at H1. The spectra at H2 in the open country terrain (Figure 35(b)) shows a reasonable match. This is a result of the turbulence intensities matching ($\tilde{1}$3% as listed in Table 3) between experiments and the integral length scales are small in magnitude compared to other terrains and model heights (refer to Table 5). To provide more context, the spectra in the current experiment was validated by comparing the aerodynamic admittance for a model in the current experiment to the aerodynamic admittance for a model of similar aspect ratios from the NIST database.

3.7   Aerodynamic Admittance

To bolster the argument that the data are adequate, the aerodynamic admittance was plotted. Aerodynamic admittance is a function correlating velocity fluctuations over the area

54

of a structure, in this case this structure is a low-rise building (Wang and Kopp, 2021a). To ensure the pressure coefficients were not affected by the low turbulence intensity, the aerodynamic admittance, $\chi^2(f)$, was plotted for the B1-H1 model for the an country terrain ('2L'). The equation for aerodynamic admittance is defined as

$$S_{\text{P}}(f) = 4\frac{\bar{P}^2}{\bar{U}^2}S_{\text{U}}(f)\chi^2(f) \tag{17}$$

The pressure spectra and velocity spectra in Eq.(17) were determined for the data set. The mean pressure, $\bar{P}$, is the product of the mean dynamic pressure at the roof height, $\bar{q}_{\text{H}}$, and the mean area-averaged pressure coefficient, $\bar{C}p_{\text{AA}}$, shown as

$$\bar{P} = \bar{q}_{\text{H}}\bar{C}p_{\text{AA}} \tag{18}$$

To calculate the mean dynamic pressure at the roof height, use

$$\bar{q}_{\text{H}} = \frac{1}{2}\rho\bar{U}_{\text{H}}^2 \tag{19}$$

The air density in Eq.(19), ρ, was assumed to be 1.225 kg/m^3.

The mean area-averaged pressure coefficient is the time-average of the area-averaged pressure coefficients, Cp_{AA}. In this case, the area-averaged pressure coefficient is a ratio of the summation of the weighted mean of a taps pressure coefficient, Cp_{i}, and its tributary area, A_{i}, to the total area under consideration, A_{total}. In Eq.(21), subscript i denotes the pressure tap in the area, A. In Eq.(20), subscript j is the number of samples or the product of the frequency and the sampling time, such that

$$\bar{C}p_{\text{AA}} = \frac{\sum_{j=1}^{m} Cp_{\text{AA}}(t)_{\text{j}}}{m} \tag{20}$$

$$Cp_{\text{AA}}(t) = \frac{\sum_{i=1}^{n} Cp_{\text{i}}(t)A_{\text{i}}}{A} \tag{21}$$

The values were calculated for the centreline taps (shown in red of Figure 36) of an area

of the shortest length, B by B, at a wind angle parallel to the ridge. A simplified diagram of this is in Figure 36 for understanding. The velocity spectra were obtained at the roof height as this was the only velocity time history available for the current data. These values were compared to the aerodynamic admittance function of open country model, 'eg1', from the NIST database. The models shared similar aspect ratios as outlined in Table 6. An empirical model from Vickery (1965) for aerodynamic admittance was also plotted for reference (Vickery, 1965). Details of these calculations can be found in Wang and Kopp (2021a).
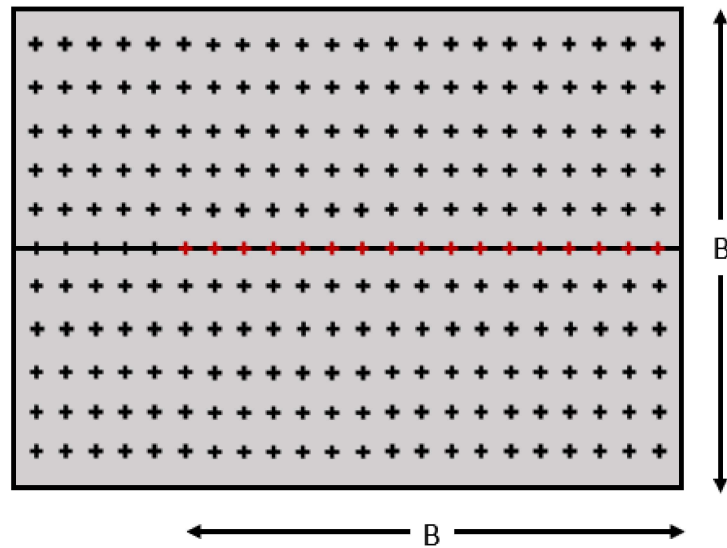

Figure 36: Diagram of centreline taps used in aerodynamic admittance calculations.

Table 6: Aspect Ratio Comparison of Models

Model	Roof Slope	H	B	L	H/B	H/L	B/L
B1-H1	0	78 mm	184 mm	275 mm	0.42	0.28	0.67
eg1	1:12	32 ft	80 ft	125 ft	0.40	0.28	0.64

The results of the aerodynamic admittance are plotted in Figure 37 for the open country terrain. It is relevant to note that in the case of the eg1 NIST model, there was only one open country terrain simulated in the wind tunnel. The aerodynamic admittance of the models show fair agreement and it can be concluded that the differences in turbulence

intensity are justified and are considered within reasonable range. The noticeable spike is likely due to the rotation frequency of the wind tunnel fan. The process selecting a length scale is described in detail in the next section.
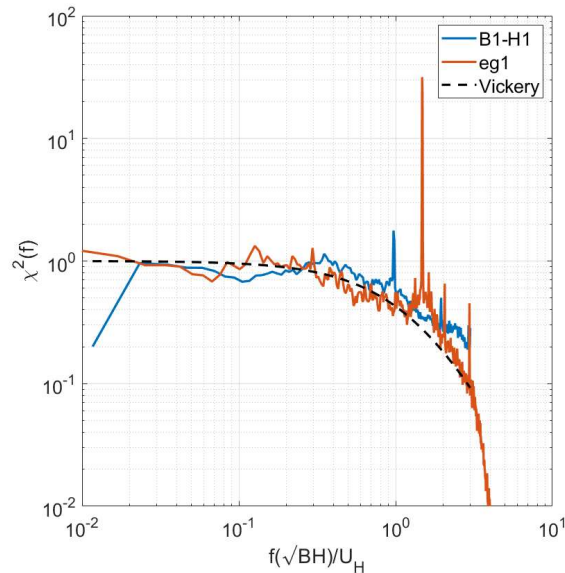

Figure 37: Aerodynamic admittance functions for an open country terrain ('2L').

3.8   Length Scale

As noted above, the previous works completed by Arif (2017) did not require full-scale dimensions; thus, all calculations were completed in model-scale. However, a scale is necessary to determine the sizing of the roof panels in the current study. The first step in establishing the scale is obtaining dimensions of the models under consideration. In this case, the model dimensions were provided and were identical to that of the TTU WERFL building (Levitan and Mehta, 1992a; Akon and Kopp, 2016). Following this, there is a matching process for the velocity spectra of the current experiment to the ESDU velocity spectra.

As previously described, the wind speed time history was extracted from the raw data files and validated against the wind speed time history to the Akon and Kopp (2016) experiment of the same terrain. Charts were created of the height above ground normalized by the

model height versus the mean wind speed normalized by the wind speed at the model height for both experiments. The non-dimensional velocity profiles showed similar trends, yet the dimensional values of the mean wind speed were significantly greater in Arif (2017) than in Akon and Kopp (2016) as outlined in Table 4.

A plot of turbulence intensity was graphed. The turbulence intensity profile did not show agreement between experiments, with observations that Arif (2017) recorded lower turbulence intensities than Akon and Kopp (2016) at H1. The aerodynamic admittance functions were plotted for Arif (2017) and for the NIST eg1 model to confirm the difference had no influence on the pressure coefficients, B1-H1 was within a reasonable range of the NIST eg1 values (Akon and Kopp, 2016; Arif, 2017). The non-dimensional power spectral density of fluctuating velocity was then plotted using the measured data alongside a plot of the power spectral density produced with ESDU 74031 and 85020 procedures, herein referred to as the 'ESDU plot'. The ESDU plot is derived from the Von Karman spectral equations and empirical equations shown in Eq.(22) – Eq.(25) (ESDU, 1974; ESDU, 2001).

ESDU 85020, A2.1:

$$\frac{nS_{\mathrm{uu}}}{\sigma_{\mathrm{u}}{}^2} = \frac{n_{\mathrm{u}}}{(1 + 70.8n_{\mathrm{u}}{}^2)^{5/6}}; \quad n_{\mathrm{u}} = \frac{L_{\mathrm{u}}n}{\bar{U}_{\mathrm{H}}} \tag{22}$$

ESDU 74031, A.16:

$$L_{\mathrm{u}} = 25\frac{\tilde{z}^{0.35}}{z_{\mathrm{o}}{}^{0.063}} \tag{23}$$

ESDU 74031, A.4a:

$$F_{\mathrm{u}} = \lambda[0.867 - 0.556log_{10}z - 0.246(log_{10}\tilde{z})^2] \tag{24}$$

ESDU 74031, A.4b:

$$\lambda = 1.0 \quad for \quad z_{\mathrm{o}} \le 0.02m$$
$$\lambda = \frac{0.76}{z_{\mathrm{o}}{}^{0.07}} \quad for \quad 0.02m < z_{\mathrm{o}} \le 1.0m \tag{25}$$

When matching spectra it is important that peak values of the ESDU plot align at a similar

non-dimensional frequency ($f \frac{H}{U_H}$) to the experimental spectra; the length scale and aerodynamic roughness are chosen so that the peaks align along the x-axis. This is due to the nature of the the wind spectrum, which expresses major energy peaks and, thus, represents fluctuations in the mean wind speed. In the event that the plots do not match, the turbulence intensities are examined for both cases, as lower turbulence intensity can produce decreased spectral values. In addition to reviewing turbulence intensity, the length scale can be adjusted to greater or less than the assumed length scale or the aerodynamic roughness can be reasonably modified within it's current order of magnitude. The effects of changing the surface roughness and the length scale were investigated.

3.8.1 Effect of Length Scale

Length scales of 1:50, 1:100, and 1:200 were plotted in accordance with ESDU procedures. These plots display the effect of length scale on the ESDU spectra. An aerodynamic roughness was set as 0.03 m, suitable for open country terrain. The full-scale building height was calculated based on length scale previously assumed. The measured spectra plot was graphed against the three ESDU plots. The plot in Figure 38 displays the spectra at heights H1 and H2, respectively. Figure 38 demonstrates that spectra at the lower model height deviate further from the ESDU plot, a result of the very small model height in reference to the turbulent element and static pitot configurations in the wind tunnel.
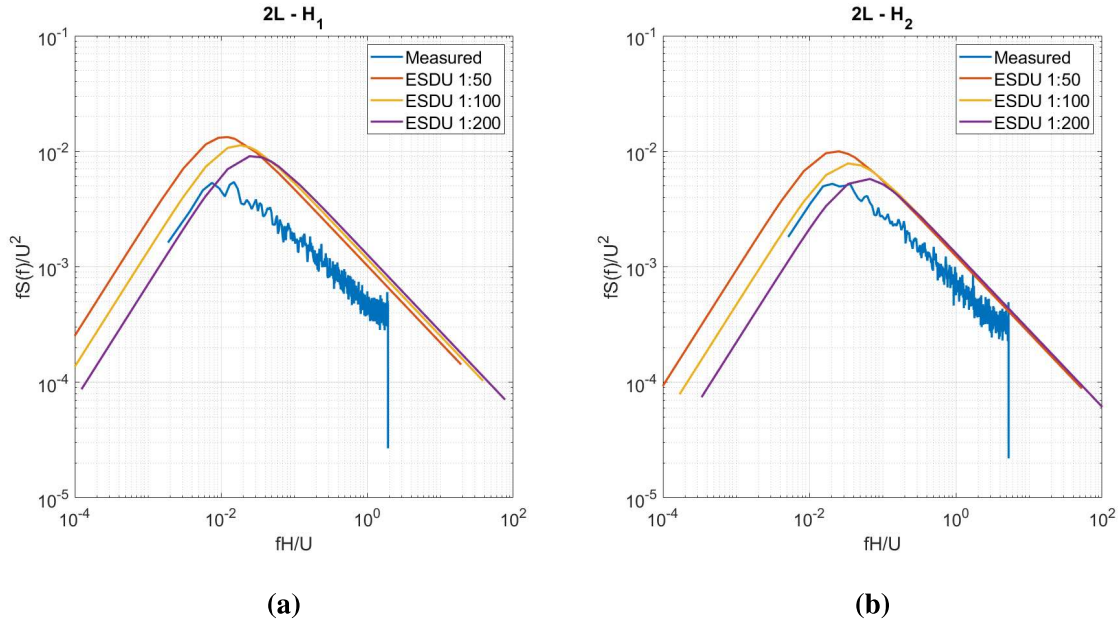
Figure 38: Experimental and ESDU spectra for 1:50, 1:100, and 1:200 scales for an open country terrain ('2L') with z_o = 0.03 m at heights (a) H1 and (b) H2.

Smaller length scales (*e.g.*, 1:50) defined by ESDU produce larger spectral values that tend to peak at lower frequencies compared to those of larger length scales. However, for all length scales the spectra tend to collapse into the same linear trend after the peak. The peaks of the charted spectra in Figure 38 most closely resemble a 1:50 length scale based on the locations of the peaks.

Despite ESDU providing detailed procedures to plot spectra, the values from these provisions are considered a guideline and will not show an exact representation, thus the experimental data will not always conform to ESDU estimations. This is potentially due to effects of Reynolds number scaling (Azzi et al., 2020). Holmes and Best (1981) also proved this when they compared their experimental spectra to the Von Karman spectrum, with a length scale derived from ESDU for open country terrain. The turbulence scales were much larger than the dimensions of the model, and so the wind tunnel spectrum was shifted by a factor of approximately 2. The authors concluded that this shift was not believed to have a significant effect on the measured pressure coefficients (Holmes and Best, 1981).

60

3.8.2 Effect of Aerodynamic Roughness

A length scale of 1:50 was assumed and spectra were graphed for the aerodynamic roughness values of 0.01 m, 0.02 m, and 0.03 m. Figure 39 outlines the effect of surface roughness on the wind spectrum.
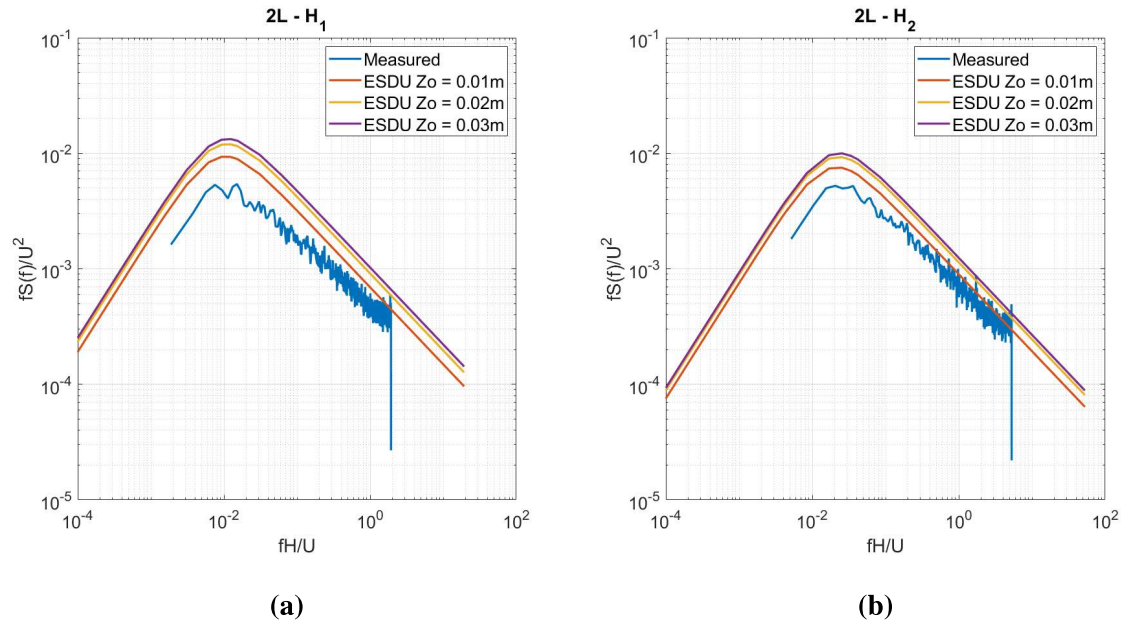

Figure 39: Experimental and ESDU spectra at H2 for z_o of 0.01 m, 0.02 m, and 0.03 m at 1:50 length scale for an open country terrain ('2L') at heights (a) H1 and (b) H2.

The overall effect of the aerodynamic roughness tend to be most visible at the peak and tail, or reduced frequencies greater than 10^{-2}. The open country terrain appears to have an approximate z_o value of 0.01 m. Although this value implies a very smooth terrain, it it still recognized as an open terrain (Liu et al., 2021). Conversely, while this terrain is deemed open country in the current study and in Akon and Kopp (2016), Browne et al. (2013) considered their terrain of the same turbulence intensity ($I_u = 16\%$) to be suburban. This may have been a consequence of potentially mismatched scales in Browne et al. (2013) and ultimately have had impacts on the pressure coefficients, as would a small integral length scales (Saathoff and Melbourne, 1989). The final length scale was set as 1:50 and the aerodynamic roughness as 0.01 m. The models used in the SSMR roof simulations are

outlined in Table 7. Only the 2L terrain was considered, this terrain is an open country terrain with a barrier present in the wind tunnel.

Table 7: Full-Scale Dimensions of Building Models

Model	Plan Dimensions (m)		Height (m)	Roof Area (m²)
	Smaller, B	Larger, L		
B1-H1	9.2	13.75	3.9	126.5
B1-H2	9.2	13.75	11.7	126.5
B2-H1	18.4	27.5	3.9	506
B2-H2	18.4	27.5	11.7	506
B3-H1	13.75	18.4	3.9	253
B3-H2	13.75	18.4	11.7	253
B4-H1	9.2	27.5	3.9	253
B4-H2	9.2	27.5	11.7	253

3.9   Summary

The normalized velocity profile matches well between the experiments, but the turbulence intensity at H1 is lower in the current experiment. The integral length scale was much larger overall in Arif (2017), but showed no trend with the presence of the barrier. This could be due to many physical factors within the wind tunnel as the experiments were completed years apart. The peak pressure coefficients become more negative as turbulence intensity and integral length scale increase (Saathoff and Melbourne, 1989). However, these data experienced both decreased turbulence intensity and increased integral length scale; thus, the impacts were analyzed by plotting the spectra. The spectra is of most importance to low-rise building simulations and it showed that although open country terrain had consensus with the Akon and Kopp (2016) experiment, the spectra did not match at H1 due to the low turbulence intensities. Regardless, the resulting aerodynamic admittance demonstrated an overlapping trend to a NIST model of similar aspect ratios. From the in-depth analysis and

62

comparative study of Arif (2017) and Akon and Kopp (2016) it was decided that a length scale of 1:50 and an aerodynamic roughness of 0.01 m would be used in the analysis.

4 Modelling Approach and Analysis

This chapter discusses the preliminary analysis used to obtain pressure coefficients from wind tunnel testing. It elaborates on the modelling approach, including roof design, influence functions, and effective tributary area. There is a validation to the Kopp and Morrison (2018) study to confirm the analysis approach. As previously mentioned, the current research takes three different modelling approaches that were presented in Chapter 1, they are listed as:

- ASCE Method: Determination of wind loads on a roof using typical area-averaging methods and peak value analyses, taking the worst values considering all wind directions and locations (within each zone). This method ignores the SSMR clips location.

- Clip Tributary Area Method: Determination of wind loads on clips of SSMR. This assumes SSMR construction with influence functions of 1 in the clip geometric tributary area. It is a code-based approach for fixed, known panel locations. This is also referred to as the 'CTA Method'.

- Influence Function Method: Determination of wind loads on clips of SSMR. This assumes SSMR construction with influence functions as defined in Xia (2022). Also referred to as the 'IF Method'

These various analyses will be discussed later in this chapter.

4.1 Pressure Coefficients

Pressure coefficients present aerodynamic pressures in terms of dimensionless variables. In this research, pressure distributions show how pressure changes spatially. The knowledge of pressure coefficients aids in creating inclusive and realistic design standards. In Arif (2017), a database of time histories for 950 individual taps at 625 Hz was collected. These are the same data that are considered in the present study. To obtain representative pressure coefficients for a low-rise building, the recorded values must be adjusted in order to be

compared to a design standard. In this case they were adjusted by: (i) a roof height velocity ratio, (ii) a statistical extrapolation, (iii) and a conversion factor in order to obtain the necessary peak values. Note that 'peak' refers to the minimum peak pressure coefficient, or in other words, the greatest suction or uplift. Higher peaks refer to greater suctions.

4.1.1 Roof Height Velocity Ratio

The pressure coefficients collected in the wind tunnel are referenced to the height of the static pitot tube at 1.47 m. The pressure coefficients at the reference height are normalized to the roof height of the wind tunnel model by a factor referred to as the Roof Height Velocity Ratio (RHVR). The RHVR is the ratio of the mean wind speed measured at the reference height, $\bar{U}_{ref}$, to the mean wind speed at the roof height, $\bar{U}_{H}$. The corrected pressure coefficients, Cp, are the product of the reference height pressure coefficient, Cp_{ref}, and the square of (RHVR), as shown in Eq.(27) and Eq.(26):

$$(RHVR) = \frac{\bar{U}_{ref}}{\bar{U}_{H}} \tag{26}$$

$$Cp = Cp_{ref}(RHVR)^2 \tag{27}$$

The values of the mean velocities and (RHVR) are outlined in Table 8 for an open country terrain ('2L').

Table 8: Model Roof Height Velocity Ratios

Height (mm)	$\bar{U}_H$ (m/s)	$\bar{U}_{ref}$ (m/s)	RHVR
H1	12.62	16.12	1.28
H2	13.86	17.22	1.24

4.1.2 Area-Averaging

Once the pressure time histories are corrected to roof height, they are area-averaged. This step is for calculating design wind loads of components and cladding. Area-averaging has

65

been used in several previous studies and is the standard approach for determining design loads (Kopp et al., 2005; Farquhar et al., 2005; Kopp et al., 2012). All pressure taps are assigned an area, which is half the distance to the adjacent taps in both directions. This can be seen in Figure 40.
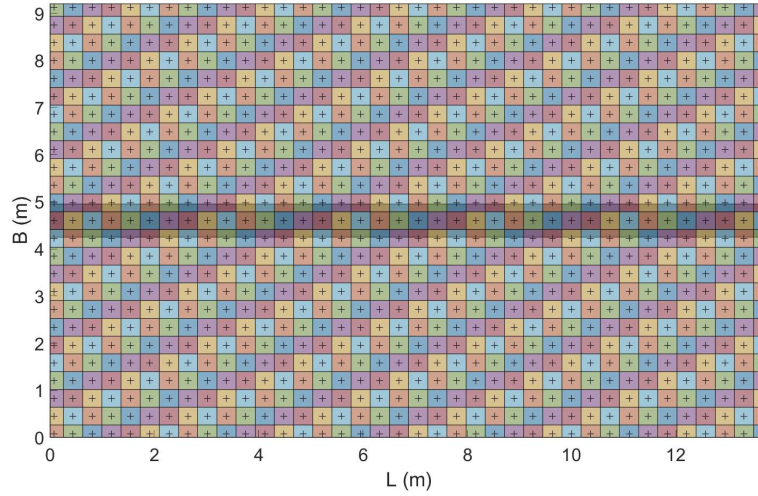

Figure 40: Taps and their tributary areas for building B1-H1. Taps are denoted as '+' and ridge cap is shaded.

The general form of area-averaging is,

$$Cp_{\text{AA}}(t) = \frac{\sum_{i=1}^{n} Cp_{\text{i}}(t) A_{\text{i}}}{A} \tag{28}$$

The area-averaged pressure coefficient, Cp_{AA}, is the summation of the the pressure coefficient at tap i, Cp_{i}, and its assigned area, A_{i}, that falls within the area under consideration, A.

In the ASCE Method, A is a square area with size $\sqrt{A}$ by $\sqrt{A}$. The Cp_{AA} is calculated for each area, A. The datum of the first square is the windward corner. The squares overlap as to capture every possible area using the tap layout.

In the Clip Tributary Area Method, the SSMR panels and clips are laid out and the area-averaged pressure coefficient is calculated for each clip location. The total area under

consideration is the clip geometric tributary area, A_{g}, which is discussed in Section 4.4.1. This is expressed as

$$Cp_{\mathrm{AA}}(t) = \frac{\sum_{i=1}^{n} Cp_{\mathrm{i}}(t)A_{\mathrm{i}}}{A_{\mathrm{g}}} \qquad (29)$$

In the Influence Function Method, the area-average pressure coefficient is also calculated for each clip. The total area under consideration is the influenced surface based on the influence function, which is discussed in Section 4.4.2. However, instead of being divided by the total area under consideration, it is divided by the clip geometric tributary area. This normalization allows for the direct comparison of GCp values between the CTA Method and the IF Method.

4.1.3 Statistical Extrapolation

Once the pressure coefficients are area-averaged, they are adjusted to obtain the statistical peak values. Instead of presenting the absolute highest peak area-averaged pressure coefficient, this work presents the statistical peak area-averaged pressure coefficients, $\check{C}p_{\mathrm{AA}}$. This method has been employed in many papers (*e.g.*, Lin and Surry, 1998; Ho et al., 2005; Morrison and Kopp, 2018), since it can provide more statistically stable values compared to measured peaks that are associated with particular probability levels. The statistical peak area-averaged pressure coefficients are found by dividing the pressure time history into 10 segments. The peaks from the segments are extracted and fit to a Gumbel distribution using the Lieblein BLUE (Best Linear Unbiased Estimator) method (Lieblein, 1974; Cook et al., 1988). This is generally represented as,

$$\check{C}p_{\mathrm{AA}} = \mu_{\mathrm{T}} - \alpha_{\mathrm{T}}[ln(ln(1/P))] \qquad (30)$$

where μ_{T} is a location parameter and α_{T} is a scale parameter of the Gumbel distribution. The peak values are calculated at a 78th percentile level of non-exceedance, denoted as P. Following this, the peak values, which are given for the time period, t are extrapolated to a 1 hour full-scale time period, symbolized by T (Gavanski et al., 2016). The equations for

67

the time extrapolations are

$$\mu_T = \mu_t + \frac{ln(\frac{T}{t})}{\alpha_T} \tag{31}$$

$$\alpha_T = \alpha_t \tag{32}$$

The statistical peak area-averaged pressure coefficients measured at mean velocity are then multiplied by a conversion factor. The product of these variables is the equivalent peak pressure coefficient measured at peak velocity, GCp, as defined by ASCE 7.

4.1.4 Conversion Factor

The conversion factor, C, corrects the wind tunnel peak pressures referenced to mean hourly velocity to the equivalent peak pressures referenced to peak velocity. These resultant values can be compared directly to the ASCE 7 provision (Wang and Kopp, 2021b). Once the peak pressure coefficients, $\check{C}p_{AA}$, are found, they are multiplied by this conversion factor, C, to convert them to the ASCE equivalent pressure, GCp. This is denoted as follows in Eq.(34), where the conversion factor is calculated in Eq.(33), such that

$$C = \frac{1}{(1 + gI_U)^2} \tag{33}$$

$$GCp = \check{C}p_{AA}C \tag{34}$$

In Eq.(33), the peak factor, g, has an assumed value of 3 as it is used to determine the 3 second gust speed. The turbulence intensity, I_U, at mean roof height is as listed in Table 3. The conversion factor is of similar concept to the value denoted as F_{WT} in previous works on the NIST database (St. Pierre, 2002). These values are denoted as GCp_{ASCE}, GCp_{CTA}, GCp_{IF} for the three models implemented, the latter two acknowledging clips. The GCp values of each method will be compared to determine a load adjustment factor.

4.2 Validation with Kopp and Morrison (2018)

It is common to validate results to demonstrate that the processing is done correctly and that the results are within a reasonable tolerance, ultimately proving the credibility of the work. In this case, the process used in the present study was validated with the results of Kopp and Morrison (2018). Kopp and Morrison (2018) used the NIST database to propose new zoning definitions that were implemented in ASCE 7-16. These zoning definitions were presented as worst-case enveloped pressure coefficients plots. These plots were reproduced in the present study with the same data sets to ensure the data was being processed correctly.

Test records from the NIST database were downloaded from the public website and tests from three models in open terrain were selected. Any necessary testing parameters and details were taken from Ho et al. (2005), St. Pierre et al. (2005), or the accompanying reports on the NIST website. The tests considered are labelled as jo1, jp1, and sg1. The pressure coefficients were calculated using the same method outlined in Kopp and Morrison (2018). The plots in Figure 41 present the reproduced values from the present study overlaid on the original plots. In this comparison, the ASCE Method was used for the area-averaging of the pressure tap time history. The area-averaged areas were setup as a grid on the building rooftop and they used the windward corner as the datum. The current values were calculated using overlapping area-averages, as was done in the paper. They are presented for the corner (Zone 3), the edge (Zone 2), and the interior (Zone 1).
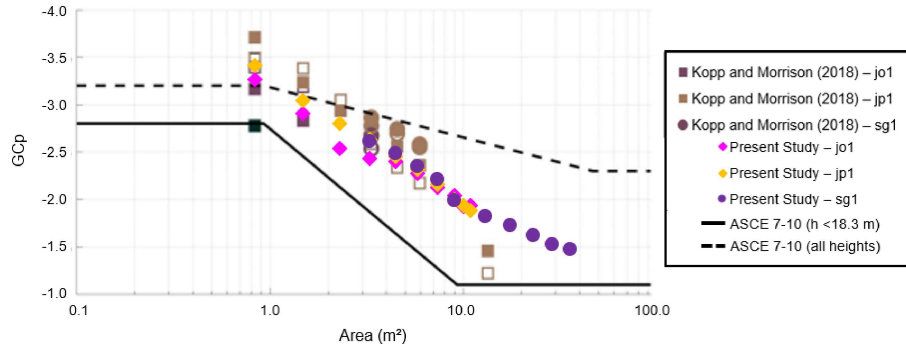
(a)
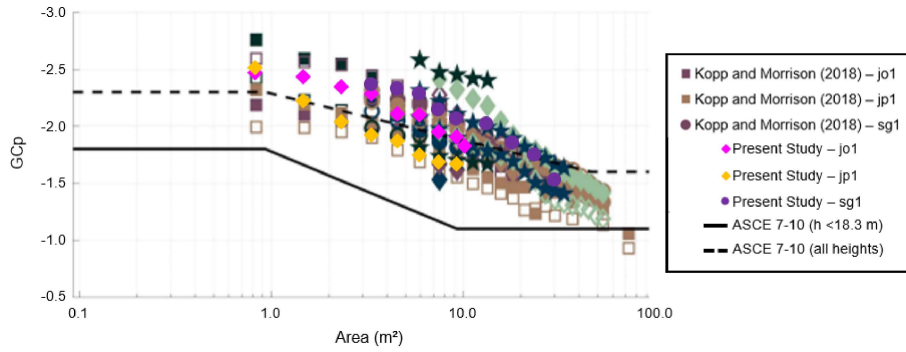
(b)
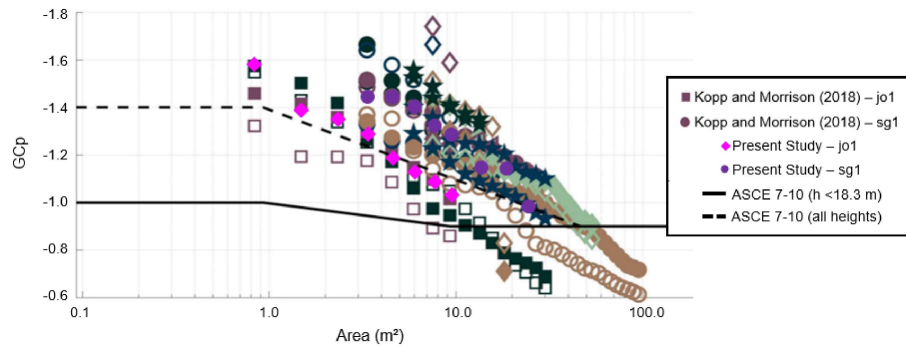
(c)

Figure 41: GCp values at corresponding areas for the ASCE 7-16 zones. The validation with Kopp and Morrison (2018) is overlain for the same tests for (a) Zone 3 (corner), (b) Zone 2 (edge), and (c) Zone 1 (interior).

When compared, the values of the present study are within approximately ±5% of those from Kopp and Morrison (2018). The results have strong agreement with the original paper, thus it can be concluded that the method of calculating the pressure coefficients has

reasonable accuracy. The tests from Arif (2017) were analysed in the same manner as Kopp and Morrison (2018). The results of these tests are discussed in Chapter 5.

4.3   Roof Layout

The ASCE Method does not require an SSMR configuration on the roof. Thus, there are four different building plans used for the ASCE Method. Each building plan was tested at two different heights, for a total of eight models. These building were included as Figure 30 of Chapter 3.

The CTA Method and IF Method both involve an SSMR configurations on the roof. However, there are only two different building plans considered in this analysis for the CTA Method and IF Method. This is because the influence functions developed by Xia (2022) are based on specific plan dimensions and the along seam influence functions cannot be scaled or stretched. The influence functions can only be applied to B1 and B4 buildings, which match the shorter dimensions, B, of the model from Xia (2022).

The standing seam metal roof was based on the model studied in Xia (2022). Their work considered a trapezoidal seam, with a double-lock mechanically seamed connection. The panel thickness was 0.5 mm, which is typical for these roofs (Xia, 2022). The metal panels under consideration in the SSMR model have a width of approximately 0.61 m (2 ft), in some cases there is a panel in the middle of the roof of approximately 0.3 m (1 ft) in width. There were 5 purlins with spacing ranging from 0.85 m spacing to 1.37 m apart. These five purlins were modelled as a 5-span beam using influence functions previously described as the updated analytical model by Xia (2022). Figure 42 shows the schematic of the purlin and clip locations on the roof layout. The ridge of the roof runs parallel to the longest plan dimension of the building. A ridge cap is situated along the ridge of the roof, it is roughly 0.61 m (2 ft) wide.
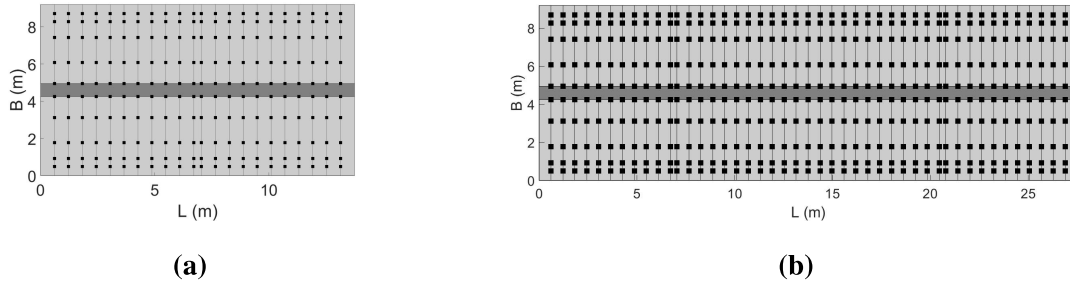
Figure 42: The standing-seam metal roof layout, including panel, clips, and purlins for (a) B1 and (b) B4.

4.4 Modelling Approaches

Low-rise buildings are complicated to model as they are made up of several different construction materials with significant variability, leading to systems that have unknown load paths (Kopp et al., 2012). The CTA Method provides the simplest way to predict clip loads of an SSMR, but it neglects load sharing and failure mechanisms under realistic boundary conditions. The Influence Function Method offers a way to reduce this uncertainty as it accounts for the connection between the load pattern and response, and thus a better idea of spatial variation (Surry et al., 2007). Both methods are based on Eq.(35) for a clip, which is shown as

$$F_{\mathrm{U}} = \int_A P(x,y,t)I(x,y)dA = \frac{1}{2}\rho\bar{U}_{\mathrm{H}}^2 Cp \int_A I(x,y)dA \qquad (35)$$

However, the Influence Function Method is much more involved than the Clip Tributary Area Method. Where necessary, a comparison of the pressure coefficients between the ASCE Method, CTA Method, and IF Method produces a load adjustment factor which demonstrates the differences of the approaches.

4.4.1 Clip Tributary Area Method

The Clip Tributary Area Method was discussed briefly in Chapter 1. Many designers use this simple approach when modelling clip loads (Morrison and Kopp, 2010). It assumes an influence function of one in the geometric tributary area of the clip and zero everywhere

else. The geometric tributary area of a clip is half of the distance to the adjacent fastener or clip, as can be seen in Figure 43.
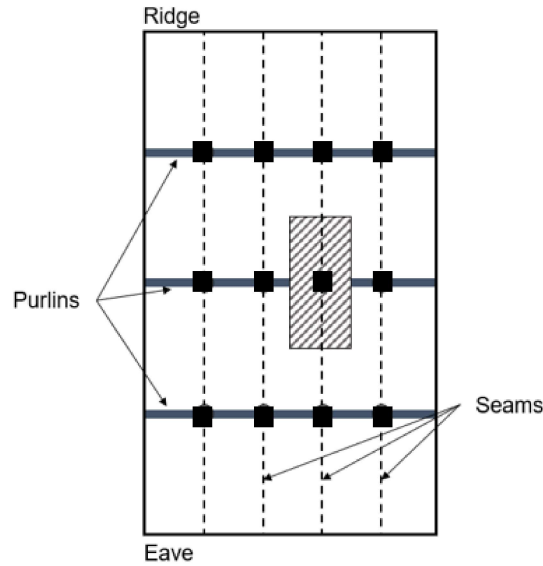
Figure 43: Diagram of the geometric tributary area (hatched fill) of a single clip (black square).

The area, A, from Eq.(35) is the area where the influence function is not equal to zero ($I(x, y) \neq 0$) for the given component. In this method, the area is equal to the clip geometric tributary area, A_{g}. Thus, the effective tributary area, A_{e}, is equal to the geometric tributary area,

$$A_{\mathrm{e}} = \int_{A_{\mathrm{g}}} I(x, y)dA = A_{\mathrm{g}} \tag{36}$$

Eq.(35) becomes,

$$F_{\mathrm{U\,CTA}} = \frac{1}{2}\rho\bar{U}_{\mathrm{H}}^{2}Cp_{\mathrm{CTA}}A_{\mathrm{g}} \tag{37}$$

The uplift force, $F_{\mathrm{U\,CTA}}$, is the clip force over the geometric tributary area of the clip. To make the force non-dimensional, it is normalized by the geometric tributary area and the dynamic pressure, $\frac{1}{2}\rho\bar{U}_{\mathrm{H}}^{2}$, as follows,

$$Cp_{\mathrm{CTA}} = \frac{F_{\mathrm{U\,CTA}}}{\frac{1}{2}\rho\bar{U}_{\mathrm{H}}^{2}A_{\mathrm{g}}} \tag{38}$$

73

The clip pressure coefficient, Cp_{CTA}, is found by area-averaging the pressure time histories of the taps within the clip geometric tributary area. This was previously discussed in Section 4.1.2. Once the clip pressure coefficient is determined, the peak pressure coefficient GCp_{CTA} is calculated.

The CTA Method is the standard approach for both statically-determinate and statically-indeterminate systems. However, the geometric tributary area of the CTA Method is not often equal to the effective tributary area, A_e, for a statically-indeterminate system, such as a SSMR. The clip loads predicted using the CTA Method will be different than the clips loads predicted with the IF Method. The method is easily applied in design modelling, but it may not provide the best estimation of clip loads because it ignores load sharing and boundary conditions of the roof. In the current study, SSMR systems are evaluated by the CTA Method and the IF Method. The results determine how to handle SSMR systems in a building code.

4.4.2 Influence Function Method

The influence function approach can assess SSMR systems in a manner that is more representative of actual wind loads compared to the CTA Method. SSMR systems are statically-indeterminate, meaning they experience load paths that change with uplift force. For instance, first the loads act on the panels, which then transfers it to the fastener or clip, and on to the purlins and MWFRS. These load paths in the roof system are complex, redundant, and do not account for the load redistribution from deformed panels (Morrison and Reinhold, 2015). This deformation cannot be considered within equilibrium calculations, instead it requires influence functions. The influence functions used in the present study were developed by Xia (2022).

Initially, Nasiri (2019) proposed an analytical model for SSMRs by assessing them as multi-span beams. Through observation, they determined the area of the adjacent panels along the seam, for the length of the seam could be considered the influence surface. This is depicted in Figure 44.
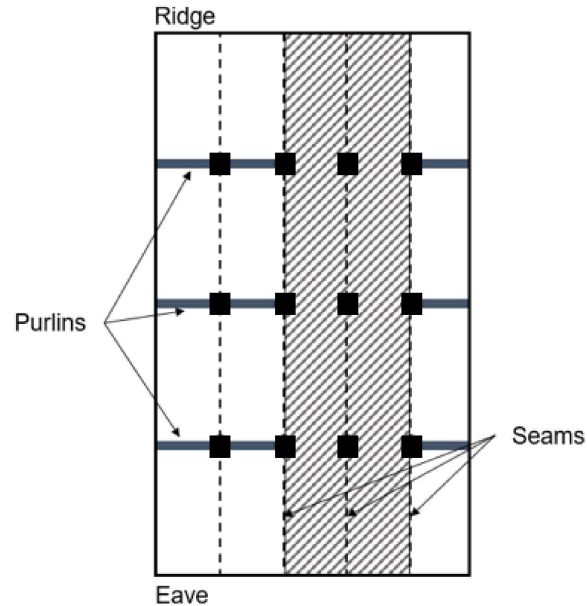
Figure 44: Diagram of the influence surface (hatched fill) of a single clip (black square).

Nasiri (2019) determined the loads are not transferred across the ridge; thus, the roof C&C system can be assessed as two separate systems. They also found that using vertical springs provided more realistic results, and recommended that all clips be modelled as springs in future work. Following this, Xia (2022) applied full-scale testing and finite element modelling to determine the influence functions of all clip of a SSMR. Xia (2022) modelled all clips as vertical springs. They updated the original analytical model and presented revised influence functions, using the same influence surface as Nasiri (2019).

In the present study, there are five clip types, as outlined in Figure 45. Although all the clips are physically identical and installed in the same manner, they are each designated as a specific clip type based on their location along the seam line. The clips in this study are assumed to be fixed clips without stand-off, as this was used in Nasiri (2019). The updated analytical model influence functions from Xia (2022) were used for the along seam influence function in the current study. These influence functions were based on 0 kPa. The along seam influence functions for all clip types are shown in Figures 46 through 50.

75
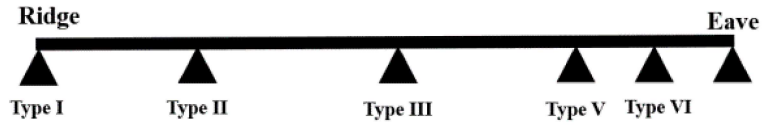
Figure 45: Diagram showing 5-span beam denoting the different clip types along the seam of a SSMR panel (Xia, 2022).
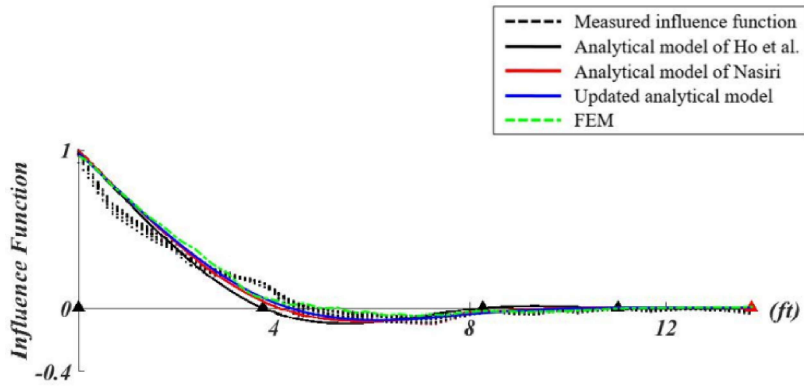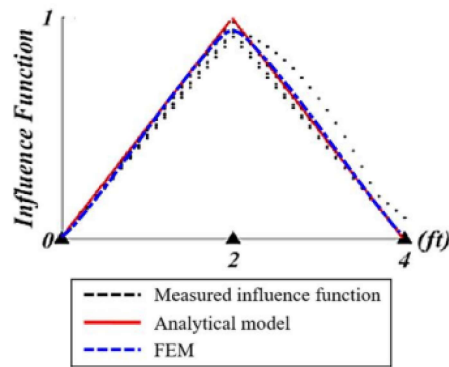

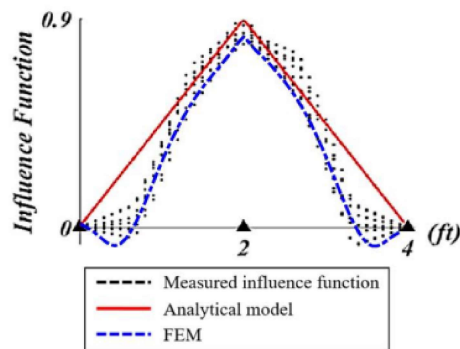**Figure 46: Along seam influence function for type I clip (Xia, 2022).**
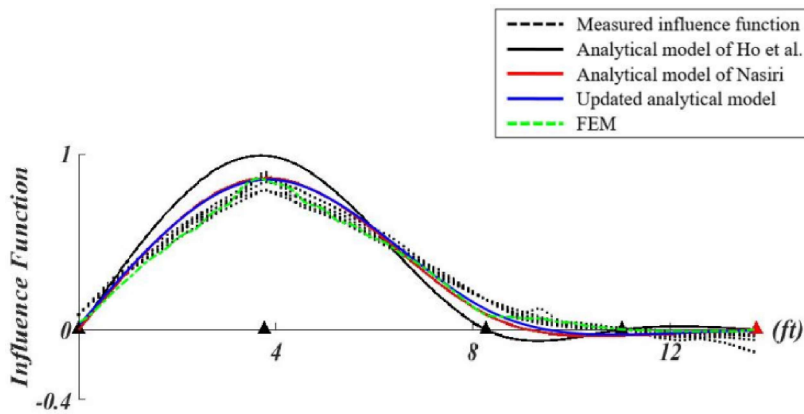
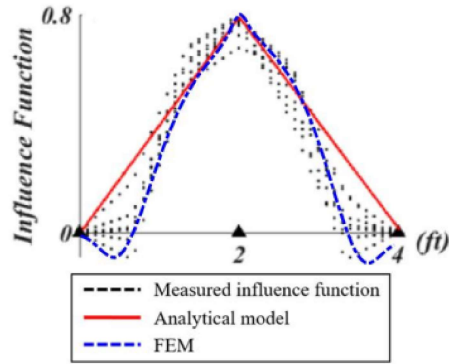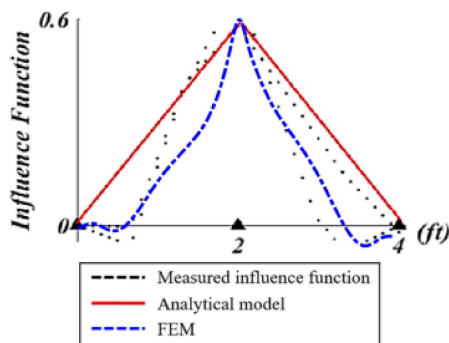**Figure 47: Along seam influence function for type II clip (Xia, 2022).**

76
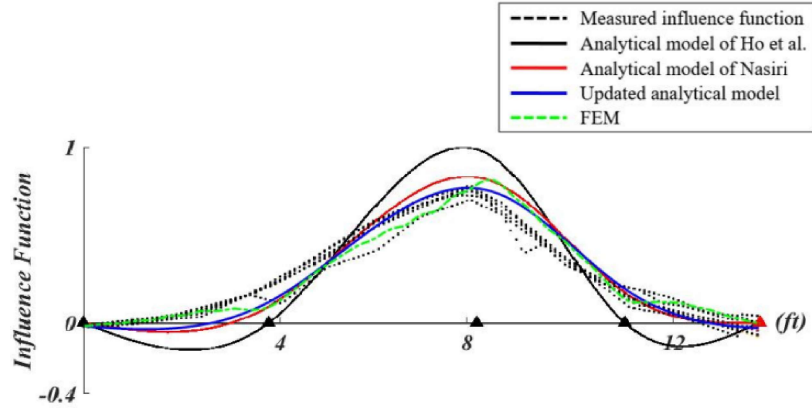
Figure 48: Along seam influence function for type III clip (Xia, 2022).
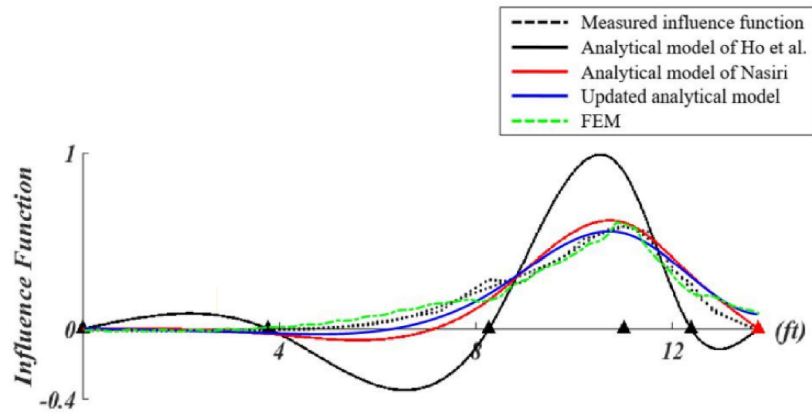
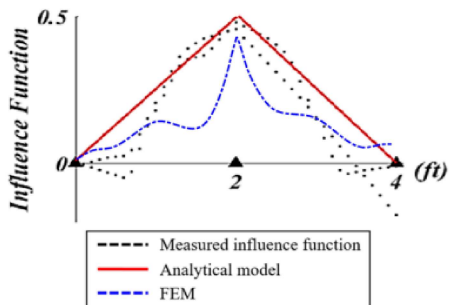**Figure 49: Along seam influence function for type V clip (Xia, 2022).**
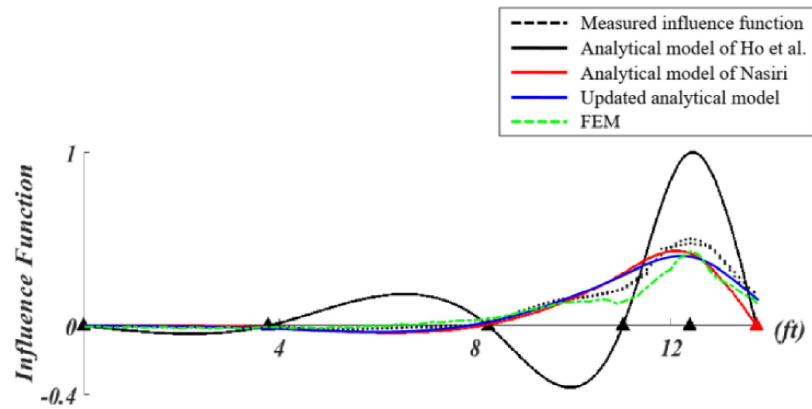
Figure 50: Along seam influence function for type VI clip (Xia, 2022).

The largest influence coefficient for a given clip is at the clip location. However, the maximum influence coefficient is always less than 1 because the clips perform as vertical springs

rather than simple supports (Xia, 2022). Furthermore, Xia (2022) found that clips are affected by the eave boundary condition and that the eave clips have a maximum influence function of approximately 0.5, while the remaining portion of the load transfers to the eave fastener.

The across seam influence function was equal to the along seam influence coefficient on the seam, and then decrease linearly to zero at the adjacent seam (also used in Ho et al., 1995, Farquhar et al., 2005, Xia, 2022). The across seam influence functions for all clip types are shown in Figures 51 through 55 for 0 kPa.

Figure 51: Across seam influence function for type I clip (Xia, 2022).

Figure 52: Across seam influence function for type II clip (Xia, 2022).

Figure 53: Across seam influence function for type III clip (Xia, 2022).

Figure 54: Across seam influence function for type V clip (Xia, 2022).

Figure 55: Across seam influence function for type VI clip (Xia, 2022).

Xia (2022) found that clip stiffness is ambiguous and effects the resultant influence functions. Component tests may underestimate clip stiffness since clips are tested individually. Thus, stiffness may be higher in reality since roof components work together to endure wind loads. With that in mind, the clip stiffness for internal clips was set to 2554 N/mm (Farquhar et al., 2005; Sinno, 2008). Ridge and eave clip stiffness were much greater at

7916 N/mm and 5072 N/mm, respectively. With this, they concluded it is reasonable to consider the ridge clip as a simple support, but the eave support should be considered as a vertical spring.

The influence functions determined by Xia (2022) are based on 0 kPa. They found that between 0 kPa and 0.5 kPa, the load level had little impact on the along seam influence functions, this trend remained until the pressure was over 1 kPa. However, a load between 0 kPa and 0.5 kPa has a significant effect on the across seam influence function due to the stiffness of the panel in this direction. The details of this are not included here for brevity, but can be found in chapter 7 of Xia (2022). This non-linear behaviour makes these systems complex to model using the computational method in this work.

In both the CTA Method and IF Method, the effective tributary area is found by integrating the influence function of an clip over the area where the influence function is non-zero ($I(x, y) \neq 0$). However, in the Influence Function Method, the area where a clip influence function is not equal to zero is the influence surface, A_{IF}. The influence surface spans the length of the panel by the distance to the adjacent seams, as shown in Figure 44. This is expressed mathematically as,

$$A_{\text{e}} = \int_{A_{\text{IF}}} I(x, y) dA \tag{39}$$

where $I(x, y)$ is the blue, updated analytical model shown in Figures 46–50 based on the clip type. Cp_{i} is found by area-averaging the pressure time histories of the taps within the clip influence surface. The tap number is denoted as i for a total number of n taps contributing to the area-average. This was previously discussed in Section 4.1.2, but is shown as

$$F_{\text{U IF}} = \frac{1}{2} \rho \bar{U}_{\text{H}}^{2} \sum_{i=1}^{n} Cp_{\text{i}} I_{\text{i}}(x, y) A_{\text{i}} \tag{40}$$

To obtain the non-dimensional force, Cp_{IF}, the uplift force is normalized by the dynamic pressure, $\frac{1}{2} \rho \bar{U}_{\text{H}}^{2}$, and by the geometric tributary area, A_{g}. This normalization allows for the direct comparison between the Clip Tributary Area Method (Cp_{CTA}) and the Influence

Function Method (Cp_{IF}). This is expressed mathematically as,

$$Cp_{IF} = \frac{F_{U\,IF}}{\frac{1}{2}\rho \bar{U_H}^2 A_g} \qquad (41)$$

Following this, the peak pressure coefficient GCp_{IF} is determined using the process previously discussed.

Although the influence surface is much greater than the geometric tributary area, the effective tributary area calculated from the Influence Function Method is not necessarily greater than that of the Clip Tributary Area Method. Nor is the clip loading the same between methods. Using the code-prescribed geometric tributary area in place of the influence surface may be conservative for statically-indeterminate SSMR systems.

The Influence Function Method has limitations. In low-rise buildings there are many non-structural features that contribute to its strength, these effects cannot be captured by influence functions. Furthermore, the influence coefficient depends on the level of load being applied and the characteristics of the clips (Kopp et al., 2010; Xia, 2022).

4.5   Load Adjustment Factor

Unlike the ASCE Method and the Clip Tributary Area Method, the Influence Function Method considers load sharing among structural components which can set more realistic code values specific to SSMRs. The purpose of this research is not to establish influence functions for every single building component, but to propose a load adjustment factor that can estimate representative wind loads. This factor, F takes the form of

$$F = \frac{GCp_{IF}}{GCp_{ASCE}} \qquad (42)$$

The factor directly compares the ASCE Method and the Influence Function Method, clearly demonstrating the quantitative difference between the code approach and a model that considers realistic load transfer pathways. A value close to 1 indicates the ASCE Method holds

reasonable agreement with the IF Method. As the factor decreases, the ASCE Method values stray from those of the IF Method. This factor is an example of a tool that could help establish SSMR-specific standards using the design standards that currently exist. The results of these analyses are presented in Chapter 5.

5   Results and Discussion

This chapter explores the results of the analyses performed. As mentioned previously, there were three different approaches that were used in the present study: (i) ASCE Method, (ii) Clip Tributary Area Method, and (iii) Influence Function Method.

First, the ASCE Method results are presented in terms of the ASCE zoning. This approach does not involve an SSMR roof configuration. It only considers typical area-averaging to determine worst case enveloped loads. This analysis includes all building models described in the above chapters.

The clip reactions for the Clip Tributary Area Method and Influence Function Method are introduced and compared. The clip loading is plotted for each clip type as this demonstrates the effect of influence functions on wind loads. The wind loading along the roof also proves insight as it confirms conclusions from previous research. These analyses include four building models due to the constraints of the along seam influence function.

The results of all three methods are compared in terms of ASCE zones. The data display the differences among the methods. Following this, the ASCE Method is compared to the IF Method via linear regression. The load adjustment factor is determined. The maximum load adjustment factor for each clip type is presented. The load adjustment factor is examined with respect to the ASCE provision on a zoned-basis. A new iteration of the ASCE Method is proposed, which include a disclaimer for ridge and eave clips.

5.1   ASCE Method

The first method employed was the ASCE 7 approach to finding the peak pressure coefficient. This method closely follows the process utilized in Kopp and Morrison (2018). It differed slightly, since it involved a greater number of segments in the Lieblein BLUE analysis, and calculated the conversion factor to get the peak winds (as described in Chapter 4). Results for all eight building models are presented.

ASCE 7 divides the roof into several different zones based on the building height. Each zone is assigned a pressure coefficient as a function of area. An example of these design standard values were previously shown in Figure 12 of Chapter 1. The zones of each building tested in the current study are included as Figure 56 for H1 and Figure 57 for H2. Note that not all buildings have interior zones due to their plan dimensions and height.
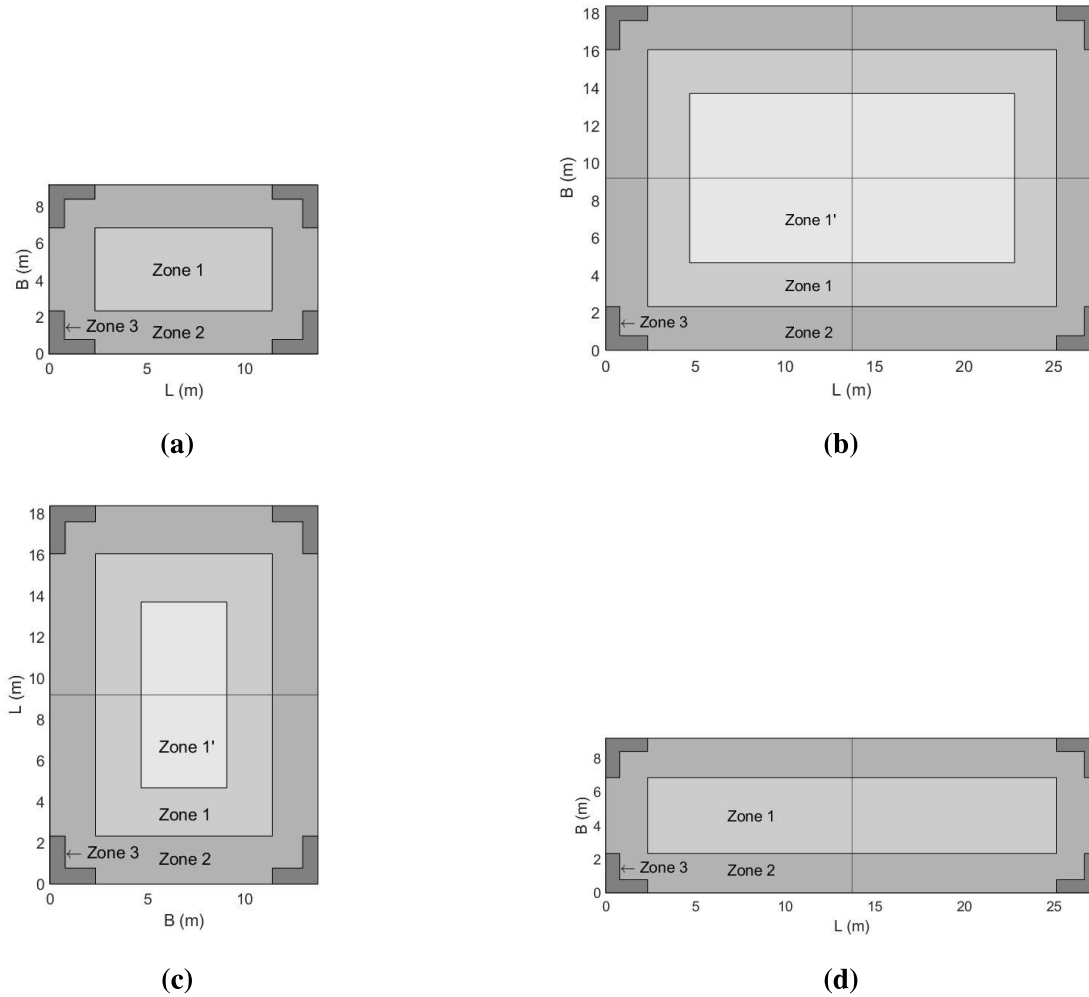
Figure 56: ASCE zones for the corner, edge, and interior areas of the models in the current study, listed as follows (a) B1-H1, (b) B2-H1, (c) B3-H1, and (d) B4-H1.
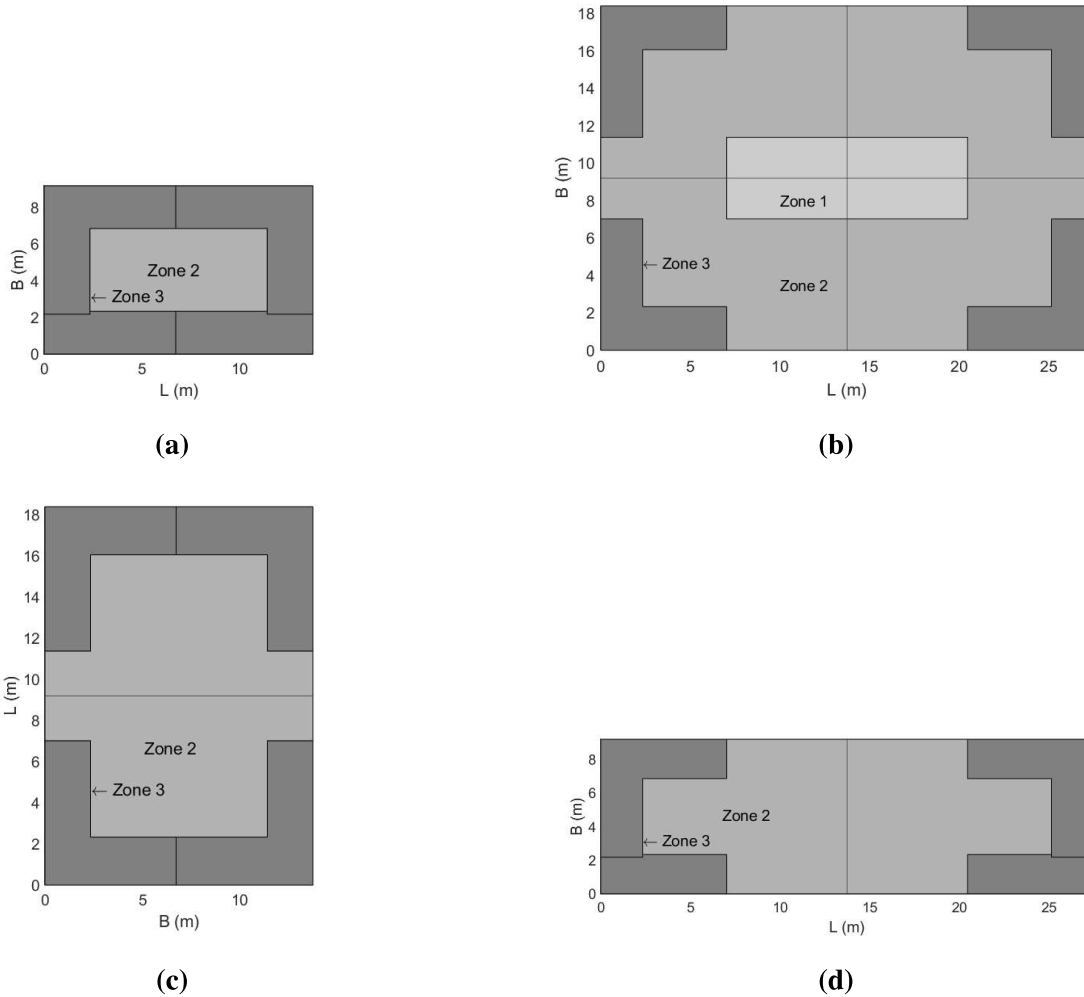
Figure 57: ASCE zones for the corner, edge, and interior areas of the models in the current study, listed as follows (a) B1-H2, (b) B2-H2, (c) B3-H2, and (d) B4-H2.

The following figures show the peak GCp for various effective wind areas in the applicable zone. The effective wind area is terminology used in ASCE 7, and refers to the size of the area-averaging grid. This value was measured over a range of wind directions as listed in Table 2 in Chapter 3. They also include the minimum GCp values as prescribed by ASCE 7.

(**a**)

(**b**)

(**c**)

86
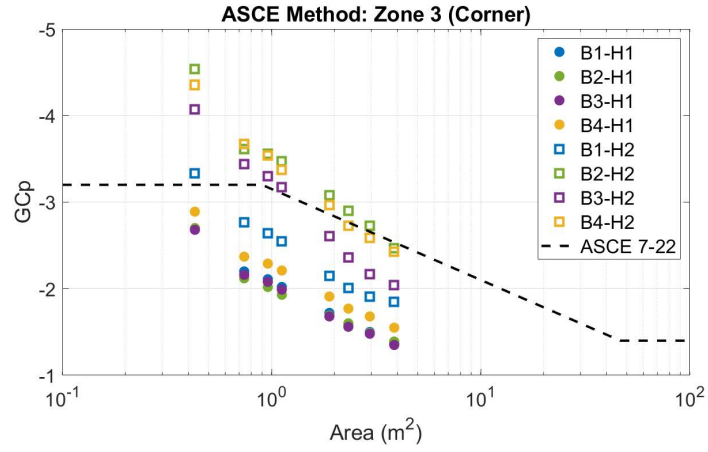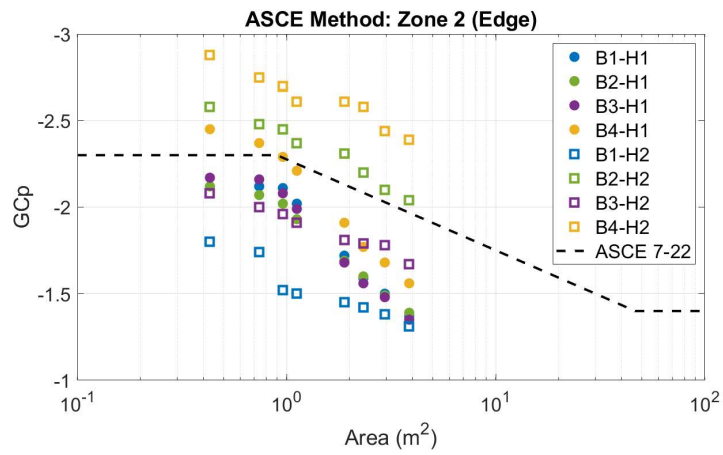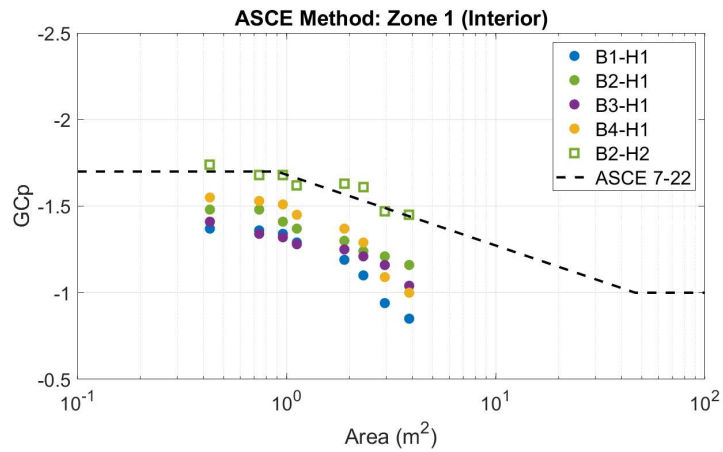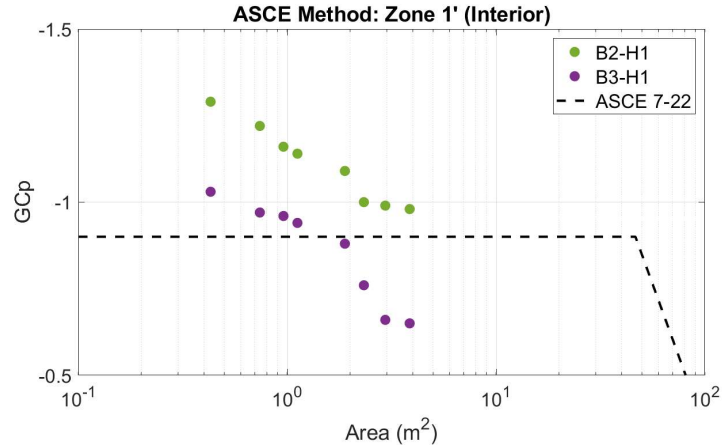
(d)

Figure 58: Worst case enveloped GCp values over all wind directions for all models in current data set presented for (a) Zone 3, (b) Zone 2, and (c) Zone 1, and (d) Zone 1', as defined by ASCE.

As shown in the Kopp and Morrison (2018) validation, as the effective wind area increases the peak pressure monotonically decreases. Surry et al. (2007) illustrated this effect of spatial averaging, shown previously in Figure 19 of Chapter 2. The study demonstrated that increasing spatial-averaging area reduces the peak load over larger areas, which results in a trend of pressure decreases with area.

Overall, the taller models at H2 have larger corner vortices and greater GCp compared to their shorter counterparts. This is typical aerodynamic behaviour for low-rise building roofs when the areas are not normalized by building height (Lin and Surry, 1998; Kopp and Morrison, 2018). This is also why ASCE zone sizing, shown previously in Figure 12 of Chapter 1, is based on the mean roof height. When compared, roof zones 3 and 2 show reasonable agreement to the ASCE provision, because the loading in these areas are driven by flow separations and reattachment. However zone 1' is in a region of reattached flow and this does not hold the same agreement, but require further investigation (Kopp et al., 2022; Doddipatla and Kopp, 2021).

5.2 Comparative Study of Clip Loads based on Clip Type

The comparison between the clip loads and clip type demonstrates the effect of influence functions on clip load predictions. This is done by comparing the results of the Clip Tributary Area (CTA) Method to the Influence Function (IF) Method. Influence functions used in the analysis depend on the individual clip types and their location on the roof.

As mentioned before, only the B1 and B4 models were considered for the CTA Method and IF Method. This is because the influence functions used in this study are based on specific plan dimensions and the along seam influence functions cannot be scaled or stretched to accommodate larger or smaller structures. This section presents results for B1-H1, the remaining figures for B1-H2, B4-H1, and B4-H2 can be found in Appendix A.

The building models B1-H1 and B1-H2 share the same roof clip layout, which is outlined in Figure 59. The clip locations, clip types, and their corresponding geometric tributary area for this roof can be seen in Figure 59. Although the clips are physically identical, the location of a clip on the roof dictates how it transfers loads. The clip type is crucial for determining clip loads with the Influence Function Method. The clip types were previously discussed in Section 4.4.2.
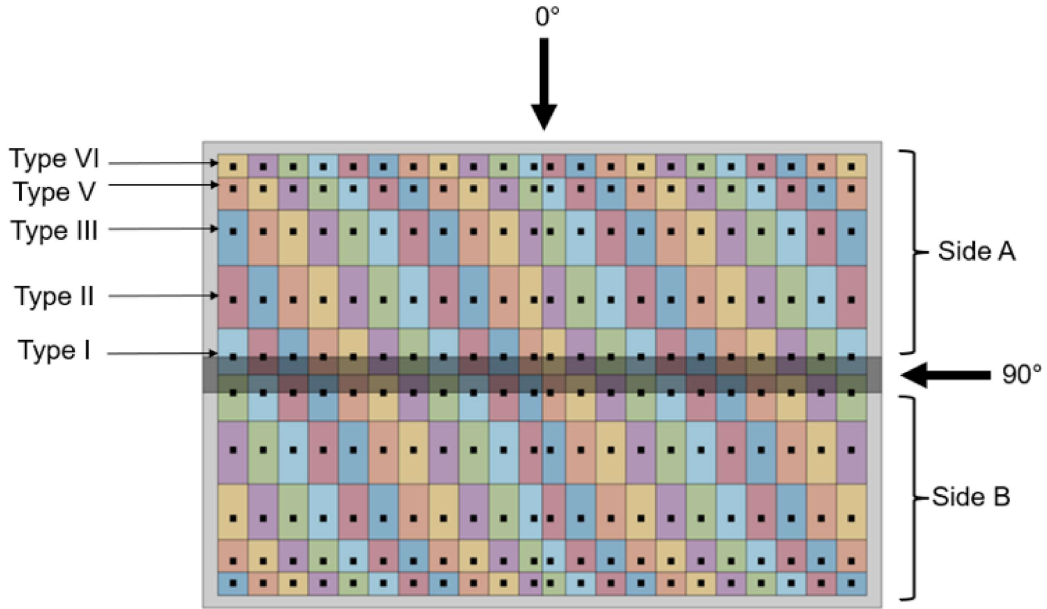
Figure 59: Roof clip layout of B1-H1 and B1-H2, including wind directions and clip types. The shaded boxes correspond to the clip geometric tributary areas.

The clip pressure coefficients were found with both the Clip Tributary Area Method and the Influence Function Method. These values are shown for B1-H1 in Figure 60 for each clip type. The results are plotted for a line of clips parallel to the roof ridge, along length L, which is normalized by the building height, H. The plots each show one clip type, as pictured in Figure 59. These results demonstrate the effect of load sharing on clip reaction predictions.

(a)   (b)
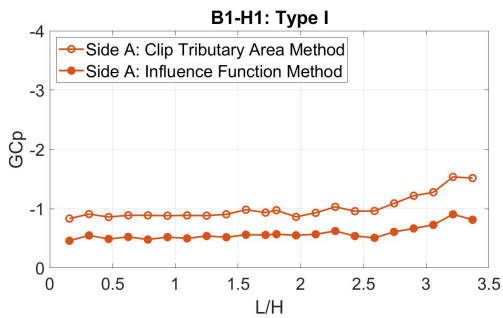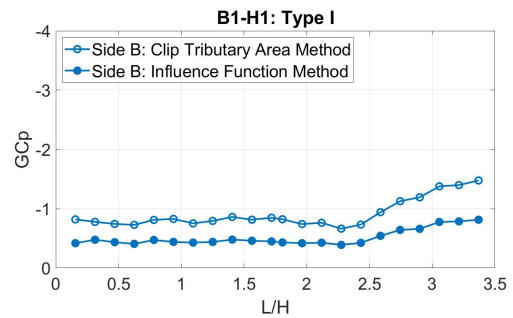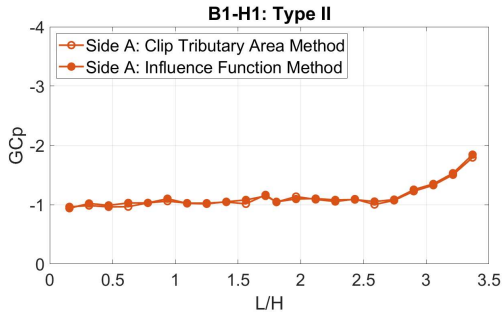
(c)
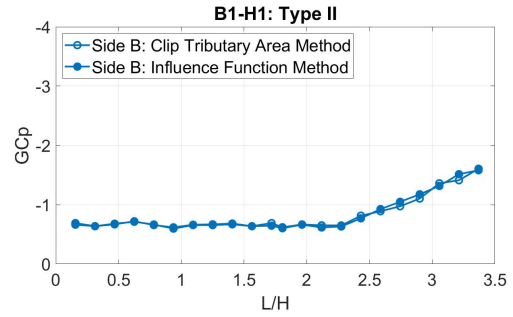
(d)
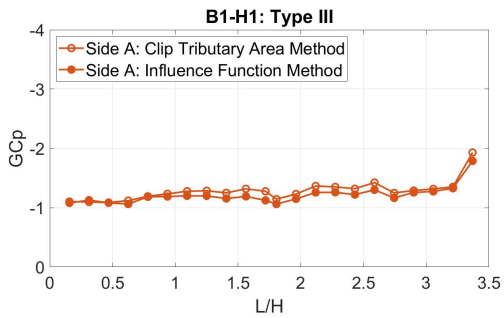
(e)
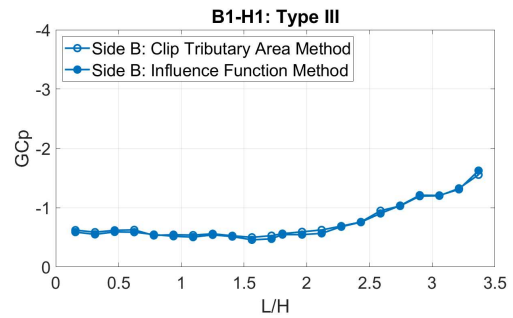
(f)
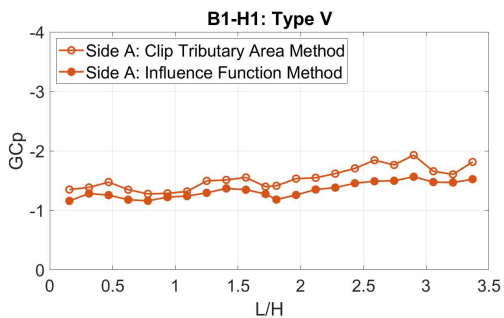
(g)
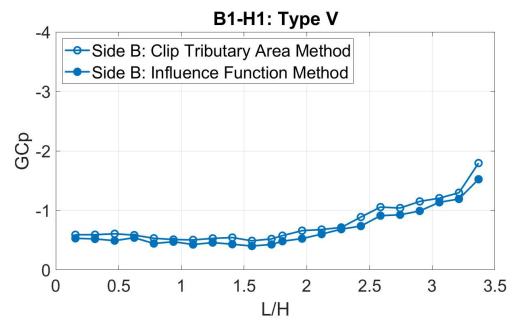
(h)
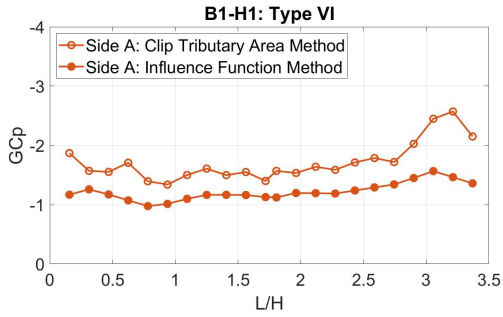
<p style="text-align:center">(i)</p>
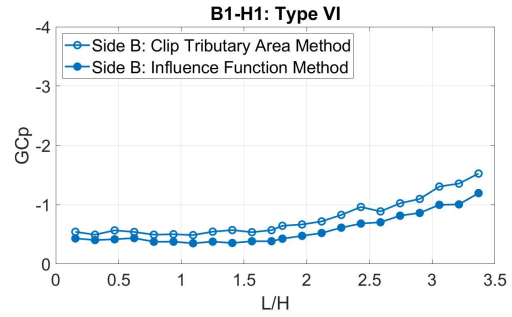
<p style="text-align:center">(j)</p>

Figure 60: GCp values for the Clip Tributary Area Method and the Influence Function Method for B1-H1. Graphs in (a), (c), (e), (g), and (i) display results for clip types I, II, III, V, VI, respectively, for Side A of the building model. Their Side B counterparts are included in (b), (d), (f), (h), and (j).

The results of the B1-H1 models are similar between the CTA Method and IF Method for the internal clips (types II, III, and V). The clip loads from the CTA Method match to the IF Method values within an average of 5% for both Side A and Side B. This indicates that the CTA Method can provide a reasonable estimate of clip loading for inner clips of a SSMR. The same cannot be said for the outer clips at the ridge and eave. Here, influence functions reduce the load most significantly for clips I (ridge) and VI (eave). The average percent difference for each clip of each model is listed in Table 9. The most notable difference is at the windward edge for the type VI clip in Figure 60 (i), where the pressure coefficients from the CTA Method are approximately doubled. This indicates that the IF Method observes the most load sharing at the windward edge in the corner of the roof.

Table 9: Average Percent Difference between CTA Method and IF Method

Model	I	II	III	V	VI
B1-H1	-43%	1%	-4%	-13%	-27%
B1-H2	-43%	3%	-1%	-9%	-27%
B4-H1	-42%	2%	-5%	-13%	-28%
B4-H2	-43%	3%	-5%	-12%	-26%

The magnitude of the ridge clip GCp is 43% lower in the IF Method than the CTA Method. While the eave clip is 27% lower in the IF Method than the CTA Method. These differences can be attributed to these two clip types having boundary conditions which lead to increased load sharing with the edge fasteners.

For the ridge clip, there is a back-up plate at the ridge cap which supports the ridge fastener and restricts deflection. The influence function for the ridge clip is included as Figure 46 of Chapter 4 for reference. For the eave clip, the approximate maximum value of the influence function is 0.5, so a half of the load transfers to the fastener installed at the eave. The influence function for the eave clip is included as Figure 50 of Chapter 4 for reference. There is also load sharing recognized at Side A of a type V clip, this is attributed to the load transfer to the eave support. This load sharing is more significant on Side A than Side B due to the orientation of the windward corner, Side A encapsulates the windward corner.

A roof typically sustains the greatest suction on corner areas and along edges. From these figures it is clear that these are also the areas of an SSMR where load sharing is the greatest. This proves the importance of influence functions for clip reaction forecasting. The CTA Method cannot capture accurate loading at the ridge and eave clips, which leads to overestimated pressure coefficients. However, otherwise, the CTA Method produces values that are, on average, within 5% of the IF Method. These results agree with the conclusions drawn from Xia (2022). The CTA Method is a valid prediction method, but is conservative if used for all clip types. This method requires some refinement for eave and ridge clips to get better estimates of their effective tributary areas for load sharing with edge fasteners. The CTA Method and IF Method are compared to the ASCE Method in the following section.

5.3   Comparative Study of Clip Loads based on ASCE Zones

The results from all three approaches are plotted against effective wind area. Effective wind area of the ASCE Method refers to the area-averaging size. Effective wind area of the CTA

Method and IF Method refers to the clip geometric tributary area. As previously mentioned, only B1 and B4 models were considered for the CTA Method and IF Method and thus only these models are included for the load adjustment factor determination. Figure 61 displays the plots for the corner zone. Figure 62 outlines the comparison between all three approaches for the edge zone. Figure 63 displays the plots for the interior zone.
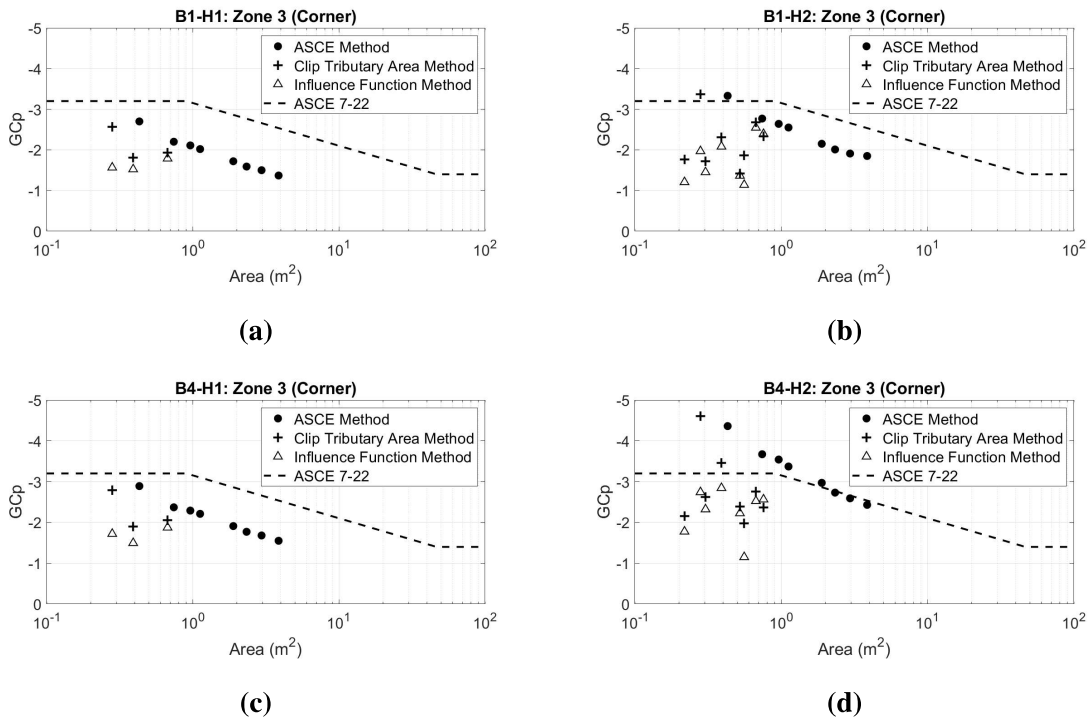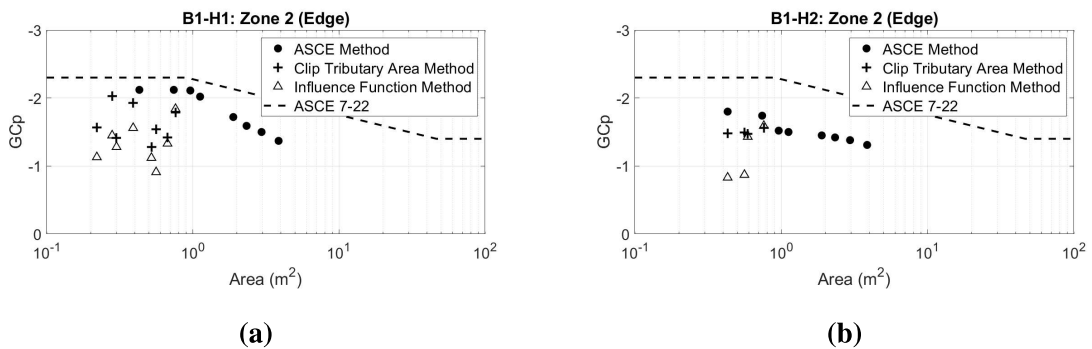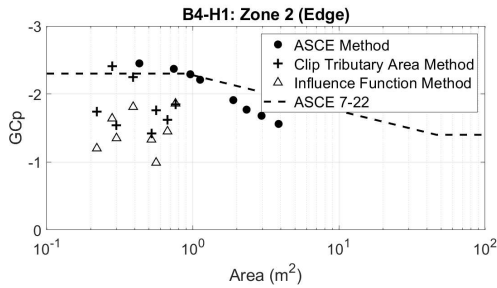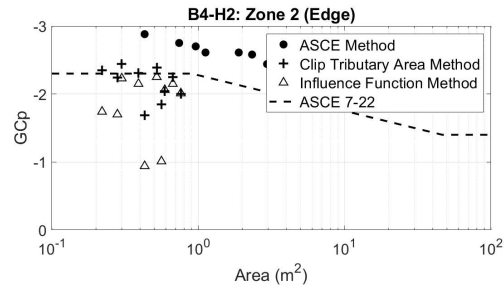

(a)   (b)

(c)   (d)

Figure 61: GCp values between ASCE Method, CTA Method, and IF Method for the corner zone. Plots are listed as (a) B1-H1, (b) B1-H2 (c) B4-H1, and (d) B4-H2.

(a)   (b)

Figure 62: GCp values between ASCE Method, CTA Method, and IF Method for the edge zone. Plots are listed as (a) B1-H1, (b) B1-H2 (c) B4-H1, and (d) B4-H2.
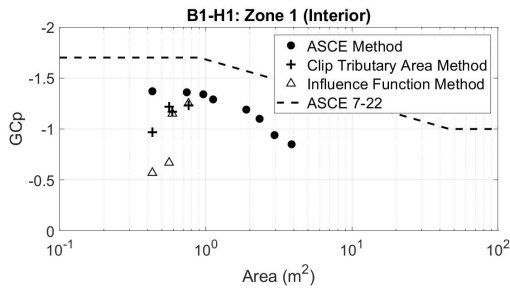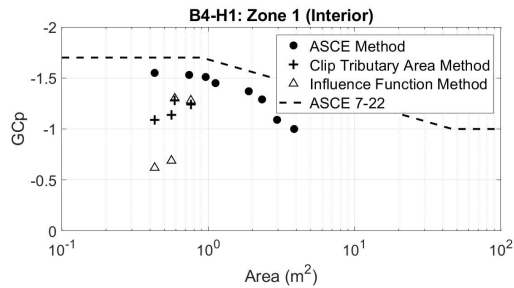
Figure 63: GCp values between ASCE Method, CTA Method, and IF Method for the interior zone. Plots are listed as (a) B1-H1 and (b) B4-H1.

These data demonstrate the nonconformity of the CTA Method and IF Method against the codified ASCE approach, which has a clear trend. The lack of correlation between area and GCp can be considered in regards to the roof layout and clip capacity. The panel spacing is uniform across the roof, but the purlins are spaced closer together towards the corners and edges. The corner and edge regions also tend to experience higher loading and the highest spatial pressure gradient. However, the results indicate these regions actually experience reduced loads. This reduction may indicate that the clips have nominally the same capacity.

It is apparent that the CTA Method and IF Method do not depend on area, and to use area to form a conclusion about a load adjustment factor would be somewhat arbitrary. Thus, it becomes difficult to create a provision for the load adjustment factor that is in accordance

94

with the current ASCE provision. A proposition for a load adjustment factor is presented in terms of clip location in the following section.
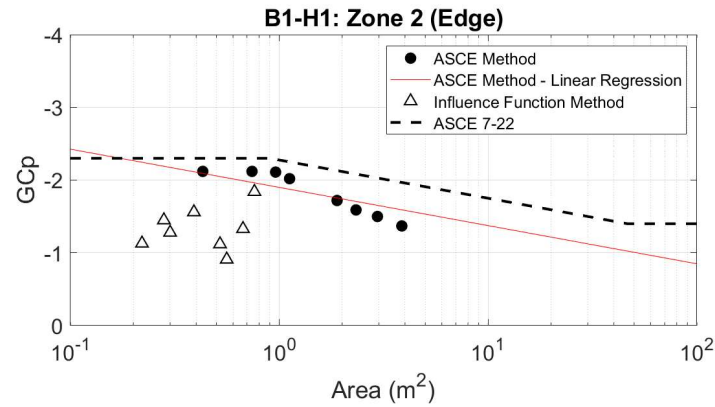
5.4   Load Adjustment Factor

The load adjustment factor expresses the level of similarity between the ASCE Method and the Influence Function Method in terms of pressure coefficient predictions. The load adjustment factor is the quotient of the pressure coefficients from the IF method by the equivalent value of the ASCE Method. Values nearing 1 indicate the ASCE Method is in agreement with the IF Method. As the factor decreases, the ASCE Method becomes more conservative and estimates greater suctions than the IF Method.

The pressure coefficients of the ASCE Method were not necessarily predicted using the same area as the IF Method. Therefore, the equivalent value of GCp_{ASCE} at the area of GCp_{IF} was found by applying a linear regression model to the ASCE Method. The slope of this model was set to that of the ASCE 7 standard. This is depicted in Figure 64 for B1-H1. The figures for the remaining buildings are included in Appendix A.
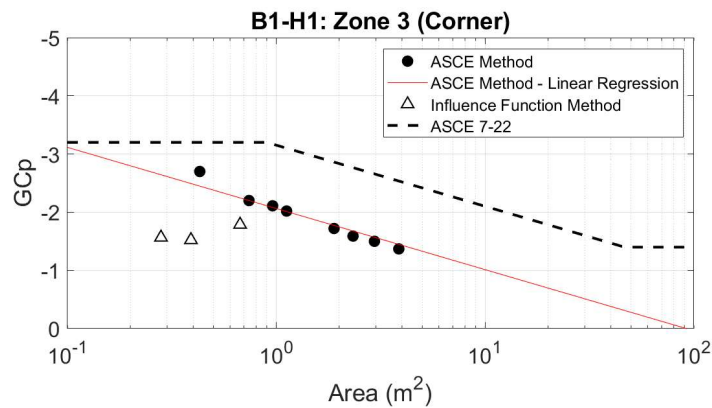
(a)

(b)
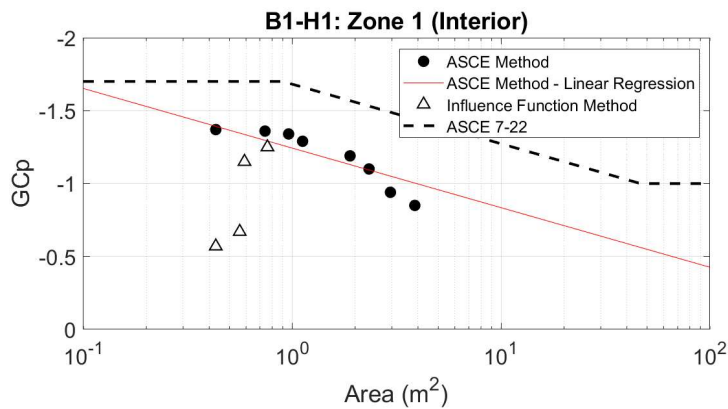
(c)

Figure 64: Linear regression of the ASCE Method of B1-H1 for (a) zone 3 (b) zone 2, and (c) zone 1.

The load adjustment factor was calculated for B1-H1 using the interpolated values from Figure 64 and the worst case enveloped pressure coefficients from the IF Method. An example of this is shown in Table 10. There is no noticeable trend of load adjustment factor with area, likely because the load adjustment factor tends to rely more on the aforementioned clip layout and position. The influence coefficients are lowest at the ridge clips (type I) and eave clips (type VI), which implies that the GCp_{IF} will be smaller than GCp_{ASCE} due to greater load sharing, leading to decreased F values.

Table 10: Load Adjustment Factors for B1-H1

Zone	Area (m²)	Clip Type	GCp_{ASCE}	GCp_{IF}	F
3	0.28	VI	-2.64	-1.57	0.59
	0.39	V	-2.49	-1.52	0.61
	0.67	III	-2.25	-1.79	0.80
2	0.22	VI	-2.25	-1.13	0.50
	0.28	VI	-2.19	-1.45	0.66
	0.30	V	-2.17	-1.28	0.59
	0.39	V	-2.11	-1.56	0.74
	0.52	III	-2.05	-1.12	0.55
	0.56	I	-2.03	-0.91	0.45
	0.67	III	-1.99	-1.33	0.67
	0.76	II	-1.96	-1.84	0.94
1	0.43	I	-1.39	-0.57	0.41
	0.56	I	-1.35	-0.67	0.50
	0.59	II	-1.34	-1.15	0.86
	0.76	II	-1.29	-1.25	0.97

The maximum load adjustment factor was taken at each clip position along the shorter plan dimension, B. This was done for all zones. Both eave edges are used as a datum to describe the clip position as a distance from the ridge. The maximum value was selected as this provides conservatism in the results. The side-by-side comparison of the load adjustment factor against area and against clip position can be seen in Figure 65.
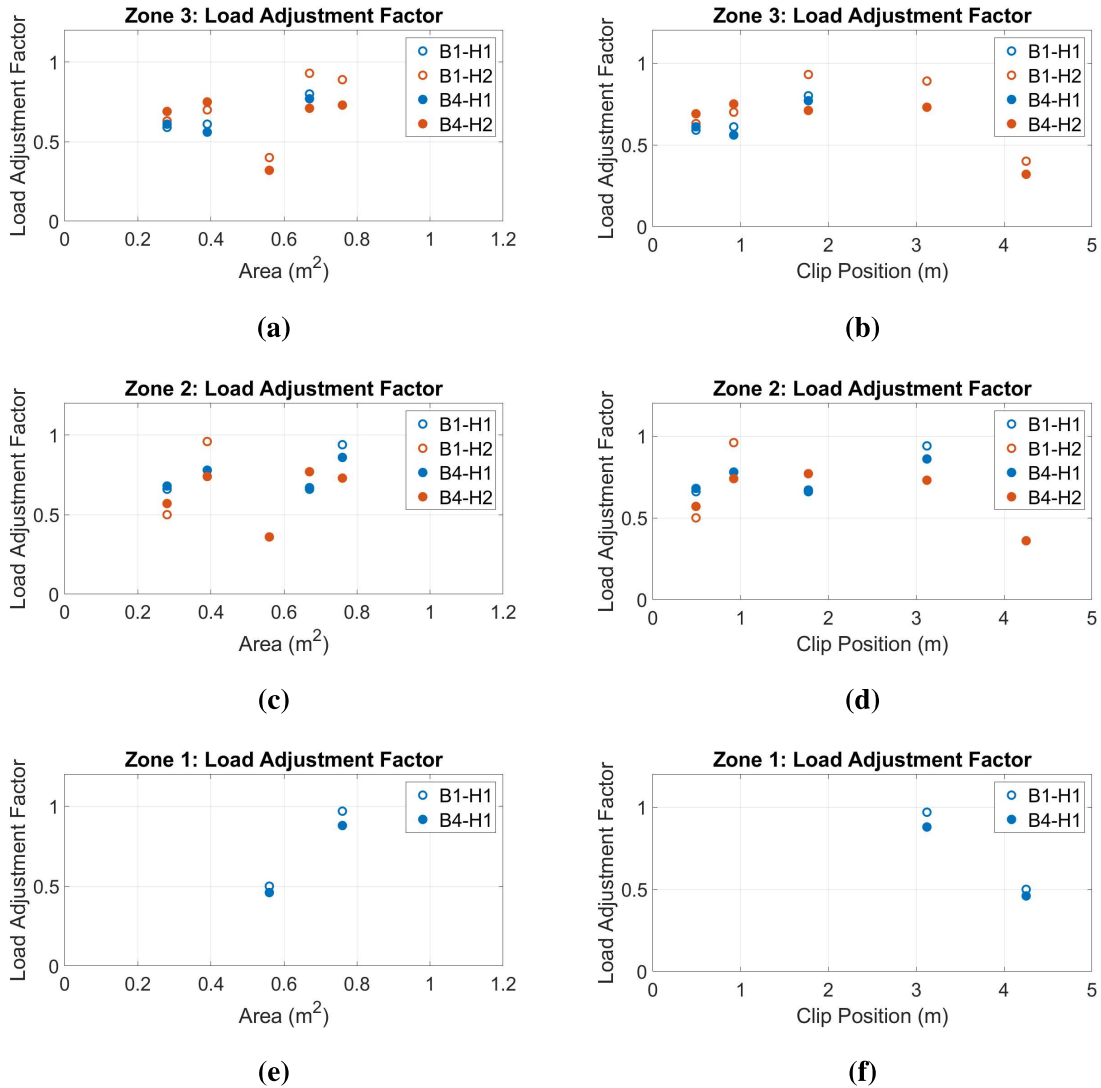
Figure 65: Maximum load adjustment factor for all buildings as shown in (a) and (b) for zone 3, (c) and (d) for zone 2, and (e) and (f) for zone 1.

Figures 65 (b), (d), and (f) show the maximum factor along the seam, with 0 m as the eave and 4.25 m as the ridge clip. Although there is no pronounced trend with clip position, the load adjustment factor tends to arc across the span of the seam, with higher load adjustment factors observed at the inner clips, and the lowest values at the ridge and eave clips. This implies that the ASCE Method, while more conservative than the IF Method, has closer approximation to the actual loads for internal clips than those at the ridge and eave.

Since there is no feasible trend with area, the load adjustment factor is generalized based on zone and clip location. The ASCE Method provides an approximation of the pressure distribution, with an average load adjustment factor for the inner clips of 0.74 in zone 3, 0.78 in zone 2, and 0.92 in zone 1. In other words, all clips regardless of their tributary area can use the average F from Table 11. These values indicate the ASCE Method is on average 26%, 22%, and 8% conservative for clips in ASCE zones 3, 2, and 1, respectively. However, this load adjustment factor will be conservative (*i.e.*, safe) for ridge and eave clips. The factor is defined more specifically for ridge and eave clips below.

Table 11: Load Adjustment Factors for Inner Clips

Zone	F
3	0.74
2	0.78
1	0.92

As mentioned, a roof incurs the highest suction at its corners and edges and these areas coincide with the clips that possess the greatest load sharing, and therefore actually limit the effect of the suction. The load adjustment factor depends on clip location. Therefore, the load adjustment factor should not only be defined for inner clips based on zone as in Table 11, but for ridge and eave clips as well, regardless of zone. Defining the clip locations of the ridge and eave clips is important; In this case, it is as simple as designating the ridge clip as the clip that secures the ridge cap to the panel or to the back-up plate and designating the eave clip as the first clip adjacent to the eave edge. The proposed values are outlined in Table 12 (Note that only 1 of Table 11 or Table 12 can be used). These values indicate the ASCE Method is, on average, 59% and 38% conservative for ridge and eave clips, respectively.

Table 12: Load Adjustment Factors for Ridge and Eave Clips

Clip	F
Adjacent to or at Ridge	0.41
Adjacent to Eave	0.62

The designer or modeller whom is utilizing the code should have an approximation of the roof clip layout, and thus using this guideline for ridge and eave clips should not be ambiguous. These tables used in combination would provide a realistic estimation of the clip loads for SSMRs.

5.5   Summary

The ASCE Method was developed to predict wind loads by employing building aerodynamic principles. It was not purposed to estimate wind loads on the SSMR structure simply because it does not account for the effects of load sharing among components. The Influence Function Method, on the other hand, can calculate more representative pressure distributions for the standing seam metal roof.

The ASCE Method results were presented in terms of the ASCE zones. The results match those of Kopp and Morrison (2018) validation of Chapter 4: As the area averaging size increases the peak pressure is reduced. As is typical aerodynamic behaviour, the taller buildings experience greater roof uplift compared to their shorter counterparts.

The clip reactions for the Clip Tributary Area Method and Influence Function Method were compared and demonstrated the effect of influence functions on clip reactions. The CTA Method was quite conservative for ridge and eave clips, but otherwise it produced values that are within 5% of the IF Method.

The results of all three methods are compared in terms of ASCE zones. There is no trend with area for the CTA Method and IF Method, as there is for the ASCE Method. However, the ASCE Method is generally conservative in clip reaction predictions. The ASCE

Method was then compared to the IF Method via linear regression in order to produce a load adjustment factor. The proposed factor was presented for each ASCE zone for inner clips and ridge and eave clips separately.

6 Conclusions and Recommendations

High winds cause extreme pressure fluctuations on low-rise buildings and the C&C take the bulk of these wind loads (Kopp and Morrison, 2018). Building aerodynamics along with wind-induced pressures lead to flow separation and reattachment, a major cause of damage to the roof and the cladding (Saathoff and Melbourne, 1989). Improved wind loading predictions can facilitate code amendments, and promote the reinforced design of components and cladding, like standing seam metal roofs.

Standing seam metal roofs (SSMR) are an economical alternative to conventional roof systems. They consist of prefabricated panels secured to the underlying structural purlins using clips hidden within the standing seam. These clips incur the bulk of the wind loads. They provide a water-tight, corrosion-resistant, thermal-resistant roofing system. Their geometric features are able to break up cornering vortices and therefore reduce wind loads on clips (Azzi et al., 2020). The motivation for this research was to present a code-approach for evaluating standing seam metal roof systems. These systems are more flexible than traditional wood-framed structures, and thus may experience deformation at lower wind loads.

This research used wind tunnel data in combination with analytical clip influence functions to produce SSMR clip reactions. The wind tunnel data involved several building models outfitted with a bare deck flat roof with a high tap resolution that could provide results with higher accuracy that the NIST database (Arif, 2017). The analytical clip influence functions were based on finite-element model of an SSMR configured roof (Xia, 2022). With these data, the wind loading was determined using three approaches: the ASCE Method, Clip Tributary Area Method (CTA Method), and Influence Function Method (IF Method). The equivalent peak pressure coefficients from all methods were compared to produce a load adjustment factor that is described by:

$$F = \frac{GCp_{\text{IF}}}{GCp_{\text{ASCE}}} \tag{43}$$

This work contributes to the recommendations of previous research (Farquhar et al., 2005; Habte et al., 2015; Surry et al., 2007) which suggested the use of aerodynamic databases in combination with finite element modelling (El Damatty et al., 2003; Nasiri, 2019; Xia, 2022) to produce component-specific responses. Using this combination of tools allowed for a direct comparison between wind loads from the code approach (ASCE Method), wind loads from a load sharing approach (IF Method), and wind loads from a hybrid method of both (CTA Method). The comparison was used to produce a load adjustment factor that roughly captures conservatism in the ASCE code. Although an adjustment factor has been mentioned in Sinno (2008), it was not in the same manner of the current work. The current work provides a connection between the ASCE provision and clip loads in effort to obtain more realistic results. Further work is required to confirm and refine the ideas of the current study.

6.1 Conclusions

The ASCE Method produced results that followed expectations of typical building aerodynamics as determined by the Kopp and Morrison (2018) validation. As the effective wind area size increases, the peak pressure monotonically decreases. The taller models displayed greater GCp compared to their shorter counterparts. ASCE roof zone 3 (corner) and zone 2 (edge) follow the design standard in the ASCE provision. Wind loads in these areas are driven by flow separation and reattachment.

A roof on a low-rise building experiences the highest suction at the corners and edges. These areas coincide with the clips that have the greatest load sharing, and thus the peak suction was reduced most significantly in these regions. The comparison of the Clip Tributary Area Method to the Influence Function Method demonstrates the role of influence functions in clip load predictions.

When compared to the Influence Function Method, the Clip Tributary Area Method overestimated the ridge clip (type I) GCp by 43% and the eave clip (type VI) by 27% . For

the eave clip, the approximate maximum value of the influence function is 0.5, therefore a sizeable portion of the load transfers to the fasteners along the eaves. For the ridge clip, there is a back-up plate at the ridge cap, which supports the ridge fastener and restricts deflection (Xia, 2022).

For the interior clips (type II, III, V), the CTA Method produces values that are within 5% of the IF Method. The CTA Method is a valid prediction model since it produces coefficients comparable to the IF Method, but it is conservative if used for all clip types because it does not account for load sharing at the ridge and eave clips.

All three approaches were compared against area. The results of the CTA Method and IF Method did not have any correlation with area, whereas the ASCE Method did. From this, it is apparent that the CTA Method and IF Method do not depend on area. To use area to form a conclusion about a load adjustment factor would be arbitrary. Without a trend based on area, a different solution to codify load adjustment factor was proposed.

It was found that the clip loads depend on the clip layout, and therefore the load adjustment factor should be defined by the clip layout and position as well. The influence functions are smallest at the ridge clips (type I) and eave clips (type VI), which implies that there will be greater load sharing and thus a smaller load adjustment factor. Although there was no strong trend with clip position, the load adjustment factor tends to be the greatest at the inner clips and the lowest at the ridge and eave clips. This indicates that the ASCE Method, however conservative, has closer approximation to the actual loads for internal clips than those at the ridge and eave.

The load adjustment factor was determined fist for inner clips based on ASCE zone. It was then determined for ridge and eave clips separately, regardless of ASCE zone. The ridge clip is defined as the clip that secures the ridge cap to the panel or to the back-up plate. The eave clip is defined as the first clip adjacent to the eave edge.

6.2 Limitations

Wind Tunnel Test Data: Unknown QA/QC between experiments There are limitations to the applicability of the current study, including the validity of the wind tunnel data, the variety of building models, and the functionality of the influence functions from Xia (2022).

First, the wind tunnel experimental data used for the velocity profile (Akon and Kopp, 2016) and for he pressure data (Arif, 2017) were completed years apart. The velocity from Akon and Kopp (2016) is notably lower than in Arif (2017), however the turbulence intensity is lower in Arif (2017) for the shorter model. The mismatch between experiments was deemed likely a result of different physical characteristics (*e.g.*, cleanliness of the screens, upstream of the wind tunnel contraction) in the wind tunnel, since the experiments were not conducted simultaneously. Although the quality control procedures were unknown for both experiments, the data was validated as best as reasonably achievable, but still shows clear discrepancies.

Second, the wind tunnel models tested only tested on buildings of two basic plan shapes with flat roofs. These building models were restricted to those with dimensions similar to Xia (2022). It would be valuable to determine the wind loading in the same fashion as in the current research, but for a roof of a slope greater than 0 degrees. These results could be compared to the results to the same modelled outfitted with a bare deck roof to determine the effect of roof pitch on wind loading.

The third limitation has to do with influence functions. The finite element analysis completed by Xia (2022) produced influence functions for a roof of one particular size and layout. The current clip layout was prescribed by Xia (2022) with clips ranging from 0.85 m to 1.37 m apart along the seam. Clip spacing in practise is typically 1 m (3 ft) apart, but can vary greatly as the exact roof layout is designed by an engineer. The effect of shifting clips along the seam has not been researched in depth to date, but would provide valuable insight into how load distribution changes with the clip layout along the seam.

In addition to the roof layout, only two building models from Arif (2017) were considered for the Clip Tributary Area Method and Influence Function Method. This is because the influence functions used in this study are based on specific plan dimensions of building breadth and the along seam influence functions likely cannot be scaled or stretched to accommodate larger or smaller structures since the clips have finite loading capacity and that capacity does not increase with tributary area. An investigation to determine the impact of scaling influence functions would provide more insight on the applicability of influence functions to different models. It would also be pertinent to determine influence functions for hip roofs, in addition to the current ones employed that area specific to gable roofs.

The influence functions are also limited by the panel properties from the FEM analysis in Xia (2022). The thickness of panel affects its flexibility, which in turn, affects the deflection and therefore the influence function. In this case, the panel was 0.5 mm thick which is a standard thickness for these roofing systems. However, further work would be required to determine the extent of decreasing or increasing panel thickness on the influence functions.

Furthermore, the influence functions used in this analysis are based on 0 kPa loading which is a simplification of the actual panel behaviour. Xia (2022) determined that between 0 kPa and 0.5 kPa, the load level had little impact on the along seam influence functions due to the seam flexibility, this trend continues until the pressure is over 1 kPa. However, a load between 0 kPa and 0.5 kPa has a significant effect on the across seam influence function due to the stiffness of the panel in this direction. This non-linear panel behaviour makes these systems complex to model with the computational method used in this work.

6.3   Recommendations for Future Work

The current work only considered a full analysis of four building models out of the eight possible models. This is because the influence functions in the along-seam direction were based on specific plan dimensions that matched those of B1 and B4. It is hypothesized that the along-seam influence functions cannot be scaled or stretched to accommodate larger

or smaller structures. Further work on influence function scaling would be required to determine their applicability to different plan shapes. It would be useful for future works to develop clip influence functions for simple-shaped buildings of different dimensions. These influence functions could be used to validate the current work and reinforce or denounce the implementation of a generalized load adjustment factor.

Furthermore, all models in this work were outfitted with a flat roof with a gable roof style SSMR. Future studies and experimentation should consider more diverse building models. Models involving roofs of several different slopes would improve the understanding of load adjustment factors and determine the relationship to roof slope. Overall, any future SSMR research should prioritize creating simple guidelines and rules that can be easily codified by bodies that govern building provisions.

References

Akon, A. F. (2017). *Effects of Turbulence on the Separating-Reattaching Flow Above Surface-Mounted, Three-Dimensional Bluff Bodies* (Doctor of Philosophy in Civil and Environmental Engineering). University of Western Ontario.

Akon, A. F., & Kopp, G. A. (2016). Mean Pressure Distributions and Reattachment Lengths for Roof-Separation Bubbles on Low-Rise Buildings. *Journal of Wind Engineering and Industrial Aerodynamics*, *155*, 115–125. https://doi.org/10.1016/j.jweia.2016.05.008

Ali, H. M., & Senseny, P. E. (2003). Models for Standing Seam Roofs. *Journal of Wind Engineering and Industrial Aerodynamics*, *91*, 1689–1702. https://doi.org/10.1016/j.jweia.2003.09.014

Arif, F. (2017). *Influence of Turbulence on the Aerodynamics of Low-Rise Buildings* (Master of Engineering Science in Civil and Environmental Engineering). University of Western Ontario.

ASCE. (2010). *Minimum Design Loads for Buildings and Other Structures: ASCE 7-10*.

ASCE. (2016). *Minimum Design Loads and Associated Criteria for Buildings and Other Structures: ASCE 7-16*.

ASCE. (2022). *Minimum Design Loads and Associated Criteria for Buildings and Other Structures: ASCE 7-22*.

ASTM International. (2001). *Standard Test Method for Structural Performance of Sheet Metal Roof and Siding Systems by Uniform Static Air Pressure Difference: ASTM E1592-05(2001)* (Standard). West Conshohocken, PA, United States. https://doi.org/10.1520/E1592-05R17

Azzi, Z., Habte, F., Vutukuru, K. S., Chowdhury, A. G., & Moravej, M. (2020). Effects of Roof Geometric Details on Aerodynamic Performance of Standing Seam Metal Roofs. *Engineering Structures*, *225*, 1–12. https://doi.org/10.1016/j.engstruct.2020.111303

Baskaran, A., & Dutt, O. (1997). Performance of Roof Fasteners Under Simulated Loading Conditions. *Journal of Wind Engineering and Industrial Aerodynamics*, *72*, 389–400. https://doi.org/10.1016/S0167-6105(97)00256-0

Cook, N. J., Keevil, A. P., & Stobart, R. K. (1988). "BRERWULF —- The Big Bad Wolf. *Journal of Wind Engineering and Industrial Aerodynamics*, *29*, 99–107.

Crandell, J. H., Nowak, M., Laatsch, E. M., van Overeem, A., Barbour, C. E., Dewey, R., & Angleton, H. (1993). *Assessment of Damage to Single-Family Homes Caused by Hurricanes Andrew and Iniki* (Standard). Washington, DC, United States, US Department of Housing; Urban Development.

Davenport, A. G. (1995). How Can We Simplify and Generalize Wind Loads? *Journal of Wind Engineering*, *54/55*, 657–669. https://doi.org/10.1016/0167-6105(94)00079-S

Dixon, C. R., Prevatt, D. O., & Datin, P. L. (2011). Influence of Edge Restraint on Clip Fastener Loads of Standing Seam Metal Roof Panels. *Journal of ASTM International*, *8*, 1–16. https://doi.org/10.1520/JAI103704

Doddipatla, L. S., & Kopp, G. A. (2021). Wind Loads on Roof-Mounted Equipment on Low-Rise Buildings with Low-Slope Roofs. *Journal of Wind Engineering and Industrial Aerodynamics*, *211*, 104552. https://doi.org/10.1016/j.jweia.2021.104552

El Damatty, A. A., Rahman, M., & Ragheb, O. (2003). Component Testing and Finite Element Modeling of Standing Seam Roofs. *Thin-Walled Structures, 41*, 1053–1072. https://doi.org/10.1016/S0263-8231(03)00048-X

ESDU. (1974). *Characteristics of Atmospheric Turbulence Near the Ground: ESDU 74031* (Standard). London, United Kingdom.

ESDU. (2001). *Characteristics of Atmospheric Turbulence Near the Ground: ESDU 85020* (Standard). London, United Kingdom.

Farquhar, S., Kopp, G. A., & Surry, D. (2005). Wind Tunnel and Uniform Pressure Tests of a Standing Seam Metal Roof Model. *Journal of Structural Engineering, 131*, 650–659. https://doi.org/10.1061/(ASCE)0733-9445(2005)131:4(650)

Gavanski, E., Gurley, K. R., & Kopp, G. A. (2016). Uncertainties in the Estimation of Local Peak Pressures on Low-Rise Buildings by Using the Gumbel Distribution Fitting Approach. *Journal of Structural Engineering, 142*, 1–14. https://doi.org/10.1061/(ASCE)ST.1943-541X.0001556

Habte, F., Mooneghi, M. A., Chowdhury, A. G., & Irwin, P. 14th International Conference on Wind Engineering. In: In *Performance of Standing Seam Metal Roofs under Realistic Wind Loading*. 2015.

Henderson, D. J., & Ginger, J. D. (2011). Response of Pierced Fixed Corrugated Steel Roofing Systems Subjected to Wind Loads. *Engineering Structures, 33*, 3290–3298. https://doi.org/10.1016/j.engstruct.2011.08.020

Ho, T. C. E., Davenport, A. G., & Surry, D. (1995). Characteristic pressure distribution shapes and load repetitions for the wind loading of low building roof panels. *Journal of Wind Engineering and Industrial Aerodynamics, 57*, 261–279. https://doi.org/10.1016/0167-6105(94)00106-N

Ho, T. C. E., Surry, D., Morrish, D., & Kopp, G. A. (2005). The UWO Contribution to the NIST Aerodynamic Database for Wind Loads on Low Buildings: Part 1. Archiving Format and Basic Aerodynamic Data. *Journal of Wind Engineering and Industrial Aerodynamics*, *93*, 1–30. https://doi.org/10.1016/j.jweia.2004.07.006

Holmes, J. D. (1988). Distribution of Peak Wind Loads on a Low-Rise Building. *Journal of Wind Engineering and Industrial Aerodynamics*, *29*, 59–67. https://doi.org/10.1016/0167-6105(88)90145-6

Holmes, J. D., & Best, R. J. (1981). An Approach to the Determination of Wind Load Effects on Low-Rise Buildings. *Journal of Wind Engineering and Industrial Aerodynamics*, *7*, 273–287. https://doi.org/10.1016/0167-6105(81)90054-4

Holmes, J. D. (2015). *Wind Loading of Structures, Third Edition*. CRC Press.

Kopp, G. A., Doddipatla, L. S., & Wu, C.-H. 14th Americas Conference on Wind Engineering. In: In *Wind Loads on a 50m High, Low-Rise Shaped Building with a Flat Roof*. 2022.

Kopp, G. A., & Morrison, M. J. (2018). Component and Cladding Wind Loads for Low-Slope Roofs on Low-Rise Buildings. *Journal of Structural Engineering*, *144*, 1–11. https://doi.org/10.1061/(ASCE)ST.1943-541X.0001989.

Kopp, G. A., Morrison, M. J., Gavanski, E., Henderson, D. J., & Hong, H. P. (2010). "Three Little Pigs" Project: Hurricane Risk Mitigation by Integrated Wind Tunnel and Full-Scale Laboratory Tests. *Natural Hazards Review*, *11*, 151–161. https://doi.org/10.1061/(ASCE)NH.1527-6996.0000019

Kopp, G. A., Morrison, M. J., & Henderson, D. J. (2012). Full-Scale Testing of Low-Rise, Residential Buildings with Realistic Wind Loads. *Journal of Wind Engineering and*

Industrial Aerodynamic, *104-106*, 25–39. https://doi.org/10.1016/j.jweia.2012.01.
004

Kopp, G. A., Surry, D., & Mans, C. (2005). Wind Effects of Parapets on Low Buildings:
Part 1. Basic Aerodynamics and Local Loads. *Journal of Wind Engineering and
Industrial Aerodynamics*, *93*, 817–841. https://doi.org/10.1016/j.jweia.2005.08.006

Kwan, K. (2020). *Effects of Corner Radii on Wind Tunnel Testing of Low-Rise Buildings*
(Master of Engineering Science in Civil and Environmental Engineering). University of Western Ontario.

Levitan, M. L., & Mehta, K. C. (1992a). Texas Tech Field Experiments for Wind Loads
Part 1: Building and Pressure Measuring System. *Journal of Wind Engineering and
Industrial Aerodynamics*, *41*, 1565–1576. https://doi.org/10.1016/0167-6105(92)
90372-H

Levitan, M. L., & Mehta, K. C. (1992b). Texas Tech Field Experiments for Wind Loads
Part II: Meteorological Instrumentation and Terrain Parameters. *Journal of Wind
Engineering and Industrial Aerodynamics*, *41*, 1577–1588. https://doi.org/10.1016/
0167-6105(92)90373-I

Lieblein, J. (1974). *Efficient Methods of Extreme-Value Methodology: Nsbir 74-602* (Standard). Institute for Applied Technology. Washington, DC, United States.

Lin, J. X., & Surry, D. (1998). The Variation of Peak Loads with Tributary Area Near
Corners on Flat Low Building Roofs. *Journal of Wind Engineering*, *77&78*, 185–
196. https://doi.org/10.1016/S0167-6105(98)00142-1

Liu, Y., Kopp, G. A., & Chen, S.-f. (2021). An Examination of the Gust Effect Factor for
Rigid High-Rise Buildings. *Frontiers in Built Environment*, *6*, 1–14. https://doi.org/
10.3389/fbuil.2020.620071

Morrison, M. J., & Kopp, G. A. (2010). Analysis of Wind-Induced Clip Loads on Standing Seam Metal Roofs. *Journal of Structural Engineering*, *136*, 334–337. https://doi.org/10.1061/(ASCE)ST.1943-541X.118

Morrison, M. J., & Kopp, G. A. (2018). Effects of Turbulence Intensity and Scale on Surface Pressure Fluctuations on the Roof of a Low-Rise Building in the Atmospheric Boundary Layer. *Journal of Wind Engineering and Industrial Aerodynamics*, *183*, 140–151. https://doi.org/10.1016/j.jweia.2018.10.017

Morrison, M. J., & Reinhold, T. A. 14th International Conference on Wind Engineering. In: In *Performance of Metal Roofing to Realistic Wind Loads and Evaluation of Current Test Standards*. 2015.

Nasiri, M. (2019). *Full-Scale Measurements to Evaluate Single-Ply Metal Roof Performance Under Extreme Wind Loads* (Doctor of Philosophy in Civil and Environmental Engineering). University of Western Ontario.

Prevatt, D. O., & Schiff, S. D. (1996). *Uplift Testing on Standing Seam Metal Roof Systems*. Clemson University.

Prevatt, D. O., Schiff, S. D., & Sparks, P. R. In Proceedings of the 11th Conference of Roofing Technology. In: In *A Technique to Assess Wind Uplift Performance of Standing Seam Metal Roofs*. 1995.

Saathoff, P. J., & Melbourne, W. H. (1989). The Generation of Peak Pressures in Separated/Reattaching Flows. *Journal of Wind Engineering and Industrial Aerodynamics*, *32*, 121–134.

Schroter, R. C. From the Proceedings of the 1985 International Symposium on Roofing Technology. In: In *Air Pressure Testing of Sheet Metal Roofing*. 1985.

Sinno, R. R. 19th International Specialty Conference on Cold-Formed Steel Structures. In: In *Response of Metal Roofs to Uniform Static and True Hurricane Wind Loads*. 2008.

Smith, T. L. (1995). Insights on Metal Roof Performance in High-Wind Regions. *Professional Roofing*, 1–5.

Song, X., Zhang, Y., & Zhang, Q. (2017). Failure Modes and Loading Bearing Capacity of Corrugated Steel Roofs Connected by Standing Seam Clips. *Steel Structures*, *17*, 1341–1352. https://doi.org/10.1007/s13296-017-1206-9

St. Pierre, L. (2002). *Evaluation of Wind Load Provisions for Low Buildings* (Master of Engineering Science in Civil and Environmental Engineering). University of Western Ontario.

St.Pierre, L. M., Kopp, G. A., Surry, D., & Ho, T. C. E. (2005). The UWO Contribution to the NIST Aerodynamic Database for Wind Loads on Low Buildings: Part 2. Comparison of Data with Wind Load Provisions. *Journal of Wind Engineering and Industrial Aerodynamics*, *93*, 31–59. https://doi.org/10.1016/j.jweia.2004.07.007

Surry, D., Sinno, R. R., Nail, B., Ho, T. C. E., Farquhar, S., & Kopp, G. A. (2007). Structurally Effective Static Wind Loads for Roof Panels. *Journal of Structural Engineering*, *133*, 871–885. https://doi.org/10.1061/(ASCE)0733-9445(2007)133:6(871)

Vickery, B. J. (1965). *On the Flow Behind a Coarse Grid and Its Use As a Model of Atmospheric Turbulence in Studies Related to Wind Loads on Buildings* (NPL Aero Report 1143).

Wang, J., & Kopp, G. A. (2021b). Comparisons of Aerodynamic Data with the Main Wind Force–Resisting System Provisions of ASCE 7-16. I: Low-Rise Buildings. *Journal*

of Structural Engineering, 147, 1–20. https://doi.org/10.1061/(ASCE)ST.1943-541X.0002925

Wang, J., & Kopp, G. A. (2021a). Gust Effect Factors for Windward Walls of Rigid Buildings with Various Aspect Ratios. *Journal of Wind Engineering and Industrial Aerodynamics, 212,* 1–21. https://doi.org/10.1016/j.jweia.2021.104603

Western University. (1980). *Boundary Layer Wind Tunnel Laboratory (BLWTL).* Retrieved October 19, 2022, from https://www.uwo.ca/projects/heritage/heritage4/

Wu, C. H., Akon, A. F., & Kopp, G. A. (2017). Effects of Turbulence on the Mean Pressure Field in the Separated-Reattaching Flow Above a Low-Rise Building. *Journal of Wind Engineering and Industrial Aerodynamics, 171,* 79–92. https://doi.org/10.1016/j.jweia.2017.09.013

Xia, Y. (2022). *Analysis of Standing Seam Metal Roofs Subjected to Extreme Wind Loads* (Doctor of Philosophy in Civil and Environmental Engineering). University of Western Ontario.

Appendix

A Supplementary Figures

A.1 Comparative Study of Clip Loads based on Clip Type

The following results are for the B1-H2 model. The results for B1-H1, as well as the roof
layout for B1, are shown in Chapter 5.

(a)   (b)
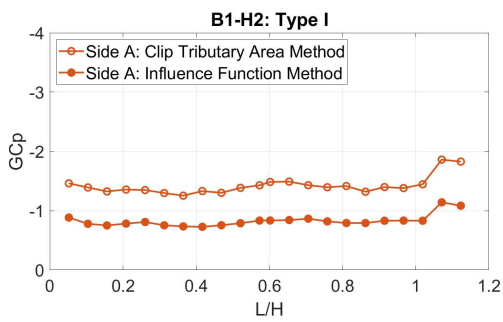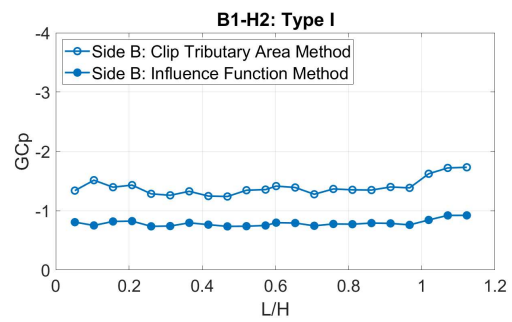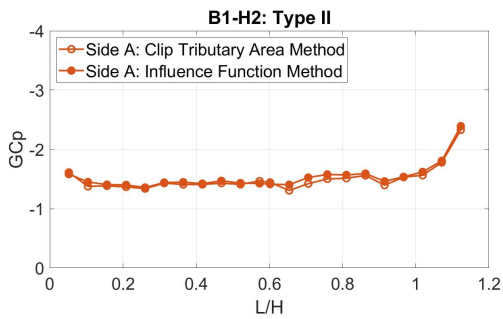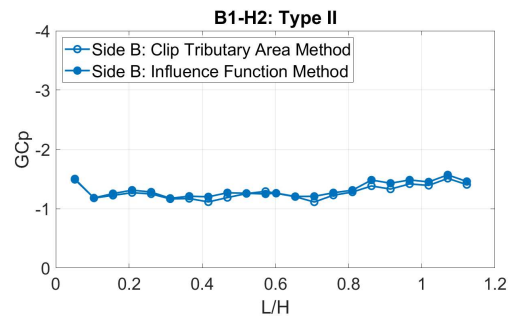
(c)   (d)
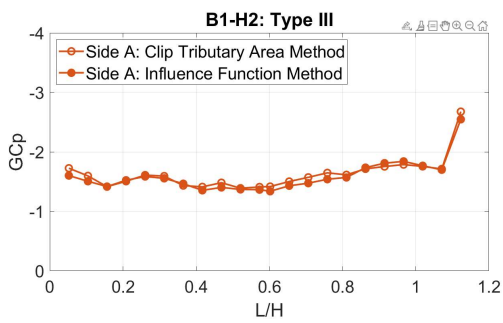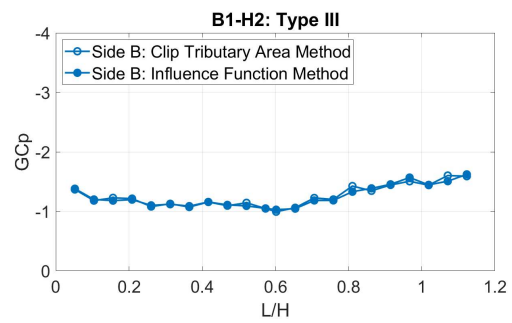
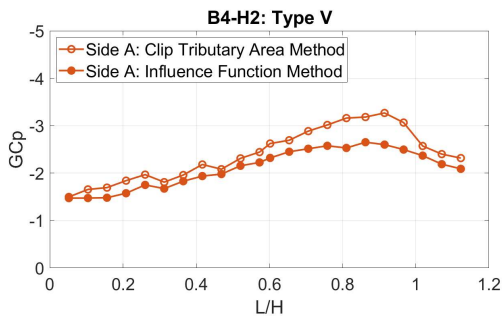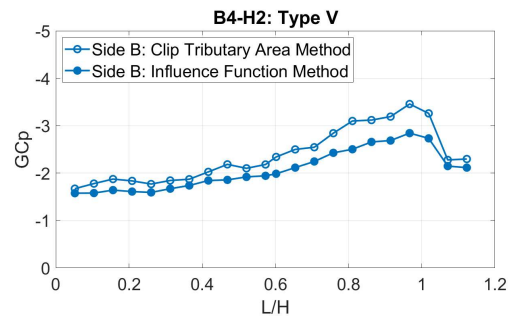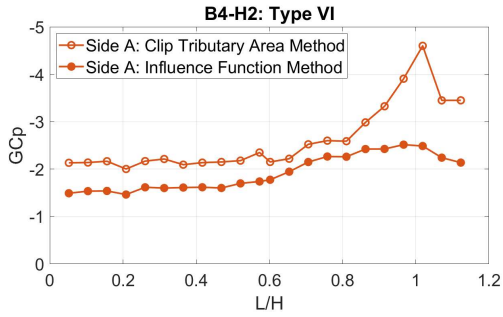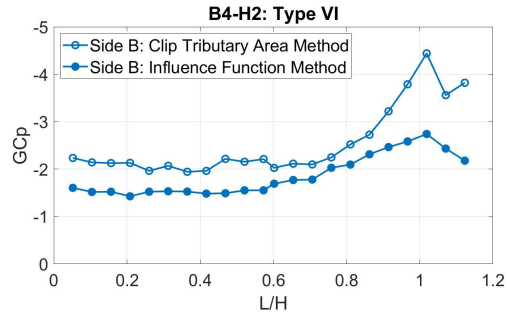(e)   (f)
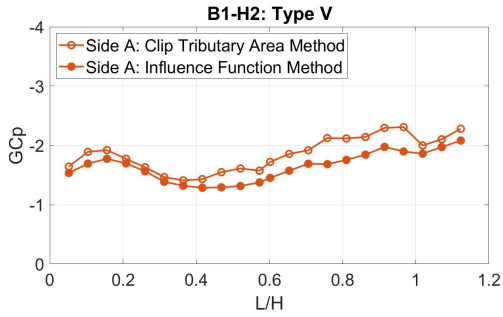
(g)
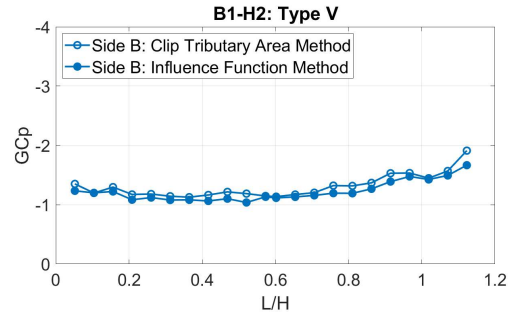
(h)
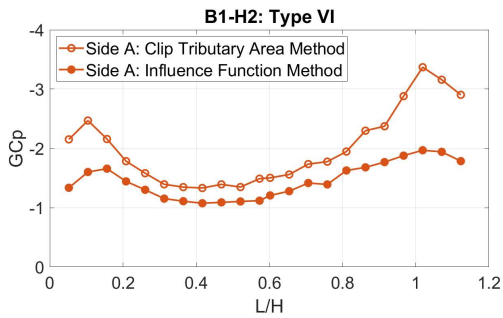
(i)
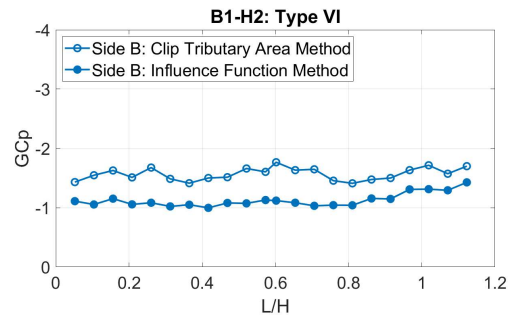
(j)

Figure 66: Comparison of GCp values between the Clip Tributary Area Method and the Influence Function Method for B1-H2. Graphs in (a), (c), (e), (g), and (i) display results for clip types I, II, III, V, VI, respectively, for Side A of the building model. Their Side B counterparts are shown in (b), (d), (f), (h), and (j).

The following results are for the B4 models, this includes B4-H1 and B4-H2.
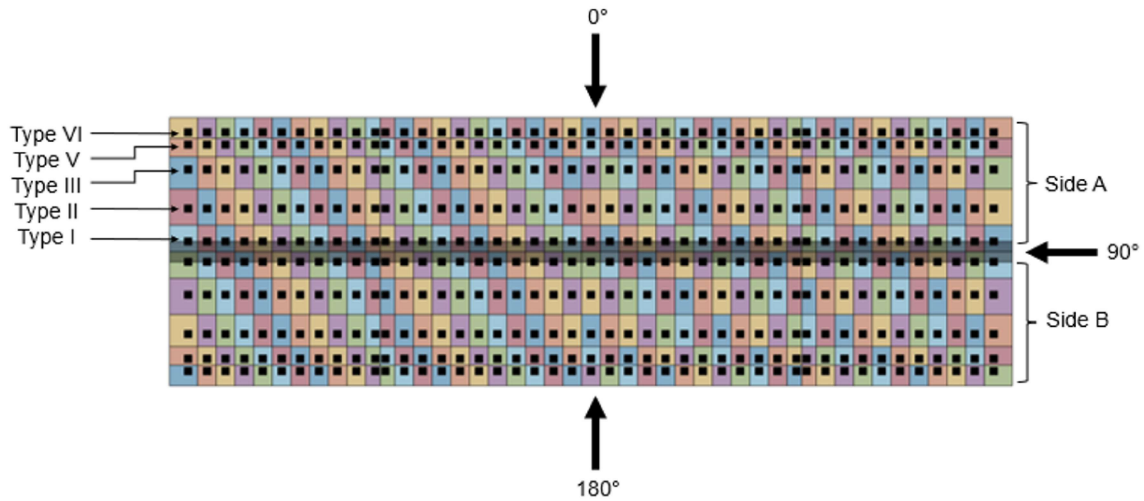
Figure 67: Roof layout of B4-H1 and B4-H2, including wind directions and clip types. The shaded boxes correspond to the clip geometric tributary areas.

(a)

(b)
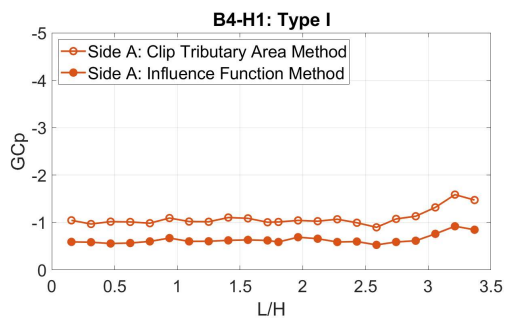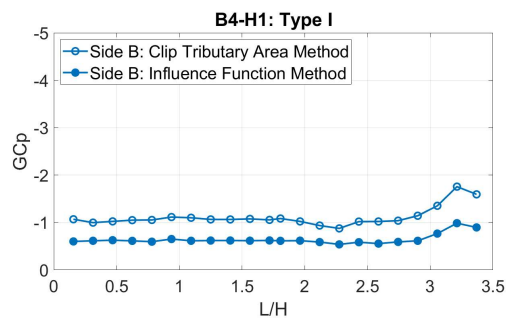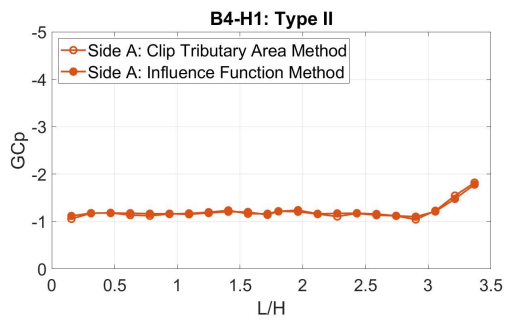
(c)
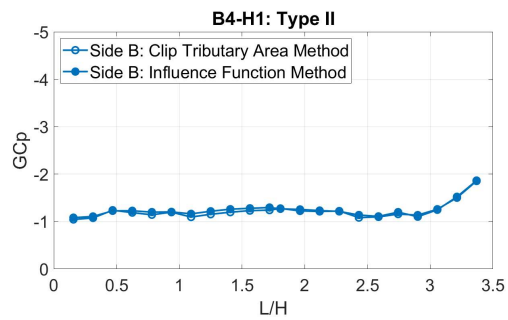
(d)
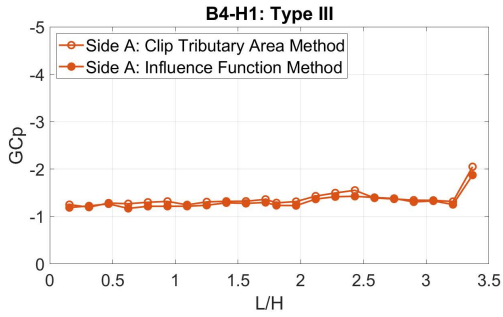
(e)
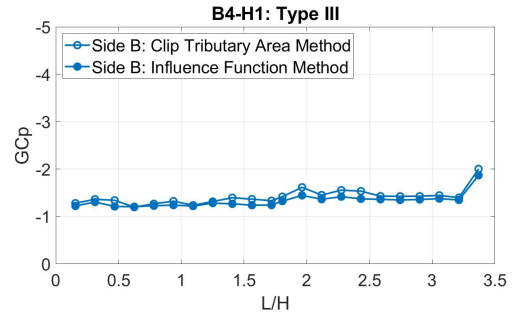
(f)
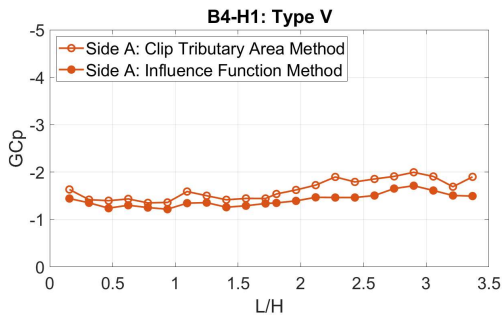
(g)
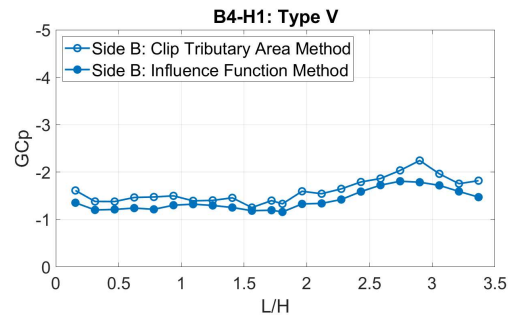
(h)
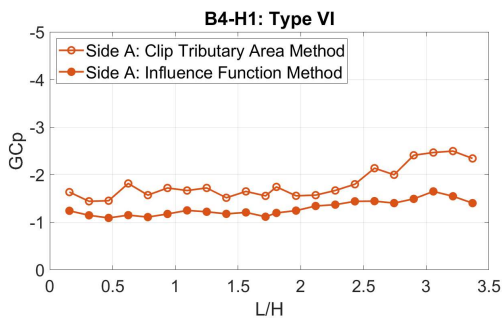
(i)
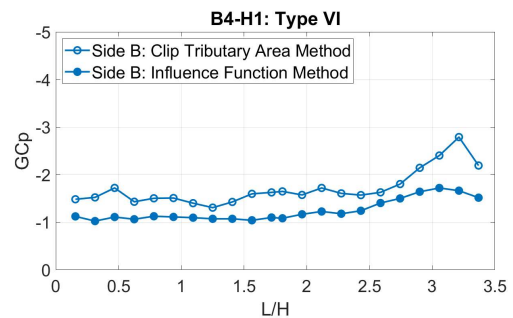
(j)

Figure 68: Comparison of GCp values between the Clip Tributary Area Method and the Influence Function Method for B4-H1. Graphs in (a), (c), (e), (g), and (i) display results for clip types I, II, III, V, VI, respectively, for Side A of the building model. Their Side B counterparts are shown in (b), (d), (f), (h), and (j).

The clip pressure coefficients are shown for B4-H2 in Figure 69 for each clip type.

119

(a)   **(b)**
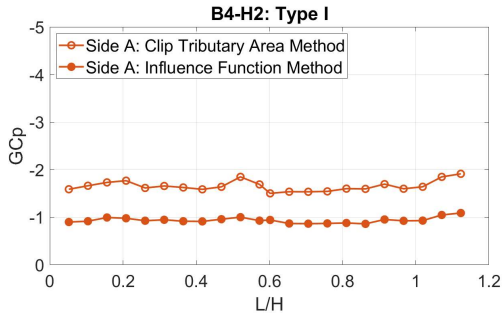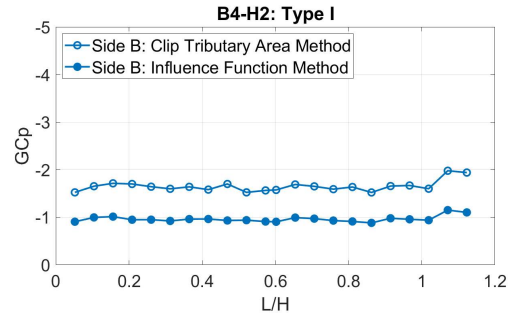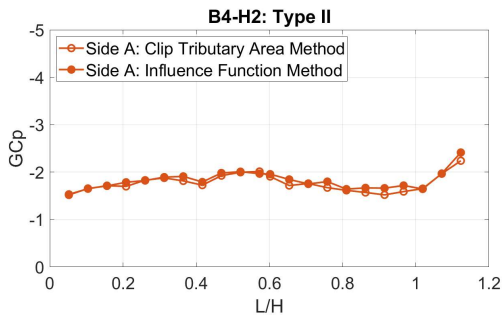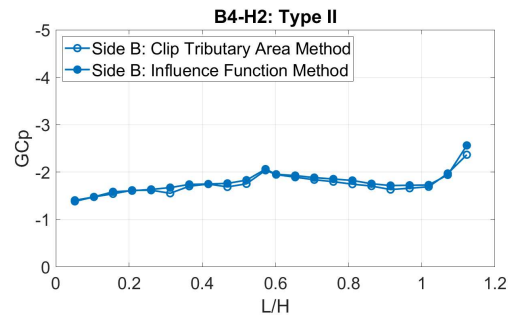
(c)   **(d)**
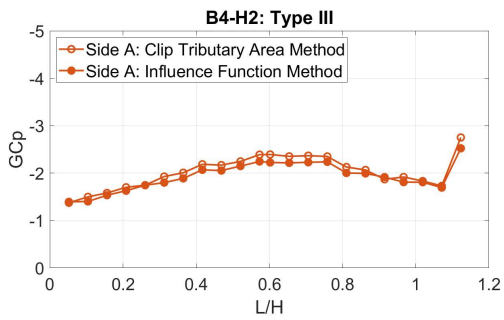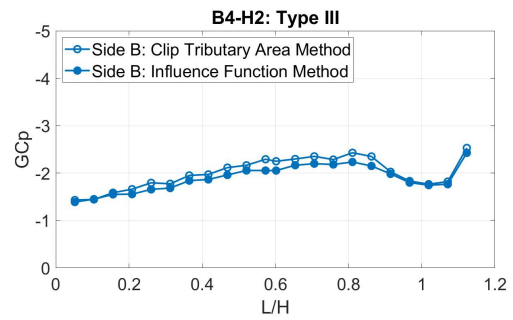
(e)   **(f)**

(g)   **(h)**

(i)   (j)

Figure 69: Comparison of GCp values between the Clip Tributary Area Method and the Influence Function Method for B4-H2. Graphs in (a), (c), (e), (g), and (i) display results for clip types I, II, III, V, VI, respectively, for Side A of the building model. Their Side B counterparts are shown in (b), (d), (f), (h), and (j).

A.2   Load Adjustment Factor
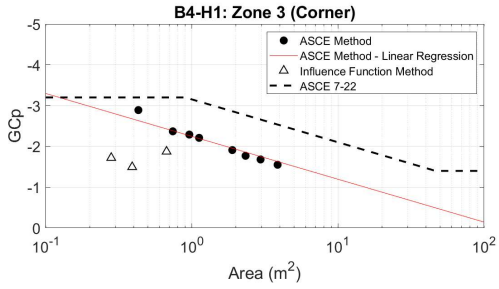
The linear regression results for B1-H1 are included in Chapter 5.
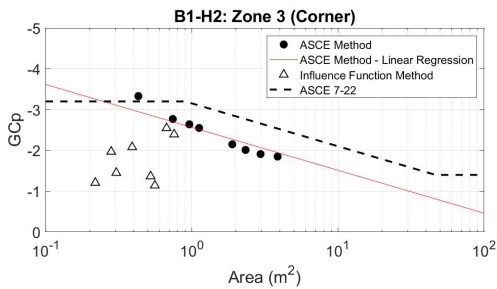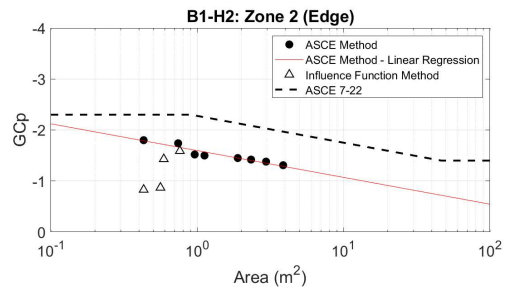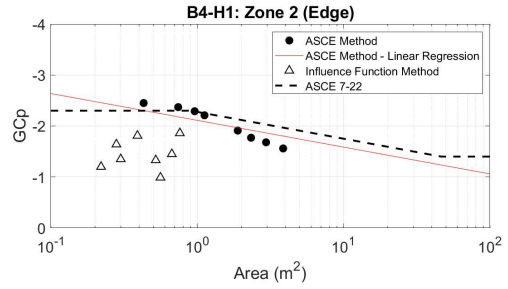

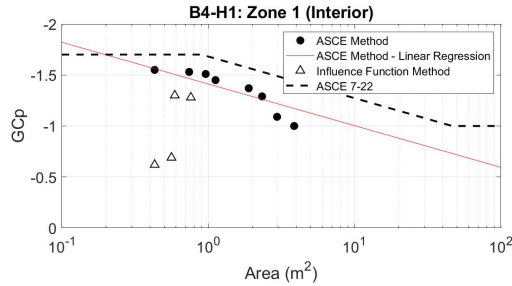(a)   (b)

Figure 70: Linear regression of the ASCE Method of B1-H2 for (a) zone 3 and (b) zone 2.
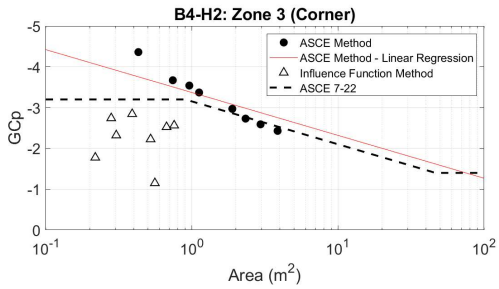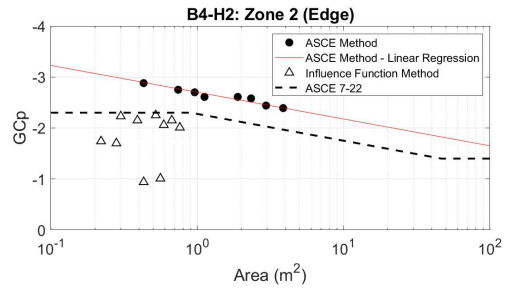
(a)

(b)

(c)

Figure 71: Linear regression of the ASCE Method of B4-H1 for (a) zone 3 (b) zone 2, and (c) zone 1.

(a)

(b)

Figure 72: Linear regression of the ASCE Method of B4-H2 for (a) zone 3 and (b) zone 2.